Dmitry N. Chigrin

# Electromagnetic waves propagation in photonic crystals with incomplete photonic bandgap

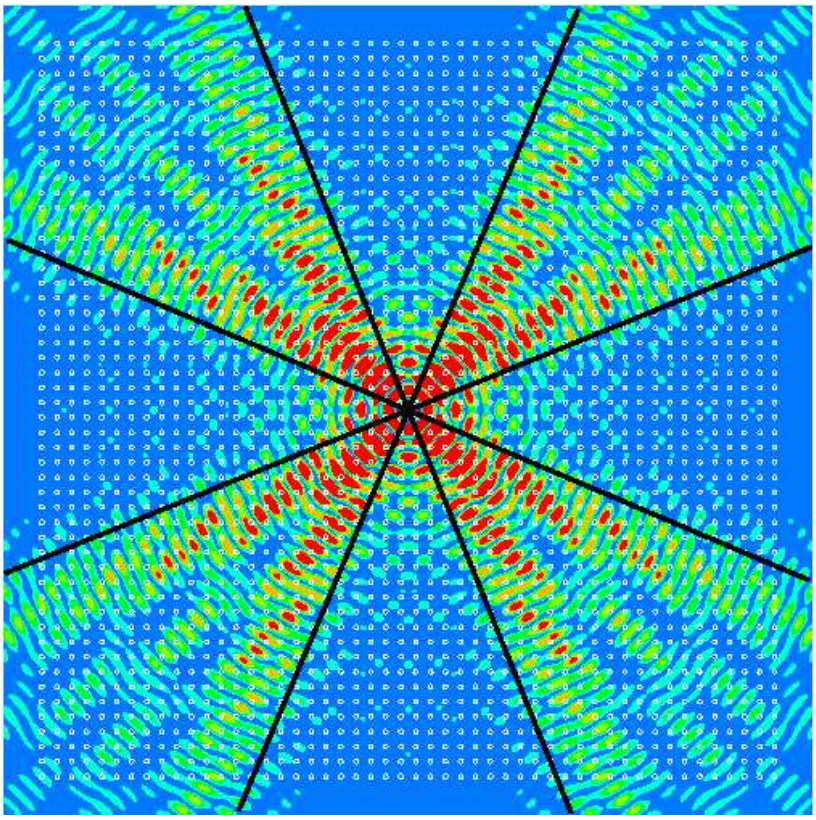

# Electromagnetic waves propagation in photonic crystals with incomplete photonic bandgap

Vom Fachbereich Elektrotechnik und Informationstechnik
der Bergischen Universität Wuppertal genehmigte Dissertation
zur Erlangung des Grades eines Doktors der Ingenieurwissenschaften
(Dr.-Ing.)

vorgelegt von
Diplom-Physiker
**Dmitry N. Chigrin**
aus Minsk, Weißrussland

Wuppertal 2003

| | |
|---|---|
| Referent: | Prof. Dr. rer. nat. C. M. Sotomayor Torres |
| Korreferent: | Prof. Dr.-Ing. V. Hansen |

Tag der mündlichen Prüfung: 23.01.2004

# Abstract

In this thesis, electromagnetic wave propagation in a dielectric periodic medium, photonic crystal, described by an incomplete photonic bandgap are studied.

A total omnidirectional reflection from a one-dimensional periodic dielectric medium is predicted. The origins of the omnidirectional reflection are discussed and optimum parameters of an omnidirectional mirror are presented. Theoretical predictions are compared with experimental realization of the mirror at optical frequencies.

The influence of a strong anisotropy of a three-dimensional periodic dielectric medium on emission properties of the classical dipole is studied. It is shown that the anisotropy of a photonic crystal leads to modifications of both the far-field radiation pattern and the radiated power of a dipole. If the dipole frequency is within a partial bandgap, the radiated power is suppressed in the direction of a stopband and enhanced in the direction of the group velocity, which is stationary with respect to a small variation of the wave vector. Such an enhancement is explained in terms of photon focusing phenomenon.

Several numerical examples illustrating modification of radiation pattern are given. Theoretical predictions of radiation pattern are compared with experimental photoluminescence of laser dye molecules embedded in an inverted opaline photonic crystal.

It is shown that far-field radiation pattern of the classical dipole can be also modified due to interference of photonic crystal eigenmodes at the detector plane. The physical reasons for the interference and the possibilities of its experimental observation are discussed.

A two-dimensional photonic crystal is proposed, which cancels out a natural diffraction of the laser beam for a wide range of beam widths and beam orientations with respect to the crystal lattice. The spreading of the beam is counteracted by the crystal anisotropy, like in the case of spatial solitons the nonlinearity of the medium counteracts the natural spreading of the beam due to diffraction.

# Zusammenfassung

In dieser Arbeit wird die Ausbreitung elektromagnetischer Wellen in einem dielektrischen periodischen Medium mit einer unvollständigen photonischen Bandlücke untershucht.

Die vollständige omnidiretkionale Reflektion eines eindimensionalen periodischen dielektrischen Mediums wird vorhergesagt. Die Herkunft der omnidiretkionalen Reflektion wird diskutiert und optimale Parameter für die Geometrie und das Material eines solchem Reflektors berechnet. Die theoretischen Vorhersagen werden mit experimentellen Ergebnisen bei optischen Frequenzen verglichen.

Untersucht wurde desweiteren der Einfluß einer starken Anisotropie eines dreidimensionalen periodischen Dielektrikas auf Emissionseigenschaften des klassischen Dipols. Es zeigt sich, daß Anisotropien zu einer Modifizierung des Fernfeld-Strahlungs-Diagramms und der Emissionsintensität eines Dipols führt. Falls sich eine Dipolfrequenz innerhalb des partiellen Bandgaps befindet, so erzeugt eine Fernfeld-Emissionsintensität eine Unterdrückung in der Richtung des Stopbandes und eine Verstärkung in der Richtung der Gruppengeschwindigkeit, welche für eine kleine Variation des Wellenvektors mathematisch stationär ist. Solch eine Verstärkung wird bezüglich des Photonfokussierungs-Phänomens erklärt.

Es wird eine Anzahl von numerischen Beispielen der Strahlungsdiagramm-Modifikation gegeben und die theoretischen Vorhersagen der Emissionsmodifikation werden mit Photolumineszensexperimenten in einem dreidimensionalen photonischen Kristall verglichen.

Weiterhin wird gezeigt, daß aufgrund der Interferenzen der photonischen Kristalleigenwerte an der Detektorebene das Fernfeld-Strahlungsdiagramm des klassischen Dipols geändert werden kann. Dabei werden die physikalischen Ursachen der Interferenzen und die Möglichkeiten ihrer experimentellen Beobachtung diskutiert.

Ein zweidimensionaler photonischer Kristall, der die natürliche Diffraktion eines Laserstrahls über einen weiten Bereich der Stahlbreite und Strahlorientierung bezüglich des Kristallgitters aufhebt, wird vorgeschlagen. Der Verbreiterung des Strahles wirkt

die Kristallanisotropie entgegen, wie dies in nichtlinearen Medien für räumliche Solitonen der Fall ist.

# Contents

# Chapter 1

# Introduction

## 1.1 Photonic crystals

Periodic media are well acknowledged for their capability to control the propagation and emission of electromagnetic waves and have gained a substantial attention as *photonic crystals* or *photonic bandgap structures.*

Photonic crystals are characterized by three parameters: the lattice topology, the spatial period and the dielectric constants of the constituent materials. By suitable selection of these parameters, a gap in the electromagnetic dispersion relation can be created, within which the linear propagation of electromagnetic waves is forbidden. This forbidden frequency range is called the *photonic bandgap.* It is said that a photonic bandgap is *complete*, if a forbidden gap exists for all polarizations and all propagation direction. It is common to distinguish one-, two- and three-dimensional photonic crystals by the number of dimensions within which the periodicity has been introduced into the structure. Examples of one-, two- and three-dimensional photonic crystals are given in figure 1.1. Necessary but not sufficient conditions to obtain a *complete photonic bandgap* are a periodicity in three spatial directions and a large difference in the dielectric constants of the constituent materials.

The first self-consistent treatment of light emission in a periodic medium with a strong modulation of the dielectric function was made by Bykov in 1972 [4]. Bykov pointed out the possibilities to realize a complete photonic bandgap and the inhibition of the spontaneous emission of atoms embedded in a periodic medium. The first self-consistent treatment of electromagnetic eigenmodes and photonic band structure in a three-dimensional periodic medium with a large dielectric function modulation was given by Ohtaka in 1979 [5]. These two pioneering works did not gain the attention they deserved at the time. It was only after the appearance of the papers

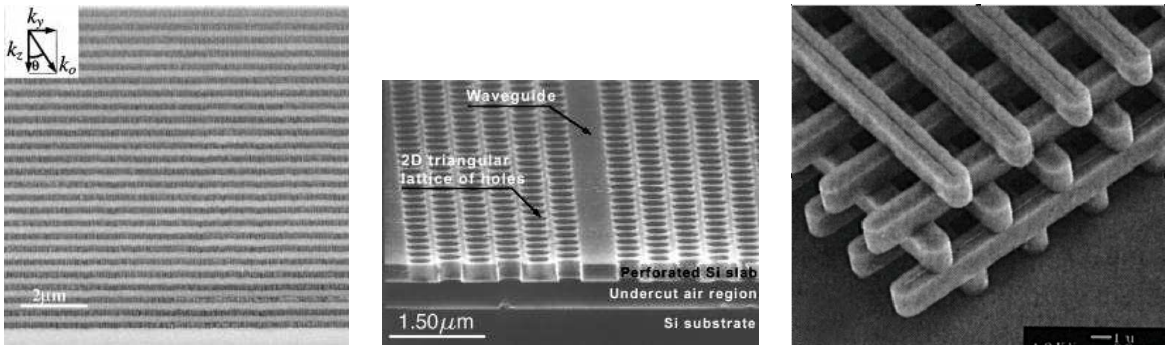


Figure 1.1: Examples of one-, two- and three-dimensional photonic crystals. Left: SEM image of the cross section of a 1D all-silicon photonic crystal (after Bruyant et. al. [1]). Center: SEM image of a 2D silicon photonic crystal with a straight waveguide (after Loncar et. al. [2]). Right: SEM image of a 3D silicon photonic crystal, woodpile structure (.after Lin et. al. [3]).

of Yablonovitch [6] and John [7] in 1987, than the idea to control the flow of light by means of a periodic medium become popular. Yablonovitch [6] proposed to use a three-dimensional periodic medium, which he called a *photonic crystal*, to inhibit the spontaneous emission of atoms and to realize localized defect modes and consequently to enhance the spontaneous emission. In the same year, John [7] proposed the use of a disordered three-dimensional periodic medium to localize electromagnetic waves. Many interesting quantum optical phenomena such as the bound state of photons [4, 8] and non-exponential decay of the spontaneous emission [4, 8] were predicted. These ideas actively stimulated research area, which leads both to various unexpected results in the fundamental understanding of light–matter interaction and to various new optoelectronics and photonics applications. Summaries of early studies can be found in [9, 10] and more recent results can be found in [11, 12].

Opportunities to control light emission and extraction using photonic crystals offer vast potential in improving existing light sources. For example, the external efficiency of light-emitting diodes typically does not exceed 2-5%, while the internal quantum efficiency of their active material can be as high as 99%. The introduction of a two-dimensional photonic crystal into the light-emitting diode design can significantly improve its external quantum efficiency [13, 14]. Another example of improved light source properties is a highly directional light source employing a three-dimensional photonic crystal [15, 16]. An inhibited spontaneous emission should result in substantially reduced threshold of semiconductor lasers, which solves the problem with removal of excess heat generated by the finite laser threshold.

Even a passive integrated optical circuit incorporating waveguides, bends, junctions and couplers typically extends over several centimeters rather than micrometers in size.

Wave guided light does not readily negotiate sharp bends, so transitions need to be gradual. Couplers typically have long interaction lengths with respect to the wavelength of light. Photonic crystals possessing a complete photonic bandgap offer one of the possible solutions to miniaturization of integrated optics. Optical waveguides, sharp bends and large-angle Y-junctions with virtually no excess loss have been designed in the micrometer and sub-micrometer length scale using photonic crystals [17]. Another important issue for integrated optics is filtering. Photonic crystals are proven to be good materials for realization of high quality resonators with very sharp filtering characteristics [17]. A compact photonic crystal based add/drop filters suitable for wavelength division multiplexing (WDM) applications have been proposed based on photonic crystal waveguides and resonators [18, 19].

In the microwave and millimeter wave domain, photonic crystals and photonic bandgap are usually called *electromagnetic crystals* and *electromagnetic bandgap*, respectively. Electromagnetic crystals are mainly used as antenna substrates [20, 21, 22, 23, 24, 25]. Conventional integrated circuit antennas on a semiconductor substrate of dielectric constant $\varepsilon$ have the drawback that the power radiated into the substrate is a factor $\varepsilon^{3/2}$ larger than the power radiated in free-space [20]. Thus, antennas on a typical semiconductor radiate only about 2% of their power in free-space. By fabricating the antenna on an electromagnetic crystal with a driving frequency within a complete electromagnetic bandgap, no power should be transmitted into the crystal if there are no evanescent surface modes. Several successful antenna designs with improved directionality and efficiency up to 70% have been reported [20, 21, 22]. To suppress surface modes of an antenna substrate a electromagnetic crystal can be used as a high-impedance surface [23, 24, 25]. Microwave and millimeter wave filters, couplers, resonators, reflectors and guiding structures can be also designed on the basis of electromagnetic crystals [26].

Although the main expectations associated with photonic crystals rely on the existence of a complete photonic bandgap, photonic crystals with an incomplete photonic bandgap can also influence dramatically the electromagnetic wave propagation. At photonic bands frequencies a photonic crystal displays strong dispersion and anisotropy. Anisotropy of photonic crystals known to be a reason for the number of anomalies in an electromagnetic beam propagation, which are usually referred to as *superprism* or *ultrarefractive* phenomena [27, 28, 29]. The first self-consistent theoretical and experimental study of ultrarefractive phenomena in a one-dimensional period medium was reported by Russell [27] and Zengerle [28] in 1986 and 1987, respectively. Ten years later, Kosaka et al. reported the experimental observation of the ultrarefraction in a three-dimensional photonic crystal [29]. Since that time an extraordinary large or negative beam bending [29], a beam self-collimation [30] and the photon focusing [31, 32]

were reported. More recently, a photonic crystal superprism was proposed for WDM applications [33].

## 1.2 Dissertation organization

The focus of the work presented in this thesis, was the theoretical study of the peculiarities of electromagnetic wave propagation in a dielectric periodic medium with an incomplete photonic bandgap. The main goal of this work was to show that a photonic crystal with an incomplete photonic bandgap can essentially influence both electromagnetic wave flow and light emission processes.

Dissertation is organized in four parts. The first part (chapters 2 and 3) provides an introduction to the basic theoretical concepts required for the material that follows. Parts two to four contain main results of the thesis. The influence of an incomplete photonic bandgap upon total reflection on, light emission in and light refraction by a photonic crystal is studied in part II (chapter 4), part III (chapters 5, 6 and 7) and part IV (chapter 8) respectively.

The general properties of the wave equation in periodic media are introduced and discussed in chapter 2. In chapter 3, total reflection on, anomalous refraction by and modified emission in a photonic crystal are explained using simple examples.

Chapter 4 reports on a remarkable property of a one-dimensional photonic crystal. A one-dimensional periodic medium can totally reflect electromagnetic waves of any polarization at all angles of incidence within a given frequency region. In this chapter, design criteria for and experimental demonstration of an omnidirectional mirror are presented.

Chapter 5 presents an asymptotic analysis of a radiation pattern of a classical dipole in a photonic crystal with an incomplete photonic bandgap. A far-field radiation pattern demonstrates a strong modification with respect to the dipole radiation pattern in vacuum. The radiated power is suppressed in the direction of the spatial stopband and is strongly enhanced in the direction of the group velocity, which is stationary with respect to a small variation of the wave vector. An effect of the radiated power enhancement is explained in terms of photon focusing. A numerical example is given for a square-lattice two-dimensional photonic crystal. Predictions of asymptotic analysis are substantiated with finite-difference time-domain calculations.

In chapter 6 it is reported that a far-field radiation pattern of the classical dipole can be additionally modified due to the interference of photonic crystal eigenmodes at the detector plane. In particular, a modulation of angle resolved emission spectra from a coherent light source will be the result of both emission rate modification and light interference at the detector position. In this chapter, a physical picture of interference

fringes formation in the far-field radiation pattern of the classical dipole is discussed in the framework of an asymptotic analysis of Maxwell's equations. A numerical example is given for a two-dimensional square lattice of air holes in polymer. The relevance of the results for experimental observation is discussed.

Chapter 7 describes the influence of an incomplete photonic bandgap upon the photoluminescence of a dye embedded in a three-dimensional opaline photonic crystal. A modification of emission directionality diagrams with respect to free space is reported. An enhancement and suppression of the emission intensity in some directions are interpreted as the spontaneous emission rate modification and explained in terms of photon focusing phenomenon. A theoretical model developed in chapter 5 reveals a reasonable agreement with experiment results.

In chapter 8 a two-dimensional photonic crystal is proposed, which cancels out a natural diffraction of the laser beam for a wide range of beam widths and beam orientations with respect to the crystal lattice. It is shown that for some frequencies the form of iso-frequency contours mimics the form of the first Brillouin zone of the crystal. A wide angular range of flat dispersion exists for such frequencies. The regions of iso-frequency contours with near zero curvature cancel out diffraction of the light beam, leading to a self-guided beam.

The overall conclusions and discussions of future research directions are given in chapter 9, which completes this thesis.

# Bibliography


[1] A. Bruyant, G. Lerondel, P. J. Reece, and M. Gal, "All-silicon omnidirectional mirrors based on one-dimensional photonic crystals," *Appl. Phys. Lett.* **82,** 3227–3229 (2003).

[2] M. Loncar, D. Nedeljkovic, T. Doll, J. Vuckovic, A. Scherer, and T. P. Pearsall, "Waveguiding in planar photonic crystals," *Appl. Phys. Lett.* **77,** 1937–1939 (2000).

[3] S. Y. Lin, J. G. Fleming, D. L. Hetherington, B. K. Smith, R. Biswas, K. M. Ho, M. M. Sigalas, W. Zubrzycki, S. R. Kurtz, and J. Bur, "A three-dimensional photonic crystal operating at infrared wavelengths," *Nature* **394,** 251–253 (1998).

[4] V. P. Bykov, "Spontaneous emission in a periodic structure," *Soviet Physics - JETP* **35,** 269–273 (1972).

[5] K. Ohtaka, "Energy band of photons and low-energy photon diffraction," *Phys. Rev. B* **19,** 5057–5067 (1979).

[6] E. Yablonovitch, "Inhibited spontaneous emission in solid-state physics and electronics," *Phys. Rev. Lett.* **58,** 2059–2062 (1987).

[7] S. John, "Strong localization of photons in certain disordered dielectric superlattices," *Phys. Rev. Lett.* **58,** 2486–2489 (1987).

[8] S. John and J. Wang, "Quantum electrodynamics near a photonic nand gap: photon bound state and dressed atoms," *Phys. Rev. Lett.* **64,** 2418–2421 (1990).

[9] *Confined Electrons and Photons: New Physics and Applications*, E. Burstein and C. Weisbuch, eds., (Plenum Press, New York, 1995).

[10] *Photonic Band Gap Materials*, C. Soukoulis, ed., (Kluwer Academic, Dordrecht, 1996).

[11] *Photonic Crystals and Light Localization in the 21st Century*, C. Soukoulis, ed., (Kluwer Academic, Dordrecht, 2001).

[12] K. Sakoda, *Optical Properties of Photonic Crystals* (Springer, Berlin, 2001).

[13] H. Hirayama, T. Hamano, and Y. Aoyagi, "Novel surface emitting laser diode using photonic band-gap crystal cavity," *Appl. Phys. Lett* **69,** 791–793 (1996).

[14] M. Boroditsky, R. Vrijen, T. F Krauss, R. Coccioli, R. Bhat, and E. Yablonovitch, "Spontaneous emission extraction and Purcell enhancement from thin-film 2-D photonic," *IEEE J. Lightwave Technol.* **17,** 2096–2112 (1999).

[15] B. Temelkuran, M. Bayindir, E. Ozbay, R. Biswas, M. M. Sigalas, G. Tuttle, and K. M. Ho, "Photonic crystal based resonant antenna with a very high directivity," *J. Appl. Phys* **87,** 603–605 (2002).

[16] S. Enoch, B. Gralak, and G. Tayeb, "Enhanced emission with angular confinement from photonic crystals," *Appl. Phys. Lett.* **81,** 1588–159 (2002).

[17] J. D. Joannopoulos, R. D. Meade, and J. N. Winn, *Photonic crystals: molding the flow of light* (Princeton University Press, Princeton NJ, 1995).

[18] S. Fan, P. R. Villeneuve, J. D. Joannopoulos, and H. A. Haus, "Channel Drop Tunneling through Localized States," *Phys. Rev. Lett.* **80,** 960–963 (1998).

[19] S. Noda, N. Yamamoto, M. Imrada, H. Kabayashi, and M. Okato, "Investigation of a channel-add/drop-filtering device using acceptor-type point defects in a two-dimensional photonic-crystal slab," *Appl. Phys. Lett.* **83,** 407–409 (2003).

[20] S. D. Cheng, R. Biswas, E. Ozbay, S. McCalmont, G. Tuttle, and K.-M. Ho, "Optimized dipole antennas on photonic band gap crystals," *Appl. Phys. Lett.* **67,** 3399–3401 (2003).

[21] E. R. Brown, C. D. Parker, and E. Yablonovitch, "Radiation properties of a planar antenna on a photonic-crystal substrate," *J. Opt. Soc. Am. B* **10,** 404–407 (1993).

[22] E. R. Brown, C. D. Parker, and O. B. McMahon, "Effect of surface composition on the radiation pattern from a photonic-crystal planar-dipole antenna," *Appl. Phys. Lett.* **64,** 3345–3347 (1994).

[23] Y.-J. Park, A. Herschlein, and W. Wiesbeck, "A photonic bandgap structure for guiding and suppresing surface waves in millimeter-wave antennas," *IEEE Trans. MTT* **49,** 1854–1859 (2001).

[24] R. F. J. Broas, D. F. Sievenpiper, and E. Yablonovitch, "A high-impedance ground plane applied to a cellphone handset geometry," *IEEE Trans. MTT* **49,** 1262–1265 (2001).

[25] S. G. Mao and M. Y. Chen, "Propagation characteristics of finite-width conductor-backed coplanar waveguides with periodic electromagnetic bandgap cells," *IEEE Trans. MTT* **50,** 2624–2628 (2002).

[26] M. Sarnowski, V. Hansen, T. Vaupel, E. Kreysa, and H. P. Gemund, "Characterization of diffraction anomalies in 2-D photonic bandgap structures," *IEEE Trans. MTT* **49,** 1868–1872 (2001).

[27] P. St. J. Russell, "Optics of Floquet-Block waves in dielectric gratings," *Appl. Phys. B: Photophysics & Laser Chemistry* **B39,** 231–246 (1986).

[28] R. Zengerle, "Light propagation in singly and doubly periodic planar waveguides," *J. Mod. Optics* **34,** 1589–1617 (1987).

[29] H. Kosaka, T. Kawashima, A. Tomita, M. Notomi, T. Tamamura, T. Sato, and S. Kawakami, "Superprism phenomena in photonic crystals," *Phys. Rev. B* **58,** R10096–R10099 (1998).

[30] H. Kosaka, T. Kawashima, A. Tomita, M. Notomi, T. Tamamura, T. Sato, and S. Kawakami, "Self-collimating phenomena in photonic crystals," *Applied Physics Letters* **74,** 1212–1214 (1999).

[31] P. Etchegoin and R. T. Phillips, "Photon focusing, internal diffraction, and surface states in periodic dielectric structures," *Phys. Rev. B* **53,** 12674–12683 (1996).

[32] D. N. Chigrin and C. M. Sotomayor Torres, "Periodic thin-film interference filters as one-dimensional photonic crystals," *Opt. Spectrosc.* **91,** 484–489 (2001).

[33] H. Kosaka, T. Kawashima, A. Tomita, M. Notomi, T. Tamamura, T. Sato, and S. Kawakami, "Superprism phenomena in photonic crystals: toward microscale lightwave circuits," *J. Lightwave Technol.* **17,** 2032–2038 (1999).

# Part I

# Principles of photonic crystals

# Chapter 2

# Eigenmodes of inhomogeneous dielectric media

The goal of this chapter is to introduce the reader to the main mathematical tools and underlying physical ideas, which are behind the theory of the electromagnetic waves propagation in periodic dielectric media, *photonic crystals*. The chapter consists on two sections. In section 2.1 the general properties of the wave equation in inhomogeneous media are introduced and discussed. Solutions of homogeneous and inhomogeneous wave equations are given in terms of normal modes expansion. In section 2.2 the influence of the periodicity on the properties of eigenwaves of an inhomogeneous dielectric medium is presented. Specifically, the *Bloch theorem* and the concept of *Bloch waves* are introduced. It is important to note, that this chapter should be regarded as a minimum introduction, sufficient for the appreciation of the results presented in this thesis. The chapter should not be considered as a complete and comprehensive introduction to the topic of electromagnetic waves propagation in photonic crystals. For more details, the reader is referred to existing textbooks covering the topic of electromagnetic wave propagation in periodic media [1, 2, 3] or the first few chapters of a solid-state physics textbooks [4, 5, 6].

## 2.1 Inhomogeneous dielectric media

### 2.1.1 Wave equations

All macroscopic electromagnetic theory, including light propagation and emission in inhomogeneous media, is governed by the macroscopic Maxwell's equations. In Gaussian

units (cgs units), the source-free Maxwell's equations take the form [7]

$$\nabla \times \mathbf{E}(\mathbf{r},t) = -\frac{1}{c}\frac{\partial \mathbf{B}(\mathbf{r},t)}{\partial t}, \tag{2.1}$$

$$\nabla \times \mathbf{B}(\mathbf{r},t) = \frac{1}{c}\frac{\partial \mathbf{D}(\mathbf{r},t)}{\partial t}, \tag{2.2}$$

$$\nabla \cdot \mathbf{D}(\mathbf{r},t) = 0, \tag{2.3}$$

$$\nabla \cdot \mathbf{H}(\mathbf{r},t) = 0. \tag{2.4}$$

Here, the standard notations for the electric field, $\mathbf{E}$, the magnetic field, $\mathbf{H}$, the electric displacement, $\mathbf{D}$, and the magnetic induction, $\mathbf{B}$, are used. $c$ is the speed of light in vacuum. To solve Maxwell's equations (2.1-2.4), one should complete them with the constitutive equations, which relate the electric displacement, $\mathbf{D}$, to the electric field, $\mathbf{E}$, and the magnetic induction, $\mathbf{B}$, to the magnetic field, $\mathbf{H}$. In the following, a general linear, non-magnetic, dielectric medium is studied. Then, the constitutive equations read

$$\mathbf{D}(\mathbf{r},t) = \varepsilon(\mathbf{r})\mathbf{E}(\mathbf{r},t), \tag{2.5}$$

$$\mathbf{B}(\mathbf{r},t) = \mathbf{H}(\mathbf{r},t), \tag{2.6}$$

where $\varepsilon(\mathbf{r})$ is a position-dependent dielectric permittivity.

Combining Maxwell's equations (2.1-2.4) with the constitutive equations (2.5-2.6) and eliminating the electric field $\mathbf{E}(\mathbf{r},t)$ or magnetic field $\mathbf{H}(\mathbf{r},t)$ in (2.1) and (2.2), one can obtain the following wave equations:

$$\nabla \times \nabla \times \mathbf{E}(\mathbf{r},t) + \frac{1}{c^2}\varepsilon(\mathbf{r})\frac{\partial^2 \mathbf{E}(\mathbf{r},t)}{\partial t^2} = 0, \tag{2.7}$$

$$\nabla \times \left\{ \frac{1}{\varepsilon(\mathbf{r})}\nabla \times \mathbf{H}(\mathbf{r},t) \right\} + \frac{1}{c^2}\frac{\partial^2 \mathbf{H}(\mathbf{r},t)}{\partial t^2} = 0. \tag{2.8}$$

Because the emission and the interaction between radiation and matter will be one of the main focus of this thesis, it is convenient to introduce the vector potential $\mathbf{A}(\mathbf{r},t)$ [7]. From Maxwell's equations (2.1-2.4) it is clear that the vector potential $\mathbf{A}(\mathbf{r},t)$ and the scalar potential $\varphi(\mathbf{r},t)$ can be introduced via the familiar relations [7]:

$$\mathbf{E}(\mathbf{r},t) = -\nabla\varphi - \frac{1}{c}\frac{\partial \mathbf{A}(\mathbf{r},t)}{\partial t}, \tag{2.9}$$

$$\mathbf{B}(\mathbf{r},t) = \nabla \times \mathbf{A}(\mathbf{r},t). \tag{2.10}$$

The gauge that is most commonly used in the radiation problems is the Coulomb or "radiation" gauge [7]. The absence of charge density implies that the scalar potential

$\varphi(\mathbf{r},t)$ is zero ($\varphi(\mathbf{r},t)=0$). With this choice, the transversality condition on $\mathbf{D}(\mathbf{r},t)$ (2.3) becomes [8]

$$\nabla\cdot[\varepsilon(\mathbf{r})\frac{\partial\mathbf{A}(\mathbf{r},t)}{\partial t}]=0. \tag{2.11}$$

One may now fix the gauge by imposing the requirement

$$\nabla\cdot[\varepsilon(\mathbf{r})\mathbf{A}(\mathbf{r},t)]=0, \tag{2.12}$$

which automatically fulfills condition (2.11). The gauge condition (2.12) is a generalization of the Coulomb gauge condition ($\nabla\cdot\mathbf{A}(\mathbf{r},t)=0$) appropriate to the presence of a dielectric [8].

Then, taking into account the constitutive equations (2.5-2.6), the electric and magnetic fields can be written in terms of the vector potential $\mathbf{A}(\mathbf{r},t)$ via:

$$\mathbf{E}(\mathbf{r},t)=-\frac{1}{c}\frac{\partial\mathbf{A}(\mathbf{r},t)}{\partial t}, \tag{2.13}$$

$$\mathbf{H}(\mathbf{r},t)=\nabla\times\mathbf{A}(\mathbf{r},t). \tag{2.14}$$

Combining equations (2.13-2.14) with Maxwell's equations (2.1-2.4) one obtains the homogeneous wave equation for the vector potential $\mathbf{A}(\mathbf{r},t)$:

$$\nabla\times\nabla\times\mathbf{A}(\mathbf{r},t)+\frac{1}{c^2}\varepsilon(\mathbf{r})\frac{\partial^2\mathbf{A}(\mathbf{r},t)}{\partial t^2}=0. \tag{2.15}$$

### 2.1.2 Eigenvalue problem

To find the solutions of wave equations (2.7-2.8) and (2.15) in the form of the time-harmonic function

$$\mathbf{F}(\mathbf{r},t)=\mathbf{F}_{\mathbf{k}}(\mathbf{r})\,e^{-i\omega_{\mathbf{k}}t}, \tag{2.16}$$

where the vector $\mathbf{F}$ is the electric field, $\mathbf{E}$, the magnetic field, $\mathbf{H}$, or the vector potential, $\mathbf{A}$, the vector function $\mathbf{F}_{\mathbf{k}}(\mathbf{r})$ should satisfy equations:

$$\mathcal{L}_E\mathbf{E}_{\mathbf{k}}(\mathbf{r})\equiv\frac{1}{\varepsilon(\mathbf{r})}\nabla\times\{\nabla\times\mathbf{E}_{\mathbf{k}}(\mathbf{r})\}=\frac{\omega_{\mathbf{k}}^2}{c^2}\mathbf{E}_{\mathbf{k}}(\mathbf{r}), \tag{2.17}$$

$$\mathcal{L}_H\mathbf{H}_{\mathbf{k}}(\mathbf{r})\equiv\nabla\times\left\{\frac{1}{\varepsilon(\mathbf{r})}\nabla\times\mathbf{H}_{\mathbf{k}}(\mathbf{r})\right\}=\frac{\omega_{\mathbf{k}}^2}{c^2}\mathbf{H}_{\mathbf{k}}(\mathbf{r}), \tag{2.18}$$

$$\mathcal{L}_A\mathbf{A}_{\mathbf{k}}(\mathbf{r})\equiv\frac{1}{\varepsilon(\mathbf{r})}\nabla\times\{\nabla\times\mathbf{A}_{\mathbf{k}}(\mathbf{r})\}=\frac{\omega_{\mathbf{k}}^2}{c^2}\mathbf{A}_{\mathbf{k}}(\mathbf{r}), \tag{2.19}$$

where three linear differential operators $\mathcal{L}_E$, $\mathcal{L}_H$ and $\mathcal{L}_A$ are defined by the first equality in each of the above equations.

Equations (2.17-2.19) represent the eigenvalue problems for differential operators ($\mathcal{L}_E$, $\mathcal{L}_H$ and $\mathcal{L}_A$) and correspond to the vector fields ($\mathbf{E_k}(\mathbf{r})$, $\mathbf{H_k}(\mathbf{r})$ and $\mathbf{A_k}(\mathbf{r})$). The eigenvectors $\mathbf{F_k}(\mathbf{r})$ are the field patterns of the harmonic modes and the eigenvalues $(\omega_\mathbf{k}/c)^2$ are proportional to the squared eigenfrequencies, $\omega_\mathbf{k}$, of those modes. The subscript $\mathbf{k}$ labels the avaliable solutions and it may run through discrete or continuous values.

### 2.1.3 Normal modes expansion

A differential operator $\mathcal{L}$ is a Hermitian operator, if $\langle \mathcal{L}\mathbf{F}, \mathbf{G}\rangle = \langle \mathbf{F}, \mathcal{L}\mathbf{G}\rangle$ holds for any vector fields $\mathbf{F}(\mathbf{r})$ and $\mathbf{G}(\mathbf{r})$. Here the inner product of two complex vectorial functions $\mathbf{F}(\mathbf{r})$ and $\mathbf{G}(\mathbf{r})$ is defined by

$$\langle \mathbf{F}, \mathbf{G}\rangle \equiv \int d^3\mathbf{r}\mathbf{F}(\mathbf{r}) \cdot \mathbf{G}^*(\mathbf{r}), \tag{2.20}$$

where $^*$ denotes the complex conjugate.

It is a simple exercise to show that the differential operator $\mathcal{L}_H$ in (2.18) is a Hermitian operator, while differential operators $\mathcal{L}_E$ (2.17) and $\mathcal{L}_A$ (2.19) are not Hermitian.

An important property of the Hermitian eigenvalue problem is that the eigenfunctions of a Hermitian operator form a complete set of orthogonal functions. Then, any solution of the wave equation (2.8,2.18) can be expanded in terms of these eigenfunctions (normal modes)

$$\mathbf{H}(\mathbf{r}, t) = \sum_\mathbf{k} \int d^3\mathbf{k} C_\mathbf{k}(t)\mathbf{H_k}(\mathbf{r}), \tag{2.21}$$

where $C_\mathbf{k}(t)$ are the time-dependent amplitude coefficients, the summation is over a discrete value of index $\mathbf{k}$, while the integration is over continuous values of index $\mathbf{k}$. For a Hermitian eigenvalue problem the orthogonality, the normalization and the completeness conditions are given by:

$$\int d^3\mathbf{r}\mathbf{H_k}(\mathbf{r}) \cdot \mathbf{H}^*_{\mathbf{k}'}(\mathbf{r}) = \delta(\mathbf{k} - \mathbf{k}'), \tag{2.22}$$

$$\sum_\mathbf{k} \int d^3\mathbf{k}\mathbf{H_k}(\mathbf{r}) \cdot \mathbf{H}^*_\mathbf{k}(\mathbf{r}') = \delta(\mathbf{r} - \mathbf{r}'), \tag{2.23}$$

where $\delta$ is the Dirac delta function.

Another important property of the Hermitian eigenvalue problem (2.18) is that the eigenfunction $\mathbf{H_k}(\mathbf{r})$ must have a real eigenfrequency $\omega_\mathbf{k}$. In fact, taking the inner product of equation (2.18) with the eigenfunction $\mathbf{H_k}(\mathbf{r})$ and taking into account that for a Hermitian operator $\mathcal{L}$, $\langle \mathcal{L}\mathbf{F}, \mathbf{G}\rangle = \langle \mathbf{F}, \mathcal{L}\mathbf{G}\rangle$, and for any operator $\mathcal{F}$, $\langle \mathcal{F}\mathbf{F}, \mathbf{G}\rangle^* =$

$\langle \mathbf{F}, \mathcal{F}\mathbf{G} \rangle$, one has:

$$\langle \mathbf{H_k}, \mathcal{L}_H \mathbf{H_k} \rangle^* = \left( \frac{\omega_\mathbf{k}^2}{c^2} \right)^* \langle \mathbf{H_k}, \mathbf{H_k} \rangle = \langle \mathcal{L}_H \mathbf{H_k}, \mathbf{H_k} \rangle = \left( \frac{\omega_\mathbf{k}^2}{c^2} \right) \langle \mathbf{H_k}, \mathbf{H_k} \rangle .$$

So, it follows that $(\omega_\mathbf{k}^2)^* = \omega_\mathbf{k}^2$, or that $\omega_\mathbf{k}^2$ is real. Further, one can show that [2]

$$\left( \frac{\omega_\mathbf{k}^2}{c^2} \right) \langle \mathbf{H_k}, \mathbf{H_k} \rangle = \langle \mathbf{H_k}, \mathcal{L}_H \mathbf{H_k} \rangle = \int d^3\mathbf{r} \frac{1}{\varepsilon(\mathbf{r})} \left| \nabla \times \mathbf{H_k}(\mathbf{r}) \right|^2 .$$

Since dielectric function $\varepsilon(\mathbf{r})$ is positive everywhere, the integrand on the right-hand side is also positive everywhere. Therefore all $\omega_\mathbf{k}^2$ must be positive, and eigenfrequency $\omega_\mathbf{k}$ is real.

### 2.1.4 Eigenvalue problem for the vector potential

The differential operator $\mathcal{L}_A$ of the vector potential eigenvalue problem (2.19) is not a Hermitian operator. At the same time, the full set of the eigenfunctions of equation (2.19) can be chosen to fulfill the orthogonality condition [8, 9, 10]. These eigenfunctions $\mathbf{A_k}(\mathbf{r})$ obey the gauge condition (2.12), $\nabla \cdot [\varepsilon(\mathbf{r}) \mathbf{A_k}(\mathbf{r})] = 0$, and are therefore transverse with respect to this gauge. Here any vector that satisfies the $\varepsilon$-transverse gauge condition (2.12) is called "$\varepsilon$-transverse" [9]. Then, an arbitrary $\varepsilon$-transverse solution of the wave equation (2.15), which satisfies the gauge condition (2.12), can be expanded in terms of the eigenfunctions $\mathbf{A_k}(\mathbf{r})$ (normal modes)

$$\mathbf{A}(\mathbf{r}, t) = \sum_\mathbf{k} \int d^3\mathbf{k} C_\mathbf{k}(t) \mathbf{A_k}(\mathbf{r}), \tag{2.24}$$

where $C_\mathbf{k}(t)$ are again the time-dependent amplitude coefficients. The same applies to the eigenvalue problem of the electric field (2.17), since differential operators $\mathcal{L}_E$ and $\mathcal{L}_A$ are identical.

That property follows from the observation that for the vector functions

$$\mathbf{Q_k}(\mathbf{r}) \equiv \sqrt{\varepsilon(\mathbf{r})} \mathbf{A_k}(\mathbf{r}) , \tag{2.25}$$

equation (2.19) can be written in the form of a Hermitian eigenvalue problem

$$\mathcal{L}_Q \mathbf{Q_k}(\mathbf{r}) = \frac{\omega_\mathbf{k}^2}{c^2} \mathbf{Q_k}(\mathbf{r}) . \tag{2.26}$$

The differential operator

$$\mathcal{L}_Q \mathbf{Q}_\mathbf{k}(\mathbf{r}) \equiv \frac{1}{\sqrt{\varepsilon(\mathbf{r})}} \nabla \times \left\{ \nabla \times \frac{1}{\sqrt{\varepsilon(\mathbf{r})}} \mathbf{Q}_\mathbf{k}(\mathbf{r}) \right\} \tag{2.27}$$

is Hermitian and its eigenfunctions $\mathbf{Q}_\mathbf{k}(\mathbf{r})$ are complete and orthogonal [8, 9, 10]. This leads to the following orthogonality and normalization condition for the eigenfunctions $\mathbf{A}_\mathbf{k}(\mathbf{r})$

$$\int d^3\mathbf{r} \varepsilon(\mathbf{r}) \mathbf{A}_\mathbf{k}(\mathbf{r}) \cdot \mathbf{A}^*_{\mathbf{k}'}(\mathbf{r}) = \delta(\mathbf{k} - \mathbf{k}'), \tag{2.28}$$

where orthogonality condition (2.22) and the definition of the vector functions $\mathbf{Q}_\mathbf{k}(\mathbf{r})$ (2.25) were used.

The eigenfunctions $\mathbf{Q}_\mathbf{k}(\mathbf{r})$ obviously provide a complete set in the subset of functions, that is defined by the gauge condition $\nabla \cdot [\sqrt{\varepsilon(\mathbf{r})} \mathbf{Q}_\mathbf{k}(\mathbf{r})] = 0$. For these functions the completeness condition is defined as

$$\sum_\mathbf{k} \int d^3\mathbf{k} \mathbf{Q}_\mathbf{k}(\mathbf{r}) \cdot \mathbf{Q}^*_\mathbf{k}(\mathbf{r}') = \mathcal{I} \delta(\mathbf{r} - \mathbf{r}'), \tag{2.29}$$

where $\mathcal{I}$ is an identity operator on this subset of functions [8]. In analogy, the completeness condition for the $\varepsilon$-transverse eigenfunctions $\mathbf{A}_\mathbf{k}(\mathbf{r})$ can be introduced as [8]:

$$\sum_\mathbf{k} \int d^3\mathbf{k} \mathbf{A}_\mathbf{k}(\mathbf{r}) \cdot \mathbf{A}^*_\mathbf{k}(\mathbf{r}') = \mathcal{I}_{\varepsilon_\perp} \delta(\mathbf{r} - \mathbf{r}'), \tag{2.30}$$

where $\mathcal{I}_{\varepsilon_\perp}$ is an identity operator on the subset of the $\varepsilon$-transverse functions. The action of $\mathcal{I}_{\varepsilon_\perp} \delta(\mathbf{r} - \mathbf{r}')$ can be explained as follows. Let $\mathbf{F}^T$ denotes an arbitrary transverse vector field, $\nabla \cdot \mathbf{F}^T = 0$, and $\mathbf{F}^L$ denotes an arbitrary longitudinal vector field, $\nabla \times \mathbf{F}^L = 0$. Then the following relations hold

$$\int d^3\mathbf{r}' \mathcal{I}_{\varepsilon_\perp} \delta(\mathbf{r} - \mathbf{r}') \mathbf{F}^T(\mathbf{r}') = \mathbf{F}^T(\mathbf{r}), \tag{2.31}$$

$$\int d^3\mathbf{r}' \mathcal{I}_{\varepsilon_\perp} \delta(\mathbf{r} - \mathbf{r}') \mathbf{F}^L(\mathbf{r}') = 0. \tag{2.32}$$

### 2.1.5 Normal modes expansion of dipole field

A general time-dependent electromagnetic field produced by an arbitrary current distribution, $\mathbf{J}$, is governed by Maxwell's equations in the form

$$\nabla \times \mathbf{E} = -\frac{1}{c} \frac{\partial \mathbf{H}}{\partial t}, \tag{2.33}$$

$$\nabla \times \mathbf{H} = \frac{1}{c} \varepsilon(\mathbf{r}) \frac{\partial \mathbf{E}}{\partial t} + \frac{4\pi}{c} \mathbf{J}, \tag{2.34}$$

$$\nabla \cdot [\varepsilon(\mathbf{r})\mathbf{E}] = 0, \tag{2.35}$$

$$\nabla \cdot \mathbf{H} = 0. \tag{2.36}$$

Then in the generalized Coulomb gauge (2.12), the inhomogeneous wave equation for the vector potential $\mathbf{A}$ can be written as:

$$\nabla \times \nabla \times \mathbf{A} + \frac{1}{c^2}\varepsilon(\mathbf{r})\frac{\partial^2 \mathbf{A}}{\partial t^2} = \frac{4\pi}{c}\mathbf{J}. \tag{2.37}$$

An important example of the current density distribution, $\mathbf{J}$, is a harmonically oscillating dipole:

$$\mathbf{J}(\mathbf{r}, t) = -i\omega_0 \mathbf{d}\delta(\mathbf{r} - \mathbf{r}_0)e^{-i\omega_0 t}. \tag{2.38}$$

Here, $\omega_0$ is a frequency, $\mathbf{d}$ is a real dipole moment and $\mathbf{r}_0$ is a location of the dipole inside an inhomogeneous medium. A point dipole (2.38) suites as a good basic model for many electrodynamic problems, where radiation of electromagnetic waves is considered.

A solution of the inhomogeneous wave equation (2.37) can be constructed by a suitable superposition of the eigenfunctions of the homogeneous wave equation (2.15). Then the field of the point dipole (2.38) is given by the normal modes expansion (2.24) and the amplitude coefficients $C_{\mathbf{k}}(t)$ can be easily obtained from the wave equation (2.37). Substituting (2.24) into the wave equation (2.37) and using the homogeneous wave equation (2.15), one obtains

$$\int d^3\mathbf{k} \left( \frac{\partial^2 C_{\mathbf{k}}(t)}{\partial t^2} + \omega_{\mathbf{k}}^2 C_{\mathbf{k}}(t) \right) \varepsilon(\mathbf{r})\mathbf{A}_{\mathbf{k}}(\mathbf{r}) \quad = 4\pi c \mathbf{J}(\mathbf{r}, t).$$

Then taking the inner product between every term of this equation and an eigenfunction $\mathbf{A}_{\mathbf{k}'}(\mathbf{r})$, i.e., multiplying by $\mathbf{A}^*_{\mathbf{k}'}(\mathbf{r})$ and integrating over the inhomogeneous medium, one finally obtains the differential equation for the amplitude coefficients $C_{\mathbf{k}}(t)$

$$\frac{\partial^2 C_{\mathbf{k}}(t)}{\partial t^2} + \omega_{\mathbf{k}}^2 C_{\mathbf{k}}(t) = -i\frac{4\pi c\omega_0}{V} \left( \mathbf{A}^*_{\mathbf{k}}(\mathbf{r}_0) \cdot \mathbf{d} \right) e^{-i\omega_0 t},$$

where the orthogonality of the eigenfunctions (2.28) and a specific form of the source term (2.38) were taken into account. Then assuming the initial conditions $C_{\mathbf{k}}(0) = 0$, one has the following solution of this differential equation

$$C_{\mathbf{k}}(t) = -i\frac{4\pi c\omega_0}{V} \frac{(\mathbf{A}^*_{\mathbf{k}}(\mathbf{r}_0) \cdot \mathbf{d})}{(\omega_{\mathbf{k}}^2 - \omega_0^2)} e^{-i\omega_0 t}. \tag{2.39}$$

Finally, the electromagnetic field radiated by a point dipole located at $\mathbf{r}_0$ can be rep-

resented in terms of normal modes as:

$$\mathbf{A}(\mathbf{r},t) = -i\frac{4\pi c\omega_0}{V}\int d^3\mathbf{k}\frac{(\mathbf{A}^*_{\mathbf{k}}(\mathbf{r}_0)\cdot\mathbf{d})\,\mathbf{A}_{\mathbf{k}}(\mathbf{r})}{(\omega^2_{\mathbf{k}}-\omega^2_0)}e^{-i\omega_0 t}. \tag{2.40}$$

The integrand in (2.40) has a pole at $\omega^2_{\mathbf{k}} = \omega^2_0$, and the integral is singular. This is a typical behavior for any resonant system, where dissipation is neglected. The standard way to regularize the integral is to add a small imaginary part to $\omega^2_0$. A regularized integral reads

$$\mathbf{A}(\mathbf{r},t) = -i\frac{4\pi c\omega_0}{V}\int d^3\mathbf{k}\frac{(\mathbf{A}^*_{\mathbf{k}}(\mathbf{r}_0)\cdot\mathbf{d})\,\mathbf{A}_{\mathbf{k}}(\mathbf{r})}{(\omega^2_{\mathbf{k}}-\omega^2_0-i\gamma)}e^{-i\omega_0 t}. \tag{2.41}$$

## 2.2 Periodic dielectric media

### 2.2.1 Translational symmetry

Being an optical analogy of crystalline solids, a photonic crystal is a space lattice built of basic blocks, "atoms", which are macroscopic dielectric materials. The lattice is characterized by space periodicity or *translational symmetry*. This means that there exist basis vectors, $\mathbf{a}_1$, $\mathbf{a}_2$, $\mathbf{a}_3$, such that the dielectric structure remains invariant under translation through any vector which is the sum of integer multiples of these vectors. The *primitive unit vectors* $\mathbf{a}_\alpha$, $\alpha = 1,\ 2,\ 3$, are the shortest vectors by which a crystal can be displaced and be brought back to itself. If the origin of the coordinate system coincides with a lattice site, the position vector of any other site is given by

$$\mathbf{R} = l_1\mathbf{a}_1 + l_2\mathbf{a}_2 + l_3\mathbf{a}_3, \tag{2.42}$$

where $l_\alpha$ ($\alpha = 1, 2, 3$) are integers (Fig. 2.1). Then, an actual crystal consists of endless repetitions of "atoms", or group of "atoms", placed similarly about each lattice site.

It is obvious that the whole crystal can be defined if the contents of a single *unit cell* is specified—for example, the parallelepiped subtended by the primitive vectors $\mathbf{a}_1$, $\mathbf{a}_2$, $\mathbf{a}_3$ (Fig. 2.1). The whole crystal is made up of repetitions of this object stacked like bricks in a wall. A possible choice of the primitive vectors, and thus the unit cell, is to some extent arbitrary. At the same time, the volume of the unit cell remains the same for any possible choice of the primitive vectors, and is given by $V = \mathbf{a}_1\cdot(\mathbf{a}_2\times\mathbf{a}_3)$. An example of alternative unit cells in a two-dimensional lattice is shown in figure 2.1. An important choice of the unit cell is the Wigner-Seitz cell, constructed by drawing the perpendicular bisector planes of the translation vectors from the chosen center to the nearest equivalent lattice cites. The Wigner-Seitz cell is shown in figure 2.1 as a grey region.

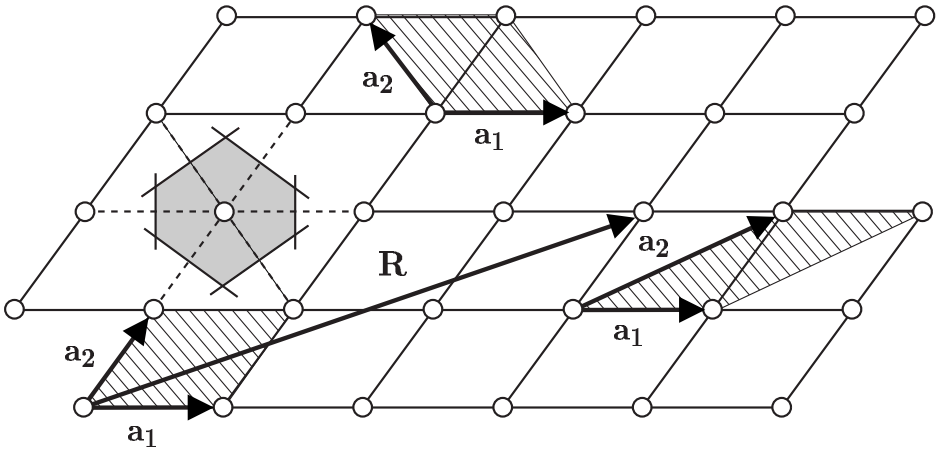


Figure 2.1: Alternative unit cells (hatched regions) in a two-dimensional triangular lattice. The Wigner-Seitz cell is shown (grey region).

The unit cell can contain one or more "atoms". Naturally, if it contains only one "atom", it is centered at the lattice site, and the lattice is called a *Bravais lattice*. If there are several atoms per unit cell, than the lattice is called a *lattice with a basis*.

### 2.2.2 Periodic functions and reciprocal lattice

The optical properties of a dielectric non-magnetic photonic crystal are described by its dielectric function, which, reflecting the translation symmetry of the lattice, must be a periodic function:

$$\varepsilon(\mathbf{r}+\mathbf{R}) = \varepsilon(\mathbf{r}) \tag{2.43}$$

for all points $\mathbf{r}$ in space and for all lattice translations $\mathbf{R}$ (2.42).

It is natural to analyze periodic functions by taking their Fourier transform. That is, the periodic function $\varepsilon(\mathbf{r})$ is build out of the plane waves with various wave vectors:

$$\varepsilon(\mathbf{r}) = \int d\mathbf{q}\, g(\mathbf{q})\, \exp(i\mathbf{q}\cdot\mathbf{r}). \tag{2.44}$$

Here $g(\mathbf{q})$ is the coefficient on the plane wave with the wave vector $\mathbf{q}$. Requiring the translation symmetry of the dielectric function (2.43) in the expansion (2.44) yields

$$\varepsilon(\mathbf{r}+\mathbf{R}) = \int d\mathbf{q}\, g(\mathbf{q})\, \exp(i\mathbf{q}\cdot\mathbf{r})\, \exp(i\mathbf{q}\cdot\mathbf{R}) = \int d\mathbf{q}\, g(\mathbf{q})\, \exp(i\mathbf{q}\cdot\mathbf{r}). \tag{2.45}$$

That is, the periodicity of the function $\varepsilon(\mathbf{r})$ implies that its Fourier transform $g(\mathbf{q})$ has the special property $g(\mathbf{q}) = g(\mathbf{q})\, \exp(i\mathbf{q}\cdot\mathbf{R})$, which is possible only if $g(\mathbf{q}) = 0$ or $\exp(i\mathbf{q}\cdot\mathbf{R}) = 1$. In other words, the transform $g(\mathbf{q})$ is zero everywhere, except for the values of $\mathbf{q}$ such that $\exp(i\mathbf{q}\cdot\mathbf{R}) = 1$ for all $\mathbf{R}$. This means, to build a lattice-

periodic function, one needs only those plane waves with wave vectors $\mathbf{q}$ such that $\exp(i\mathbf{q}\cdot\mathbf{R}) = 1$, or equivalently, $\mathbf{q}\cdot\mathbf{R} = 2\pi l$, for all of the lattice vectors $\mathbf{R}$ and integer $l$.

Those vectors $\mathbf{q}$ are called *reciprocal lattice vectors* and are usually designated by the letter $\mathbf{G}$. The reciprocal vectors form a lattice of their own, that is, the sum of integral multiples of these vectors yields another reciprocal lattice vector. To construct reciprocal lattice vectors, for a given crystal lattice, the requirement $\mathbf{GR} = 2\pi l$ should be satisfied, for all of the lattice vectors $\mathbf{R}$ and integer $l$. Using the primitive unit vectors, $\mathbf{a}_\alpha$, and primitive reciprocal unit vectors, $\mathbf{b}_\beta$, this requirement boils down to the form

$$\mathbf{GR} = (l_1\mathbf{a}_1 + l_2\mathbf{a}_2 + l_3\mathbf{a}_3)(m_1\mathbf{b}_1 + m_2\mathbf{b}_2 + m_3\mathbf{b}_3) = 2\pi l,$$

where $l_\alpha$, $m_\beta$ $(\alpha, \beta = 1,\ 2,\ 3)$ and $l$ are integers. This requirement can be satisfied, if the primitive reciprocal vectors $\mathbf{b}_\beta$ are constructed so that $\mathbf{a}_\alpha\mathbf{b}_\beta = 2\pi\delta_{\alpha\beta}$, which can be easily done as follows:

$$\mathbf{b}_1 = \frac{2\pi}{V}\left(\mathbf{a}_2 \times \mathbf{a}_3\right),\ \mathbf{b}_2 = \frac{2\pi}{V}\left(\mathbf{a}_3 \times \mathbf{a}_1\right),\ \mathbf{b}_3 = \frac{2\pi}{V}\left(\mathbf{a}_1 \times \mathbf{a}_2\right), \tag{2.46}$$

where $V$ is the volume of the unit cell of the direct lattice. The parallelepiped constructed from the primitive reciprocal vectors $\mathbf{b}_\beta$ is called the unit cell of reciprocal lattice. The space where the reciprocal lattice exists is called *reciprocal space*.

In summary, when the Fourier transform of a lattice-periodic function $\varepsilon(\mathbf{r})$ is taken, one only needs to include terms with wave vectors that are reciprocal lattice vectors, as follows

$$\varepsilon(\mathbf{r}) = \sum_{\mathbf{G}} \varepsilon\left(\mathbf{G}\right)\exp(i\mathbf{G}\cdot\mathbf{r}), \tag{2.47}$$

with the Fourier coefficients given by:

$$\varepsilon\left(\mathbf{G}\right) = \frac{1}{V}\int_V d^3\mathbf{r}\varepsilon(\mathbf{r})\exp(-i\mathbf{G}\cdot\mathbf{r}). \tag{2.48}$$

### 2.2.3 Translation symmetry and Bloch theorem

In the case of an unbounded periodic medium (2.43), the differential operator $\mathcal{L}_H$ (2.18) is translationaly invariant:

$$\mathcal{L}_H\left(\mathbf{r}+\mathbf{R}\right) = \mathcal{L}_H\left(\mathbf{r}\right), \tag{2.49}$$

for all points $\mathbf{r}$ in space and for all lattice translations $\mathbf{R}$ (2.42). For the lattice translation $\mathbf{R}$ (2.42) one can introduce the translation operator $T_{\mathbf{R}}$ such that

$$T_{\mathbf{R}} f\left(\mathbf{r}\right) = f\left(\mathbf{r}+\mathbf{R}\right), \tag{2.50}$$

where $f(\mathbf{r})$ is an arbitrary function. Then an application of the translation operator $T_{\mathbf{R}}$ to the eigenvalue equation (2.18) gives

$$\begin{aligned} T_{\mathbf{R}}\mathcal{L}_H(\mathbf{r})\,\mathbf{H}_{\mathbf{k}}(\mathbf{r}) &= \mathcal{L}_H(\mathbf{r}+\mathbf{R})\,\mathbf{H}_{\mathbf{k}}(\mathbf{r}+\mathbf{R}) \\ &= \mathcal{L}_H(\mathbf{r})\,\mathbf{H}_{\mathbf{k}}(\mathbf{r}+\mathbf{R}) \\ &= \mathcal{L}_H(\mathbf{r})\,T_{\mathbf{R}}\mathbf{H}_{\mathbf{k}}(\mathbf{r}) \end{aligned}$$

which is valid for any eigenfunction $\mathbf{H}_{\mathbf{k}}(\mathbf{r})$. This simply means that translation operators commute with the operator $\mathcal{L}_H$

$$T_{\mathbf{R}}\mathcal{L}_H = \mathcal{L}_H T_{\mathbf{R}}. \tag{2.51}$$

At the same time, the translation operators commute among themselves. Then, eigenfunctions of the operator $\mathcal{L}_H$ can be find in a way to be simultaneously eigenfunctions of both operators $\mathcal{L}_H$ and $T_{\mathbf{R}}$ for all lattice translations $\mathbf{R}$ (e.g. [11]):

$$\mathcal{L}_H\mathbf{H}_{\mathbf{k}}(\mathbf{r}) = \left(\frac{\omega_{\mathbf{k}}}{c}\right)^2 \mathbf{H}_{\mathbf{k}}(\mathbf{r}), \tag{2.52}$$

$$T_{\mathbf{R}}\mathbf{H}_{\mathbf{k}}(\mathbf{r}) = c(\mathbf{R})\,\mathbf{H}_{\mathbf{k}}(\mathbf{r}). \tag{2.53}$$

Applying two successive translations to the eigenfunction $\mathbf{H}_{\mathbf{k}}(\mathbf{r})$ one has

$$T_{\mathbf{R}}T_{\mathbf{R}'}\mathbf{H}_{\mathbf{k}}(\mathbf{r}) = c(\mathbf{R})\,T_{\mathbf{R}'}\mathbf{H}_{\mathbf{k}}(\mathbf{r}) = c(\mathbf{R})\,c(\mathbf{R}')\,\mathbf{H}_{\mathbf{k}}(\mathbf{r}).$$

Due to the fact, that for two arbitrary translations, $T_{\mathbf{R}}T_{\mathbf{R}'} = T_{\mathbf{R}+\mathbf{R}'}$, the eigenvalue of the resulting transformation is

$$T_{\mathbf{R}}T_{\mathbf{R}'}\mathbf{H}_{\mathbf{k}}(\mathbf{r}) = T_{\mathbf{R}+\mathbf{R}'}\mathbf{H}_{\mathbf{k}}(\mathbf{r}) = c(\mathbf{R}+\mathbf{R}')\,\mathbf{H}_{\mathbf{k}}(\mathbf{r}).$$

Then, eigenvalues of the translation operators $T_{\mathbf{R}}$ obey the relation

$$c(\mathbf{R}+\mathbf{R}') = c(\mathbf{R})\,c(\mathbf{R}'). \tag{2.54}$$

For the primitive unit translation in the basic direction $\mathbf{a}_\alpha$, the eigenvalue of the corresponding translation operator can be chosen in the form

$$c(\mathbf{a}_\alpha) = \exp(ik_\alpha l_\alpha).$$

Then for the translation operator $T_{\mathbf{R}}$ the eigenvalue can be written as

$$c(\mathbf{R}) = \exp(i\mathbf{k}\cdot\mathbf{R}),$$

where a vector $\mathbf{k}$ is defined by

$$\mathbf{k} = k_1\mathbf{b}_1 + k_2\mathbf{b}_2 + k_3\mathbf{b}_3$$

and $\mathbf{b}_1$, $\mathbf{b}_2$ , $\mathbf{b}_3$ are the primitive reciprocal lattice vectors (2.46).

Now, applying an arbitrary lattice translation $\mathbf{R}$ to the eigenfunction $\mathbf{H}_\mathbf{k}(\mathbf{r})$ one obtains

$$T_\mathbf{R}\mathbf{H}_\mathbf{k}(\mathbf{r}) = \mathbf{H}_\mathbf{k}(\mathbf{r}+\mathbf{R}) = c(\mathbf{R})\,\mathbf{H}_\mathbf{k}(\mathbf{r}) = e^{i\mathbf{k}\cdot\mathbf{R}}\mathbf{H}_\mathbf{k}(\mathbf{r}),$$

which leads to the ***Bloch's theorem*****:** *for any eigenfunction* $\mathbf{H}_\mathbf{k}(\mathbf{r})$ *of the wave equation (2.8,2.18) with periodic dielectric function* $\varepsilon(\mathbf{r})$*, there exists a vector* $\mathbf{k}$ *such that translation by a lattice vector* $\mathbf{R}$ *is equivalent to the multiplying by the phase factor* $\exp(i\mathbf{kR})$,

$$\mathbf{H}_\mathbf{k}(\mathbf{r}+\mathbf{R}) = e^{i\mathbf{k}\cdot\mathbf{R}}\mathbf{H}_\mathbf{k}(\mathbf{r}). \tag{2.55}$$

### 2.2.4 Bloch eigenwaves

There is another common way to formulate the ***Bloch's theorem:*** *the eigenfunction* $\mathbf{H}_\mathbf{k}(\mathbf{r})$ *of the wave equation (*2.8,2.18*) with periodic dielectric function* $\varepsilon(\mathbf{r})$*, can be chosen to have the form of a plane wave times a vector function with the periodicity of the lattice:*

$$\mathbf{H}_\mathbf{k}(\mathbf{r}) = \mathbf{h}_\mathbf{k}(\mathbf{r})\,e^{i\mathbf{k}\cdot\mathbf{r}}, \tag{2.56}$$

*where*

$$\mathbf{h}_\mathbf{k}(\mathbf{r}+\mathbf{R}) = \mathbf{h}_\mathbf{k}(\mathbf{r}) \tag{2.57}$$

*for all points* $\mathbf{r}$ *in space and all lattice translations* $\mathbf{R}$*.*

To prove (2.56-2.57), one simply substitutes (2.56) in (2.55)

$$\mathbf{H}_\mathbf{k}(\mathbf{r}+\mathbf{R}) = \mathbf{h}_\mathbf{k}(\mathbf{r}+\mathbf{R})\,e^{i\mathbf{k}\cdot(\mathbf{r}+\mathbf{R})} = e^{i\mathbf{k}\cdot\mathbf{R}}\mathbf{h}_\mathbf{k}(\mathbf{r})\,e^{i\mathbf{k}\cdot\mathbf{r}},$$

which gives condition (2.57) on the periodic vector function $\mathbf{h}_\mathbf{k}(\mathbf{r})$.

Eigenfunctions (2.56) of the eigenvalue problem (2.8,2.18) are called the *Bloch eigenwaves*, or simply, the *Bloch waves* and they are the eigenmodes of a periodic medium. Bloch waves form a complete set of orthogonal functions (Sec. 2.1.3), which satisfy the Bloch theorem. Then, any solution of the wave equation (2.8,2.18) with periodic dielectric function, $\varepsilon(\mathbf{r})$, can be found as a superposition of the Bloch waves (Sec. 2.1.3).

It is instructive to present the Bloch wave as a superposition of the plane waves. Due to the lattice periodicity of the functions $\mathbf{h}_\mathbf{k}(\mathbf{r})$, their Fourier expansion leads to

(Sec. 2.2.2)

$$\mathbf{h_k}(\mathbf{r}) = \sum_{\mathbf{G}} \mathbf{h_k}(\mathbf{G}) \exp(i\mathbf{G}\cdot\mathbf{r}), \tag{2.58}$$

where summation is over reciprocal lattice vectors and Fourier coefficients are given by:

$$\mathbf{h_k}(\mathbf{G}) = \frac{1}{V}\int_V d^3\mathbf{r}\mathbf{h_k}(\mathbf{r}) \exp(-i\mathbf{G}\cdot\mathbf{r}). \tag{2.59}$$

Then, the Bloch waves (2.56) can be represented in the terms of plane waves

$$\mathbf{H_k}(\mathbf{r}) = \sum_{\mathbf{G}} \mathbf{h_k}(\mathbf{G}) \exp(i(\mathbf{k}+\mathbf{G})\cdot\mathbf{r}). \tag{2.60}$$

The periodic dielectric function can be also expanded in the Fourier series

$$\varepsilon^{-1}(\mathbf{r}) = \sum_{\mathbf{G}} \widetilde{\varepsilon}(\mathbf{G}) \exp(i\mathbf{G}\cdot\mathbf{r}), \tag{2.61}$$

where the Fourier coefficients are given by:

$$\widetilde{\varepsilon}\,(\mathbf{G}) = \frac{1}{V}\int_V d^3\mathbf{r}\varepsilon^{-1}(\mathbf{r}) \exp(-i\mathbf{G}\cdot\mathbf{r}). \tag{2.62}$$

Substituting (2.60) and (2.61) in the wave equation (2.18), an infinite linear system of homogenous equations for the unknown Fourier coefficients $\mathbf{h_k}(\mathbf{G})$ is obtained:

$$-\sum_{\mathbf{G}'} \widetilde{\varepsilon}(\mathbf{G}-\mathbf{G}')(\mathbf{k}+\mathbf{G}) \times \{(\mathbf{k}+\mathbf{G}') \times \mathbf{h_k}(\mathbf{G}')\} = \frac{\omega_{\mathbf{k}}^2}{c^2}\mathbf{h_k}(\mathbf{G}). \tag{2.63}$$

By solving these set of equations numerically, one can obtain the dispersion relation of the eigenfunctions [1, 2]. This numerical method, based on the Fourier expansion of the electromagnetic field and the dielectric function, is called the plane-wave expansion (PWE) method. It will be discussed in more details in chapter 3.

### 2.2.5 Existence of photonic band structure

In general the Bloch theorem should be written in the following form

$$\mathbf{H}_{n\mathbf{k}}(\mathbf{r}) = \mathbf{h}_{n\mathbf{k}}(\mathbf{r})\, e^{i\mathbf{k}\cdot\mathbf{r}}, \tag{2.64}$$

where the index $n$ appears because for the given $\mathbf{k}$ there may be many solutions of the wave equation (2.8,2.18). Here, it is assumed that index $\mathbf{k}$ is fixed and a vector function $\mathbf{h}_{n\mathbf{k}}(\mathbf{r})$ is a periodic function on the crystal lattice. Then, the function $\mathbf{h}_{n\mathbf{k}}(\mathbf{r})$

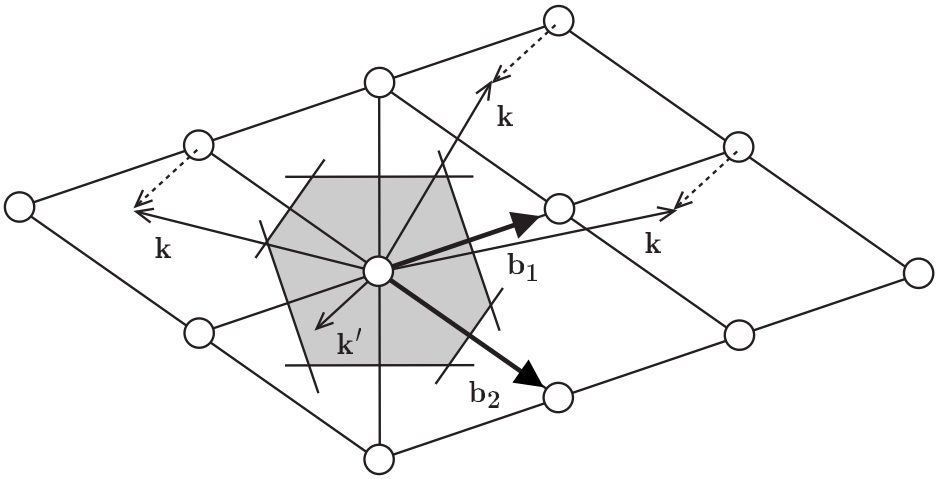


Figure 2.2: The reciprocal lattice of the two-dimensional triangular lattice (Fig. 2.1). All wave vectors $\mathbf{k}$ are reduced to the wave vector $\mathbf{k}'$, which lies in the first Brillouin zone (grey region).

is determined by the following eigenvalue problem

$$(\nabla + i\mathbf{k}) \times \left\{ \frac{1}{\varepsilon(\mathbf{r})} (\nabla + i\mathbf{k}) \times \mathbf{h}_{n\mathbf{k}}(\mathbf{r}) \right\} = \left( \frac{\omega_{\mathbf{k}}}{c} \right)^2 \mathbf{h}_{n\mathbf{k}}(\mathbf{r}) \tag{2.65}$$

with the periodic boundary condition (2.57)

$$\mathbf{h}_{n\mathbf{k}}(\mathbf{r} + \mathbf{R}) = \mathbf{h}_{n\mathbf{k}}(\mathbf{r}) . \tag{2.66}$$

Because of the periodic boundary condition, one can regard (2.65-2.66) as an Hermitian eigenvalue problem restricted to a single primitive cell of the crystal. Moreover, since the eigenvalue problem is set in a fixed volume, an infinite family of solutions with discretely spaced eigenvalues is expected. These discrete solutions are labeled with the band index $n$.

In the same time, the wave vector $\mathbf{k}$ appears only as a parameter in the eigenvalue problem (2.65-2.66). Then, each of the discrete eigenvalues is expected to vary continously as the wave vector varies. In this way, a family of continuous functions (dispersion relations) $\omega = \omega_n(\mathbf{k})$ is defined. These functions are labeled in order of increasing frequency by the band index. The information contained in the dispersion relations is called the *photonic band structure* of the photonic crystal. In addition, as it will be shown by direct examples in chapter 3, continuous branches $\omega = \omega_n(\mathbf{k})$ can be generally separated by a forbidden frequency gap [12, 13].

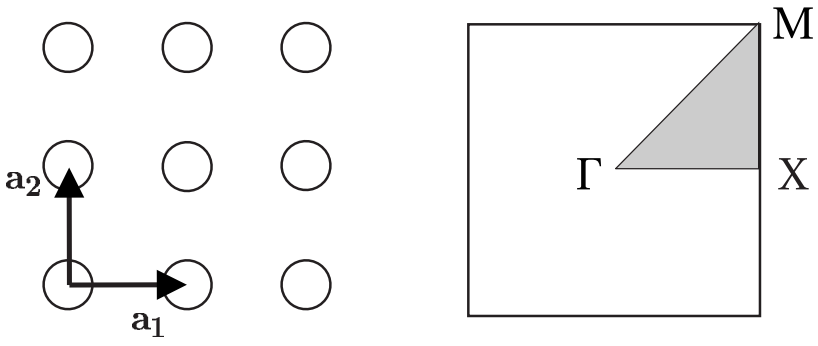


Figure 2.3: A two-dimensional square lattice (left) and the corresponding first Brillouin zone (right). The irreducible zone is the grey triangular wedge. The special point at the center, corner and face of the first Brillouin zone are conventionally known as Γ, M and X.

### 2.2.6 Brillouin zone

One important feature of the Bloch waves is that different values of the wave vector $\mathbf{k}$ do not necessarily lead to different eigenwaves. In fact, for an eigenwave with the wave vector $\mathbf{k} = \mathbf{k}' + \mathbf{G}$, where $\mathbf{G}$ is a reciprocal lattice vector, the Bloch's theorem (2.55) reads

$$\begin{aligned} \mathbf{H}_{n\mathbf{k}}(\mathbf{r}+\mathbf{R}) &= e^{i(\mathbf{k}'+\mathbf{G})\cdot\mathbf{R}}\mathbf{H}_{n\mathbf{k}}(\mathbf{r}) \\ &= e^{i\mathbf{k}'\cdot\mathbf{R}}e^{i\mathbf{G}\cdot\mathbf{R}}\mathbf{H}_{n\mathbf{k}}(\mathbf{r}) = e^{i\mathbf{k}'\cdot\mathbf{R}}\mathbf{H}_{n\mathbf{k}}(\mathbf{r}). \end{aligned}$$

Here the last equality is due to Eq. (2.45). This relation means, that the eigenwave $\mathbf{H}_{n\mathbf{k}}(\mathbf{r})$ satisfies the Bloch's theorem as it had the wave vector $\mathbf{k}'$. So, the original label $\mathbf{k}$ is not unique: *every eigenwave has a whole host of possible wave vectors, differing from one another by the vectors of the reciprocal lattice.*

It is common to choose the value of $\mathbf{G}$ in $\mathbf{k} = \mathbf{k}' + \mathbf{G}$ to make $|\mathbf{k}'|$ as small as possible, i. e., to lie as near to the origin of the reciprocal lattice as it can. This means that $|\mathbf{k}'|$ is to lie nearer to the origin than to any other sites of the reciprocal lattice, which amounts to saying that $\mathbf{k}'$ lies within the Wigner-Seitz cell (Sec. 2.2.1) of the reciprocal lattice. The Wigner-Seitz cell of the reciprocal lattice is called the *first Brillouin zone.* It is evident that one can reduce any wave vector $\mathbf{k}$ in the reciprocal space to a point in the first Brillouin zone (Fig. 2.2), so any eigenwave can be given a label in the *reduced zone scheme* and can be characterized by its *reduced wave vector.*

### 2.2.7 Symmetries of the crystal lattice

A photonic crystal might have symmetries other than discrete translations. The full set of rotation, mirror-reflection or inversion transformations, which leaves the crystal

invariant, is called the *point group* of the crystal. The band structure of the crystal are also invariant with respect to the point group transformations and has additional redundancies of the crystal eigenwaves within the Brillouin zone.

This property is illustrated here on the example of the rotational symmetry. Suppose the operator $\mathcal{R}$ is a rotation operator. To rotate a vector field $\mathbf{H}_{n\mathbf{k}}(\mathbf{r})$, the vector $\mathbf{H}_{n\mathbf{k}}$ together with its argument $\mathbf{r}$ should be rotated

$$\mathbb{R}\mathbf{H}_{n\mathbf{k}}(\mathbf{r}) = \mathcal{R}\mathbf{H}_{n\mathbf{k}}\left(\mathcal{R}^{-1}\mathbf{r}\right), \tag{2.67}$$

where the vector field rotation operator $\mathbb{R}$ was introduced. If the rotation by $\mathcal{R}$ leaves the system invariant, then the operator $\mathbb{R}$ should commute with the differential operator $\mathcal{L}_H$ (2.18), that leads to

$$\mathcal{L}_H\left(\mathbb{R}\mathbf{H}_{n\mathbf{k}}(\mathbf{r})\right) = \mathbb{R}\left(\mathcal{L}_H\mathbf{H}_{n\mathbf{k}}(\mathbf{r})\right) = \left(\frac{\omega_{\mathbf{k}}}{c}\right)^2\left(\mathbb{R}\mathbf{H}_{n\mathbf{k}}(\mathbf{r})\right). \tag{2.68}$$

Relation (2.68) means, that the rotated field $\mathbb{R}\mathbf{H}_{n\mathbf{k}}(\mathbf{r})$ is itself an eigenwave of the wave equation (2.8,2.18) with the same eigenfrequency as an original eigenwave $\mathbf{H}_{n\mathbf{k}}(\mathbf{r})$. Further, it can be shown that the eigenwave $\mathbb{R}\mathbf{H}_{n\mathbf{k}}(\mathbf{r})$ is simply an eigenwave with the wave vector $\mathcal{R}\mathbf{k}$. To prove this statement, one should show that $\mathbb{R}\mathbf{H}_{n\mathbf{k}}(\mathbf{r})$ is an eigenfunction of the translation operator $T_{\mathbf{R}}$ with eigenvalue $\exp(i\mathcal{R}\mathbf{k}\mathbf{R})$, where $\mathbf{R}$ is a lattice vector. Taking into account that operators $T_{\mathbf{R}}$ and $\mathbb{R}$ commute, one has

$$\begin{aligned} T_{\mathbf{R}}\left(\mathbb{R}\mathbf{H}_{n\mathbf{k}}(\mathbf{r})\right) &= \mathbb{R}\left(T_{\mathcal{R}^{-1}\mathbf{R}}\mathbf{H}_{n\mathbf{k}}(\mathbf{r})\right) \\ &= \mathbb{R}\left(e^{i\left(\mathbf{k}\mathcal{R}^{-1}\mathbf{R}\right)}\mathbf{H}_{n\mathbf{k}}(\mathbf{r})\right) \\ &= e^{i(\mathcal{R}\mathbf{k}\mathbf{R})}\left(\mathbb{R}\mathbf{H}_{n\mathbf{k}}(\mathbf{r})\right), \end{aligned}$$

which proves that the eigenwave $\mathbb{R}\mathbf{H}_{n\mathbf{k}}(\mathbf{r})$ has the wave vector $\mathcal{R}\mathbf{k}$, so

$$\omega_n(\mathcal{R}\mathbf{k}) = \omega_n(\mathbf{k}). \tag{2.69}$$

Since the band structure $\omega = \omega_n(\mathbf{k})$ possesses the full symmetry of the point group, it is not necessary to consider it at every point in the first Brillouin zone. The smallest region within the first Brillouin zone for which the $\omega = \omega_n(\mathbf{k})$ are not related by symmetry of the crystal is called the *irreducible* Brillouin zone. For example, a photonic crystal with the symmetry of a simple square lattice has a square first Brillouin zone (Fig. 2.3). Then, the irreducible Brillouin zone is a triangular wedge with 1/8 the area of the full Brillouin zone (Fig. 2.3). The rest of the Brillouin zone contains redundant copies of the irreducible zone.

The mirror reflection symmetry in a photonic crystal deserves special attention.

Under certain conditions it allows to separate the wave equations (2.7,2.8) into two separate and independent equations, one for each field polarization [2]. In one case the magnetic field, $\mathbf{H}_{n\mathbf{k}}$, is perpendicular to the mirror plane and the electric field vector, $\mathbf{E}_{n\mathbf{k}}$, is parallel; while in the other case the magnetic field vector is in the plane and the electric field vector is perpendicular to the plane. This simplification provides immediate information about the eigenmode symmetries and facilitates the numerical calculation of their eigenfrequencies. The separation of the wave equations (2.7,2.8) by the field polarization is possible in the case of one- and two-dimensional periodic medium [2]. In the later case, the electromagnetic wave propagation should be restricted to the plane of periodicity.

### 2.2.8 Time reversal symmetry and scaling law

If the crystal has an inversion center, that is, if the periodic dielectric function is $\varepsilon(\mathbf{r}) = \varepsilon(-\mathbf{r})$, the band structure $\omega = \omega_n(\mathbf{k})$ also possesses the inversion symmetry $\omega_n(\mathbf{k}) = \omega_n(-\mathbf{k})$. Comparing the wave equation (2.65) with its complex conjugate

$$(\nabla - i\mathbf{k}) \times \left\{ \frac{1}{\varepsilon(\mathbf{r})} (\nabla - i\mathbf{k}) \times \mathbf{h}^*_{n\mathbf{k}}(\mathbf{r}) \right\} = \left( \frac{\omega_{\mathbf{k}}}{c} \right)^2 \mathbf{h}^*_{n\mathbf{k}}(\mathbf{r}) \tag{2.70}$$

and using the fact that eigenfrequencies are real (Sec. 2.1.3), one can see, that the Bloch wave $\mathbf{h}^*_{n\mathbf{k}}(\mathbf{r})$ satisfies the same wave equation as $\mathbf{h}_{n\mathbf{k}}(\mathbf{r})$ (2.65), with the very same eigenfrequency, but with the wave vector $-\mathbf{k}$. It follows that

$$\omega_n(\mathbf{k}) = \omega_n(-\mathbf{k}) \tag{2.71}$$

and that the band structure of the crystal has inversion symmetry even if the crystal itself does not. Taking the complex conjugate of $\mathbf{h}_{n\mathbf{k}}(\mathbf{r})$ is equivalent to reversing the sign of the time in the Maxwell's equations (2.1-2.4). So, the property (2.71) is a consequence of the *time-reversal* symmetry of the Maxwell's equations.

Another useful property of the photonic band structure is the scaling law. Suppose that for the crystal with a dielectric function $\varepsilon(\mathbf{r})$, an eigenwave $\mathbf{H}_{n\mathbf{k}}(\mathbf{r})$ has the eigenfrequency $\omega_{n\mathbf{k}}$. An eigenwave $\mathbf{H}_{n\mathbf{k}}(\mathbf{r})$ satisfies the wave equation (2.8,2.18)

$$\nabla \times \left\{ \frac{1}{\varepsilon(\mathbf{r})} \nabla \times \mathbf{H}_{n\mathbf{k}}(\mathbf{r}) \right\} = \frac{\omega^2_{n\mathbf{k}}}{c^2} \mathbf{H}_{n\mathbf{k}}(\mathbf{r}). \tag{2.72}$$

Now, performing the scale transformation $\mathbf{r}' = \mathbf{r}/s$, which is just a compression or

expansion of the original crystal, a change of variables can be done in (2.72) leading to

$$s\nabla' \times \left\{ \frac{1}{\varepsilon(\mathbf{r}'/s)} \nabla' \times \mathbf{H}_{n\mathbf{k}}\left(\mathbf{r}'/s\right) \right\} = \frac{\omega_{n\mathbf{k}}^2}{c^2} \mathbf{H}_{n\mathbf{k}}\left(\mathbf{r}'/s\right), \tag{2.73}$$

where a new dielectric function is $\varepsilon'\left(\mathbf{r}\right) = \varepsilon(\mathbf{r}'/s)$, $\mathbf{r}' = \mathbf{r}s$ and $\nabla' = \nabla/s$. Recognizing that $\varepsilon(\mathbf{r}'/s) = \varepsilon'\left(\mathbf{r}'\right)$ and dividing equation (2.73) by $s$, one have an eigenvalue problem for the field $\mathbf{H}'_{n\mathbf{k}}\left(\mathbf{r}'\right) = \mathbf{H}_{n\mathbf{k}}\left(\mathbf{r}'/s\right)$

$$\nabla' \times \left\{ \frac{1}{\varepsilon'(\mathbf{r}')} \nabla' \times \mathbf{H}_{n\mathbf{k}}\left(\mathbf{r}'/s\right) \right\} = \left(\frac{\omega_{n\mathbf{k}}}{sc}\right)^2 \mathbf{H}_{n\mathbf{k}}\left(\mathbf{r}'/s\right), \tag{2.74}$$

which gives a new eigenfrequency $\omega'_{n\mathbf{k}} = \omega_{n\mathbf{k}}/s$. That is, the mode profile and its eigenfrequency after changing the length scale by factor $s$ are simply the mode profile and the frequency of the original crystal scaled by the same factor $s$. This simple fact is of considerable practical importance. Assuming that a dielectric function is the same at any length scale, *all modeling and design can be done for a single length scale, e.g., for optical or microwave regime, with a guarantee that the obtained results will be valid at any other length scales.*

# Bibliography


[1] P. Yeh, *Optical Waves in Layered Media* (John Wiley and Sons, New York, 1988).

[2] J. D. Joannopoulos, R. D. Meade, and J. N. Winn, *Photonic crystals: molding the flow of light* (Princeton University Press, Princeton NJ, 1995).

[3] K. Sakoda, *Optical Properties of Photonic Crystals* (Springer, Berlin, 2001).

[4] J. M. Ziman, *Principles of the Theory of Solids* (Cambridge University Press, Cambridge, 1972).

[5] N. W. Ashcroft and N. D. Mermin, *Solid State Physics* (Saunder College, Philadelphia, 1976).

[6] C. Kittel, *Solid State Physics* (John Wiley and Sons, New York, 1986).

[7] J. D. Jackson, *Classical Electrodynamics* (John Wiley, New York, 1975).

[8] R. J. Glauber and M. Lewenstein, "Quantum optics of dielectric media," *Phys. Rev. A* **43,** 467–491 (1991).

[9] J. P. Dowling and C. M. Bowden, "Atomic emission rates in inhomogeneous media with applications to photonic band structures," *Phys. Rev. A* **46,** 612–622 (1992).

[10] K. Sakoda and K. Ohtaka, "Optical response of three-dimensional photonic lattices: Solutions of inhomogeneous Maxwell's equations and their applications," *Phys. Rev. B* **54,** 5732–5741 (1996).

[11] D. Park, *Introduction to the Quantum Theory* (McGraw-Hill, New York, 1964).

[12] E. Yablonovitch, "Inhibited spontaneous emission in solid-state physics and electronics," *Phys. Rev. Lett.* **58,** 2059–2062 (1987).

[13] S. John, "Strong localization of photons in certain disordered dielectric superlattices," *Phys. Rev. Lett.* **58,** 2486–2489 (1987).

# Chapter 3

# Reflection, refraction and emission in photonic crystals

The existence of the continuous photonic bands (allowed bands) separated by forbidden gaps in the dispersion relations of a periodic medium leads to a number of unusual properties of photonic crystals. In this chapter *a total reflection*, *an anomalous refraction* and *a modified emission* are illustrated using examples of one-, two- and three-dimensional photonic crystals respectively. In section 3.1, a one-dimensional photonic crystal is introduced and analyzed using a band structure formalism. A one-dimensional photonic crystal slab acts as a high reflector at the forbidden gap frequencies. In section 3.2, using an example of a two-dimensional photonic crystal it is demonstrated, how the allowed bands anisotropy leads to the anomalous refraction. The concept of iso-frequency surfaces is introduced. In section 3.3, the radiated power of oscillating dipole placed in a three-dimensional photonic crystal is introduced and analyzed. It is shown that both suppression and enhancement of radiated power over some frequency regions are possible. In this chapter two numerical methods, namely, the transfer matrix and the plane wave expansion methods, are introduced and discussed. Both methods have been routinely used in the work reported in this thesis.

## 3.1 Bragg mirror as a one-dimensional photonic crystal

The subject of this section is the simplest type of photonic crystals, i.e., media which are periodic in one spatial direction (Fig. 3.1). Such structures are widely used in modern optoelectronics, ranging from Bragg mirrors for distributed-feedback lasers

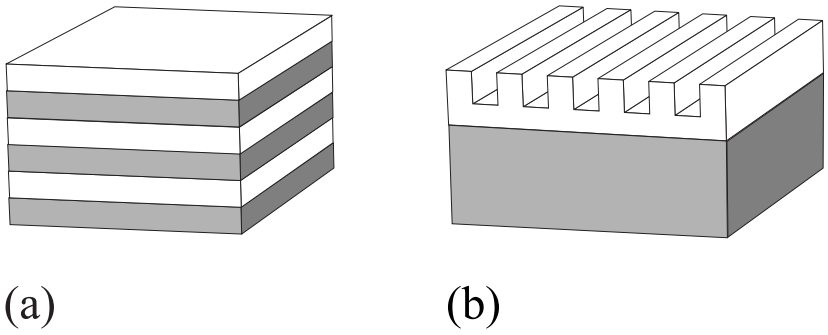


Figure 3.1: Two examples of one-dimensional photonic crystals, (a) a thin-film multilayer structure and (b) a planar corrugated waveguide.

to narrow-band filters for dense wavelength division multiplexing (WDM) systems (see e.g. [1, 2, 3]). Thin-film growth, especially molecular-beam epitaxy, make it possible to grow almost any thin-film structure with well-controlled periodicity and layer thickness [1, 2].

A typical example of a one-dimensional periodic medium is a Bragg mirror [Fig. 3.1(a)], which is a multilayer made of alternating transparent layers with different refractive indices. Assuming a laser beam is incident on a Bragg mirror, the light will be reflected and refracted at each interface (Fig. 3.2). Constructive interference in reflection occurs when the condition

$$m\lambda = 2\Lambda \cos \alpha_{inc} \tag{3.1}$$

is satisfied [4]. Here, $\lambda$ is the wavelength of the incident light, $\Lambda$ is a period of the periodic medium, $m$ is an integer number and $\alpha_{inc}$ is an angle of incidence. This relation is known as the *Bragg condition*. It can be easily derived by considering the phase difference between rays reflected from successive layers. Constructive interference occurs when the optical path difference between rays reflected from successive lattice planes contains an integer number of wavelengths. Thus, reflection spectrum of a Bragg mirror consists of alternating regions of strong and weak reflection, with a strong reflection corresponding to the Bragg condition (3.1).

### 3.1.1 Light propagation in periodic layered media: transfer matrix method

The simplest periodic medium is one made up of alternating layers of transparent dielectric materials with different refractive indices, $n_1$ and $n_2$. Here it is assumed, that alternating layers have thicknesses, $d_1$ and $d_2$. Further, subscripts 1 and 2 are used for low and high index layers, respectively. Formally, then such a structure is

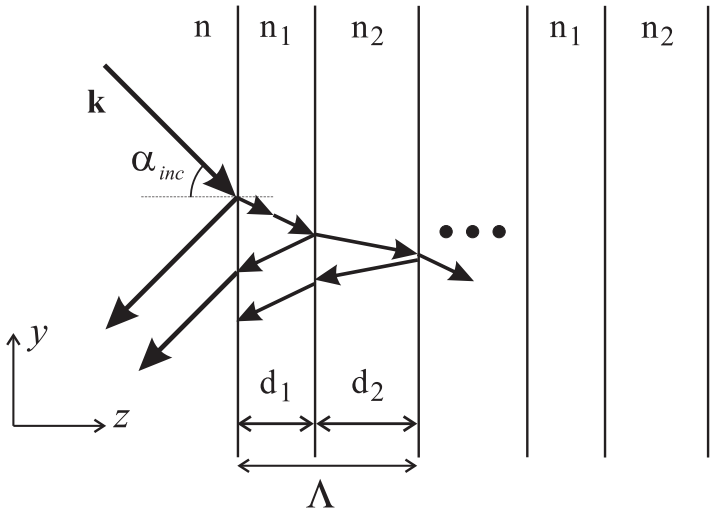


Figure 3.2: Schematic representation of a one-dimensional periodic medium. The coordinate system and light rays refracting and propagating through a stack are shown. The angle of incidence is designated by $\alpha_{inc}$. Refractive indices of alternating regions and an ambient medium are $n_1$, $n_2$ ($n_1 < n_2$) and $n$, respectively. Thicknesses of alternating regions are $d_1$ and $d_2$. $\Lambda = d_1 + d_2$ is a period.

described by the periodic refractive index

$$n(z) = \begin{cases} n_1, & 0 < z < d_1 \\ n_2, & d_1 < z < \Lambda \end{cases} \tag{3.2}$$

with

$$n\left(z\right) = n\left(z + \Lambda\right), \tag{3.3}$$

where the $z$ axis is normal to the layer interfaces and $\Lambda = d_1 + d_2$ is the period. The geometry of the structure is sketched in figure 3.2.

To solve for the electromagnetic field in such a structure, the approach described in [5] is followed. The general solution of the wave equation for the multilayered structure can be written in the form

$$\mathbf{E}\left(\mathbf{r}\right) = \mathbf{E}\left(z\right) e^{i(-k_y y + \omega t)}, \tag{3.4}$$

where it is assumed that the plane of propagation is the $yz$ plane (Fig. 3.2), $k_y$ is the $y$ component of the wave vector $\mathbf{k}$, which remains constant throughout the medium. The electric field within each homogeneous layer can be expressed as a superposition of an incident and a reflected plane wave. The complex amplitudes of these two waves can be represented as the components of a column vector. The electric field in layer $\alpha$

($\alpha = 1,\, 2$) of the $n$-th unit cell can thus be represented by a column vector

$$\begin{pmatrix} a_n^{(\alpha)} \\ b_n^{(\alpha)} \end{pmatrix}, \quad \alpha = 1,\, 2. \tag{3.5}$$

As a result, the electric field distribution in the same layer can be written

$$E\left(y,z\right) = \left[a_n^{(\alpha)} e^{-ik_{\alpha n}(z-n\Lambda)} + b_n^{(\alpha)} e^{ik_{\alpha n}(z-n\Lambda)}\right] e^{-ik_y y} \tag{3.6}$$

with

$$k_{\alpha z} = \left[\left(\tfrac{n_\alpha \omega}{c}\right)^2 - k_y^2\right]^{1/2}, \quad \alpha = 1,\, 2. \tag{3.7}$$

Here $k_{\alpha z}$ is the $z$ component of the wave vector $\mathbf{k}$ in the $\alpha$'s layer, $c$ is speed of light in vacuum.

The column vectors (3.5) are not independent of each other. They are related through the continuity conditions at the interface. As a consequence, only one vector can be chosen arbitrary. Due to the planar geometry of the problem, the separation of the electromagnetic field into TE (transverse electric) and TM (transverse magnetic) polarization states is possible (chapter 2). Then, in the case of TE waves (the electric field $\mathbf{E}$ perpendicular to the plane of propagation $yz$), imposing the continuity of $E_x$ and $H_y$ at the interfaces $z = (n-1)\,\Lambda$ and $z = (n-1)\,\Lambda + d_2$, leads to the following two matrix equations:

$$\begin{pmatrix} 1 & 1 \\ 1 & -1 \end{pmatrix} \begin{pmatrix} a_{n-1} \\ b_{n-1} \end{pmatrix} = \begin{pmatrix} e^{ik_{2z}\Lambda} & e^{-ik_{2z}\Lambda} \\ \frac{k_{2z}}{k_{1z}} e^{ik_{2z}\Lambda} & -\frac{k_{2z}}{k_{1z}} e^{-ik_{2z}\Lambda} \end{pmatrix} \begin{pmatrix} c_n \\ d_n \end{pmatrix} \tag{3.8}$$

$$\begin{pmatrix} e^{ik_{2z}\Lambda} & e^{-ik_{2z}\Lambda} \\ e^{ik_{2z}\Lambda} & -e^{-ik_{2z}\Lambda} \end{pmatrix} \begin{pmatrix} c_n \\ d_n \end{pmatrix} = \begin{pmatrix} e^{ik_{1z}\Lambda} & e^{-ik_{1z}\Lambda} \\ \frac{k_{1z}}{k_{2z}} e^{ik_{1z}\Lambda} & -\frac{k_{1z}}{k_{2z}} e^{-ik_{1z}\Lambda} \end{pmatrix} \begin{pmatrix} a_n \\ b_n \end{pmatrix} \tag{3.9}$$

where $a_n \equiv a_n^{(1)}$, $b_n \equiv b_n^{(1)}$, $c_n \equiv a_n^{(2)}$ and $d_n \equiv b_n^{(2)}$. By eliminating column vector

$$\begin{pmatrix} c_n \\ d_n \end{pmatrix}$$

in (3.8-3.9), one can obtain the following matrix equation,

$$\begin{pmatrix} a_{n-1} \\ b_{n-1} \end{pmatrix} = \begin{pmatrix} A_p & B_p \\ C_p & D_p \end{pmatrix} \begin{pmatrix} a_n \\ b_n \end{pmatrix}, \tag{3.10}$$

which relates the complex amplitudes of the plane waves in layer 1 of the unit cell to those of the equivalent layer in the next unit cell. Here index $p$ can be chosen as $TE$

or $TM$ for TE and TM waves, respectively. The matrix

$$\begin{pmatrix} A_p & B_p \\ C_p & D_p \end{pmatrix} \tag{3.11}$$

is called *a unit-cell translation matrix*. Because unit-cell translation matrix in (3.10) relates the field amplitudes in two equivalent layers with the same index of refraction, it is unimodular

$$A_p D_p - B_p C_p = 1. \tag{3.12}$$

In the case of TE waves, the form of the matrix elements in (3.10) follows from (3.8-3.9) and is given by

$$A_{TE} = e^{ik_{1z}d_1}\left[\cos k_{2z}d_2 + \frac{1}{2}i\left(\frac{k_{2z}}{k_{1z}} + \frac{k_{1z}}{k_{2z}}\right)\sin k_{2z}d_2\right] \tag{3.13}$$

$$B_{TE} = e^{-ik_{1z}d_1}\left[\frac{1}{2}i\left(\frac{k_{2z}}{k_{1z}} - \frac{k_{1z}}{k_{2z}}\right)\sin k_{2z}d_2\right] \tag{3.14}$$

$$C_{TE} = e^{ik_{1z}d_1}\left[-\frac{1}{2}i\left(\frac{k_{2z}}{k_{1z}} - \frac{k_{1z}}{k_{2z}}\right)\sin k_{2z}d_2\right] \tag{3.15}$$

$$D_{TE} = e^{-ik_{1z}d_1}\left[\cos k_{2z}d_2 - \frac{1}{2}i\left(\frac{k_{2z}}{k_{1z}} + \frac{k_{1z}}{k_{2z}}\right)\sin k_{2z}d_2\right] \tag{3.16}$$

In the case of TM waves, for which the magnetic field $\mathbf{H}$ is perpendicular to the propagation plane $yz$, the complex amplitudes of the plane wave in two successive unit cells are also related via the matrix equation (3.10), but with slightly different matrix elements

$$A_{TM} = e^{ik_{1z}d_1}\left[\cos k_{2z}d_2 + \frac{1}{2}i\left(\frac{n_2^2 k_{1z}}{n_1^2 k_{2z}} + \frac{n_1^2 k_{2z}}{n_2^2 k_{1z}}\right)\sin k_{2z}d_2\right] \tag{3.17}$$

$$B_{TM} = e^{-ik_{1z}d_1}\left[\frac{1}{2}i\left(\frac{n_2^2 k_{1z}}{n_1^2 k_{2z}} - \frac{n_1^2 k_{2z}}{n_2^2 k_{1z}}\right)\sin k_{2z}d_2\right] \tag{3.18}$$

$$C_{TM} = e^{ik_{1z}d_1}\left[-\frac{1}{2}i\left(\frac{n_2^2 k_{1z}}{n_1^2 k_{2z}} - \frac{n_1^2 k_{2z}}{n_2^2 k_{1z}}\right)\sin k_{2z}d_2\right] \tag{3.19}$$

$$D_{TM} = e^{-ik_{1z}d_1}\left[\cos k_{2z}d_2 - \frac{1}{2}i\left(\frac{n_2^2 k_{1z}}{n_1^2 k_{2z}} + \frac{n_1^2 k_{2z}}{n_2^2 k_{1z}}\right)\sin k_{2z}d_2\right] \tag{3.20}$$

It is important to note that a unit-cell translation matrix which relates the field amplitudes in layer 2 of the unit cell is different from the matrices (3.13-3.16) and (3.17-3.20). However, these matrices possess the same trace. It will be shown later, that the trace of a unit-cell translation matrix, $A_p + D_p$, is directly related to the band structure of the periodic medium.

As it was noted above, only one column vector (3.5) is independent. One can

choose it, for example, as the column vector of the layer 1 in the zeroth unit cell. The remaining column vector of the equivalent layers are related to that of the zeroth unit cell by

$$\begin{pmatrix} a_0 \\ b_0 \end{pmatrix} = \begin{pmatrix} A_p & B_p \\ C_p & D_p \end{pmatrix}^n \begin{pmatrix} a_n \\ b_n \end{pmatrix}, \tag{3.21}$$

which can be inverted to yield

$$\begin{pmatrix} a_n \\ b_n \end{pmatrix} = \begin{pmatrix} A_p & B_p \\ C_p & D_p \end{pmatrix}^{-n} \begin{pmatrix} a_0 \\ b_0 \end{pmatrix}. \tag{3.22}$$

By using the identity

$$\begin{pmatrix} A_p & B_p \\ C_p & D_p \end{pmatrix}^{-1} = \begin{pmatrix} D_p & -B_p \\ -C_p & A_p \end{pmatrix}$$

for unimodular matrices (3.12) one can write

$$\begin{pmatrix} a_n \\ b_n \end{pmatrix} = \begin{pmatrix} D_p & -B_p \\ -C_p & A_p \end{pmatrix}^n \begin{pmatrix} a_0 \\ b_0 \end{pmatrix}. \tag{3.23}$$

The matrix in equation (3.23) is a translation matrix, or *transfer matrix*, of the $n$-periods multilayer structure, relating the complex amplitudes of the plane waves in layer 1 of the zeroth unit cell to those of the equivalent layer in the last unit cell of the medium.

### 3.1.2 Photonic band structure

A periodic layered medium is equivalent to a one-dimensional crystal which is invariant under lattice translations. If the translation operator is defined by $T_z z = z - l\Lambda$, where $l$ is an integer, the field in the periodic layered structure obeys the relation

$$T_z \mathbf{E}(z) = \mathbf{E}(z + l\Lambda). \tag{3.24}$$

Then, the transfer matrix in (3.10) is a representation of the unit-cell translation operator. According to the Bloch theorem (chapter 2), the electric field of the eigenwave in a periodic medium can be found in the form

$$\mathbf{E}(\mathbf{r}, t) = \mathbf{E}_K(z)\, e^{-iKz} e^{-ik_y y} e^{i\omega t}, \tag{3.25}$$

where $\mathbf{E}_K(z)$ is a periodic function with period $\Lambda$ and the wave vector $\mathbf{k}$ is separated in the $y$ component $k_y$, which remains constant throughout the medium, and in the $z$

component $K$, which remains to be determined. The subscript $K$ indicates that the function $\mathbf{E}_K(z)$ depends on $K$. The $z$ component of the wave vector is known as *the Bloch wave numbe*r.

Equations (3.24) and (3.25) together with the transfer matrix (3.10) specify the dispersion relations for the periodic layered medium. The problem at hand is thus to determine the Bloch wave number $K$ and the Bloch eigenwave $\mathbf{E}_K(z)$ as a function of frequency $\omega$ and the tangential component of the wave vector $k_y$.

In terms of the column vector representation, the periodic condition on the field, $\mathbf{E}_K(z) = \mathbf{E}_K(z+\Lambda)$, is simply given by

$$\begin{pmatrix} a_n \\ b_n \end{pmatrix} = e^{-iK\Lambda} \begin{pmatrix} a_{n-1} \\ b_{n-1} \end{pmatrix}. \tag{3.26}$$

Then, taking into account the matrix equation (3.10) and periodicity condition (3.26), one can find, that the column vector of the Bloch eigenwave satisfies the following eigenvalue equation

$$\begin{pmatrix} A_p & B_p \\ C_p & D_p \end{pmatrix} \begin{pmatrix} a_n \\ b_n \end{pmatrix} = e^{iK\Lambda} \begin{pmatrix} a_n \\ b_n \end{pmatrix}. \tag{3.27}$$

The phase factor $\exp(iK\Lambda)$ is thus the eigenvalue of the transfer matrix (3.11) and satisfies the secular equation

$$\begin{vmatrix} A_p - e^{iK\Lambda} & B_p \\ C_p & D_p - e^{iK\Lambda} \end{vmatrix} = 0,$$

the solutions of which are

$$e^{iK\Lambda} = \frac{1}{2}(A_p + D_p) \pm \left\{ \left[ \frac{1}{2}(A_p + D_p) \right]^2 - 1 \right\}^{1/2}. \tag{3.28}$$

The eigenvectors corresponding to the eigenvalues (3.28) are obtained from (3.27) and are equal to

$$\begin{pmatrix} a_0 \\ b_0 \end{pmatrix} = \begin{pmatrix} B_p \\ e^{iK\Lambda} - A_p \end{pmatrix}. \tag{3.29}$$

For the $n$-th unit cell the corresponding column vectors are given according to (3.26), by

$$\begin{pmatrix} a_n \\ b_n \end{pmatrix} = e^{-inK\Lambda} \begin{pmatrix} B_p \\ e^{iK\Lambda} - A_p \end{pmatrix}.$$

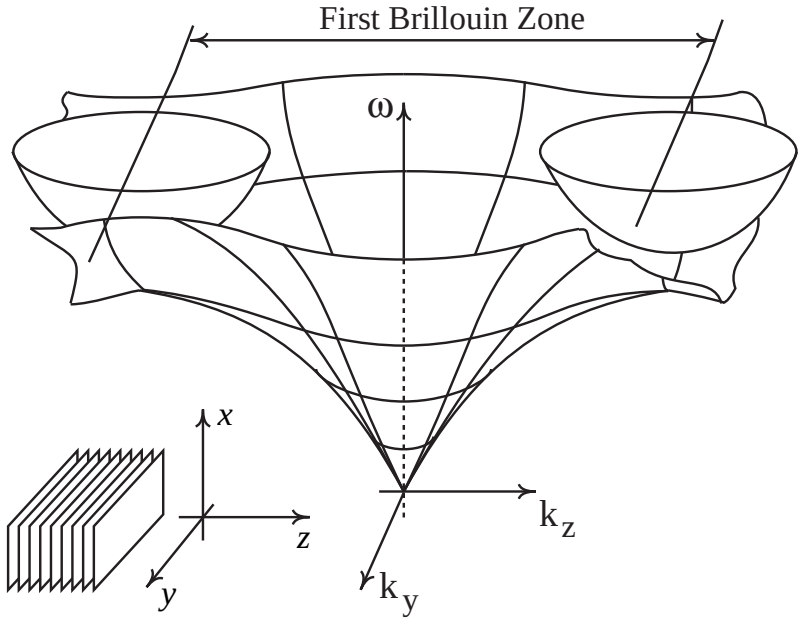


Figure 3.3: The sketch of the photonic band structures of a periodic layered medium. The inset shows the orientation of the medium. Only two-dimensional slices of the wave vector space are presented. The band structure is presented for one polarization.

Then finally, the Bloch eigenwave in layer 1 of the $n$-th unit cell is given by

$$E_K(z)\, e^{iKz} = \left[\left(a_0 e^{-ik_{1z}(z-n\Lambda)} + b_0 e^{ik_{1z}(z-n\Lambda)}\right) e^{iK(z-n\Lambda)}\right] e^{-iKz}, \tag{3.30}$$

where amplitudes $a_0$ and $b_0$ are given by (3.29). It is important to note, that the function inside the square brackets is independent of the unit cell number $n$ and therefore is periodic with period $\Lambda$, in agreement with the Bloch theorem (3.25).

The Bloch eigenwaves (3.30) can be considered as the eigenvectors of the transfer matrix (3.11) with the eigenvalue $\exp(iKz)$ given by (3.28). The two eigenvalue in (3.28) are reciprocals to each other, since the transfer matrix is unimodular (3.12). Equation (3.28) gives the dispersion relation between frequency $\omega$, tangential component of the wave vector $k_y$, and the Bloch wave number $K$. The dispersion relation defines *the photonic band structure* of the periodic layered medium, a one-dimensional photonic crystal, and it has the form

$$K(\omega, k_y) = \frac{1}{\Lambda} \cos^{-1}\left[\frac{1}{2}(A_p + D_p)\right]. \tag{3.31}$$

Regimes where $\left|\frac{1}{2}(A_p + D_p)\right| < 1$, corresponds to real Bloch wave numbers $K$ and thus to propagating Bloch waves. However, when $\left|\frac{1}{2}(A_p + D_p)\right| > 1$ , the Bloch wave number is a complex number, $K = m\pi/\Lambda + i\mathrm{Im}K$, and so the Bloch wave is evanescent.

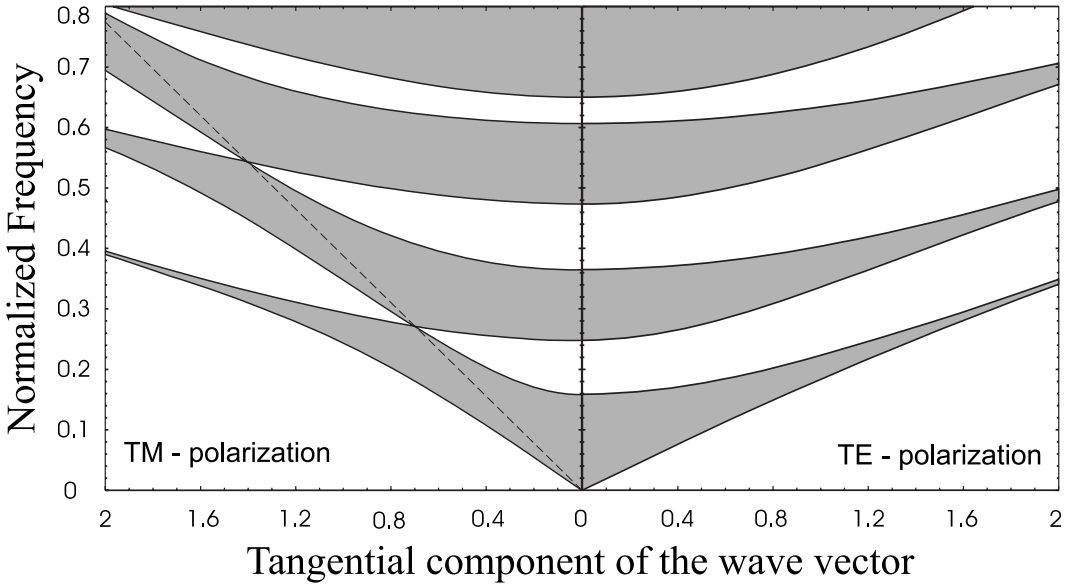


Figure 3.4: Projected band structure of a typical one-dimensional photonic crystal for TE (right panel) and TM (left panel) polarizations. The frequency, $\omega$, and the tangential component of the wave vector, $k_y$, are normalized as $\omega\Lambda/2\pi c$ and $k_y\Lambda/\pi$, respectively. The shaded areas correspond to allowed bands. The dashed line corresponds to the Brewster angle.

These regions are called *forbidden bands*, or *photonic bandgaps*, of the periodic medium. The band edges, defining bandgaps, are given by $\left|\frac{1}{2}\left(A_p + D_p\right)\right| = 1$.

The dispersion relation (3.31) gives the component of the Bloch wave vector along the $z$ direction, $K = k_z$, for the Bloch wave with frequency $\omega$ and the tangential component of the wave vector $k_y$. It can be represented by a surface in a three-dimensional space ($k_z$, $k_y$, $\omega$). An example of such a three-dimensional band structure is presented in figure 3.3. The intersection of this surface with the planes $k_z = m\pi/\Lambda$ are curves which represents band edges. The projection of these curves on the $k_y\omega$ plane gives *projected band structure*.

An example of the projected band structure is given in figure 3.4. The refractive indices of a periodic layered medium are chosen close to ones of $SiO_2$ and Si in the near IR region and are $n_1 = 1.4$ and $n_2 = 3.4$, respectively. Thicknesses of the layers are equal, $d_1 = d_2$. The right panel is for TE waves, and the left one for TM waves. Shaded zones are the allowed bands, where the Bloch wave number $K = k_z$ is a real number. It is interesting to note that the TM bandgaps shrink to zero, when $k_y = (\omega/c)\, n_2 \sin\alpha_B$ with $\alpha_B$ equal to the Brewster angle, since at this angle the reflection at the interfaces between layers vanishes and the incident and reflected waves are uncoupled.

In figure 3.5 the band structure of the $SiO_2$/Si periodic layered medium (Fig. 3.4) is shown for the special case $k_y = 0$, which corresponds to the normal incidence. The

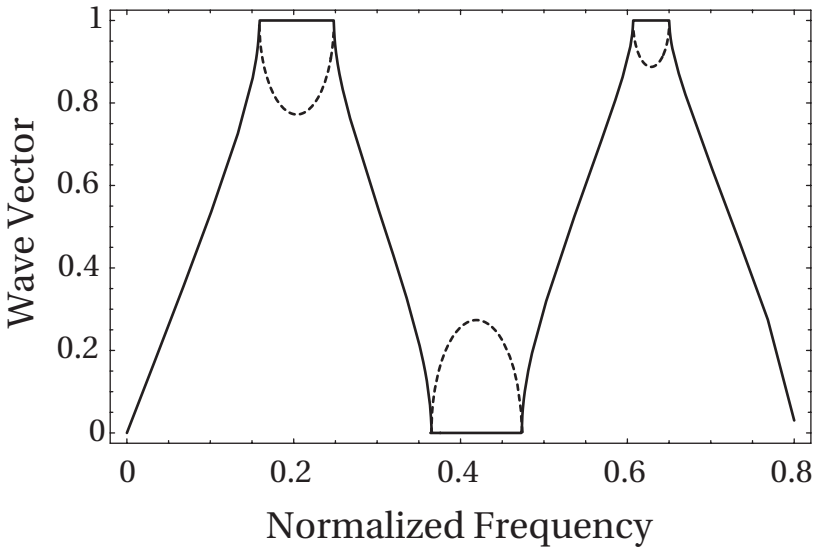


Figure 3.5: Photonic band structure of a typical one-dimensional photonic crystal for $k_y = 0$ (normal incidence). The frequency is normalized as $\omega\Lambda/2\pi c$. The Bloch wave number $K$ is normalized as $K\Lambda/\pi$. The dashed curves give the imaginary part of the Bloch wave number $K$ in arbitrary units.

band structure represents the dependence of the Bloch wave number as a function of the frequency $\omega$. The photonic bands (allowed bands) separated by clearly defined photonic bandgaps (forbidden bands) are shown. The imaginary part of the Bloch wave number is shown as dashed curves. Its value vanishes within allowed bands and is non-zero within forbidden bands.

### 3.1.3 Bragg reflection

Consider a periodic layered medium with $N$ unit cells placed in a dielectric medium with refractive index $n = n_1$ (Fig. 3.2). Assuming an incident field coming from the left, the reflection coefficient is given by

$$r_N = \frac{a_0}{b_0}, \tag{3.32}$$

where $a_0$ and $b_0$ are complex amplitudes of incident and reflected field, correspondingly. Here, it is assumed that there is no wave incident on the periodic medium from the right (i.e., $b_n = 0$). From (3.21) one has

$$\begin{pmatrix} a_0 \\ b_0 \end{pmatrix} = \begin{pmatrix} A_p & B_p \\ C_p & D_p \end{pmatrix}^N \begin{pmatrix} a_n \\ b_n \end{pmatrix}, \tag{3.33}$$

where the $N$-th power of the unimodular matrix (3.8) can be simplified by the following matrix identity

$$\begin{pmatrix} A_p & B_p \\ C_p & D_p \end{pmatrix}^N = \begin{pmatrix} A_p U_{N-1} - U_{N-2} & B_p U_{N-1} \\ C_p U_{N-1} & D_p U_{N-1} - U_{N-2} \end{pmatrix} \tag{3.34}$$

with

$$U_N = \frac{\sin(N+1)K\Lambda}{\sin K\Lambda} \tag{3.35}$$

and the Bloch wave number $K$ given by equation (3.31). The complex reflection coefficient is obtained from equations (3.32-3.35) as

$$r_N = \frac{C_p U_{N-1}}{A_p U_{N-1} - U_{N-2}} \tag{3.36}$$

and the reflectivity of the periodic medium is obtained from (3.36) by taking the square of the complex reflection coefficient $r_N$:

$$|r_N|^2 = \frac{|C_p|^2}{|C_p|^2 + \left(\frac{\sin K\Lambda}{\sin NK\Lambda}\right)^2}. \tag{3.37}$$

The term $|C_p|^2$ in (3.37) is roughly equal to the reflectivity of a single unit cell. This follows from the equation (3.37) with $N = 1$ and by taking into account that the reflectivity of the unit cell is usually much less than unity. For a large number of periods $N$, the second term in the denominator of relation (3.37) is a fast-varying function of the Bloch wave number $K$, or equivalently, of the tangential component of the wave vector $k_y$ and frequency $\omega$. This term dominates the structure of the reflectivity spectrum of the layered periodic medium.

Within allowed bands, the reflectivity oscillates with frequency having exactly $N-1$ nodes where the reflectivity vanishes. For frequencies within a forbidden band, the Bloch wave number (3.31) is complex

$$K = m\pi/\Lambda + i\mathrm{Im}K$$

and reflectivity formula (3.37) becomes

$$|r_N|^2 = \frac{|C_p|^2}{|C_p|^2 + \left(\frac{\sinh \mathrm{Im}(K)\Lambda}{\sinh N\mathrm{Im}(K)\Lambda}\right)^2}. \tag{3.38}$$

For large $N$, the second term in the denominator of relation (3.38) approaches zero exponentially as $\exp[-2(N-1)\,\mathrm{Im}(K)\,\Lambda]$. So, the reflectivity of a Bragg mirror (one-

dimensional photonic crystal) is near unity for the medium with a substantial number of periods and a Bragg mirror acts as a high reflector within the frequency range of a forbidden band of the periodic medium.

The reflectivity of the typical Bragg reflector as a function of frequency and angle of incidence is presented in figure 3.6-top. The light is impinging on the 10-period Bragg mirror from the ambient medium with $n = n_1$. The indices of refraction are $n_1 = 1.4$ and $n_2 = 3.4$, and the layers thicknesses are equal, $d_1 = d_2$ (see Fig. 3.4). The total reflection is colored blue, while the vanishing reflection is colored red.

At the center of each forbidden band, the period of the layered medium is approximately equal to an integer multiple of the light wavelength. The light is highly reflected, since successive reflections from neighboring interfaces are in phase with one another and therefore are constructively superimposed. Regions of high reflection are shown in blue in figure 3.6-top. For comparison, the photonic band structure of an infinite periodic medium (Fig. 3.4) projected onto the $\omega\alpha_{inc}$ plane is presented in figure 3.6-bottom. Here $\alpha_{inc}$ is angle of incidence. The projected band structure (Fig. 3.4) is related to the projected band structure (Fig. 3.6-bottom) via $k_y = (\omega/c)\, n \sin\alpha_{inc}$, which relates the tangential component of the wave vector with the angle of incidence $\alpha_{inc}$. Regions of high reflection coincide with the forbidden bands of the periodic medium.

TE and TM polarized waves have different band structures and different reflectivities. In figure 3.6, the left panel is for TM waves and the right panel in for TE waves. For TM waves incident at the Brewster angle $\alpha_B$, there is no reflected wave (Fig. 3.6) regardless of the number of periods forming a Bragg mirror, since at this angle the reflection at the interfaces between layers vanishes and the incident and reflected waves are uncoupled.

Analytical expression (3.37) gives reflectivity of the periodic layered medium in the case when the light is incident from a medium with a refractive index $n_1$. Typically, a refractive index of an ambient medium, $n$, is different from refractive indices of the layers. In such a case, the reflection coefficient of the layered medium surrounded by two homogenous dielectric media with refractive indices $n$ and $n_l$ is given by [4]

$$r = \frac{(t_{11} + t_{12}p_l)\, p - (t_{21} + t_{22}p_l)}{(t_{11} + t_{12}p_l)\, p + (t_{21} + t_{22}p_l)}, \tag{3.39}$$

where $t_{ij}$ are elements of the transfer matrix of the layered medium (3.23), which can be calculated numerically using matrix elements of the unit-cell translation matrix (3.13-3.20). In equation (3.39), coefficients $p$ and $p_l$ are defined as $p = n\cos\alpha_{inc}$ and $p_l = n_l \cos\alpha_l$, where $\alpha_{inc}$ and $\alpha_l$ are angles between the $z$ axis and incident and transmitted waves, respectively. The reflectivity is given by the square of the reflection coefficient (3.39), $|r|^2$.

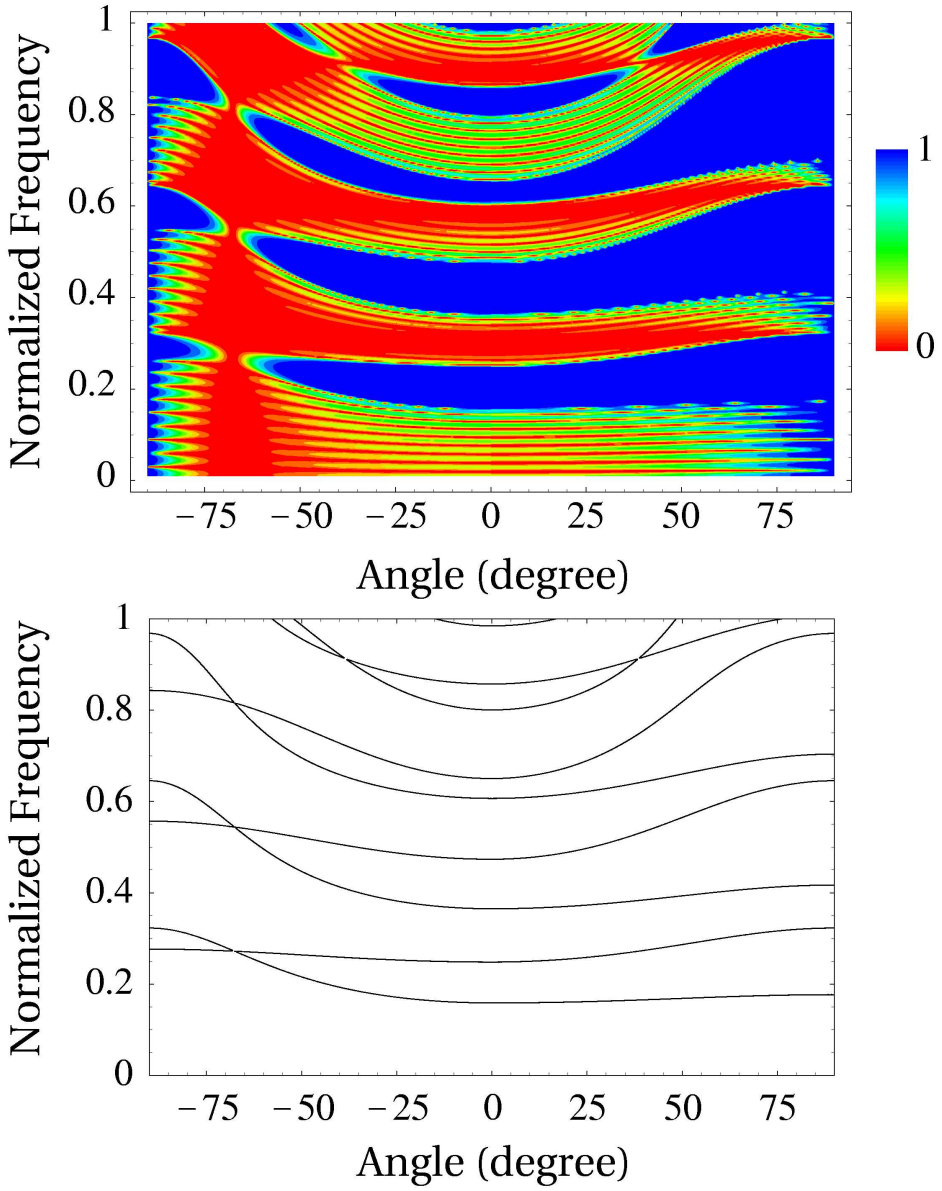


Figure 3.6: Top: a two-dimensional map of reflectivity spectrum of a 10-period Bragg reflector for TE (right) and TM (left) polarizations. Bottom: Photonic band structure of the corresponding infinite periodic medium projected onto the $\omega\alpha_{inc}$ plane. Here $\alpha_{inc}$ is angle of incidence, which is related to the tangential component of the wave vector via $k_y = (\omega/c)\, n \sin\alpha_{inc}$. The light impinges on the Bragg mirror from the ambient medium with $n = n_1$. The indices of refraction are $n_1 = 1.4$ and $n_2 = 3.4$, and the layers thicknesses are equal, $d_1 = d_2$ (see Fig. 3.4).

## 3.2 Form-anisotropy of photonic crystals

The dispersion relation between the eigenfrequency, $\omega_n(\mathbf{k})$, and the wave vector, $\mathbf{k}$, defines a *photonic band structure* of a periodic medium and describes properties of the Bloch eigenmodes. Dispersion relation can be formally written as

$$\omega = \omega_n(\mathbf{k}), \tag{3.40}$$

where $n$ is the band index. To build an intuitive understanding of the Bloch wave properties it is illustrative to introduce a geometrical representation of the dispersion relation (3.40). This can be done by defining an iso-frequency surface. *An iso-frequency surface* or *constant frequency surface* is a surface in $\mathbf{k}$-space constructed by solving equation (3.40)

$$\omega_n(\mathbf{k}) = \omega_0, \quad \omega_0 = constant \tag{3.41}$$

independently for each band $n$.

Iso-frequency surfaces of a periodic medium are strongly non-spherical (Fig. 3.3). This is a result of the anisotropy of a periodic medium. The anisotropy of periodic layered media is a well known phenomenon [4]. In the long-wavelength regime ($\lambda \gg \Lambda$) it is usually referred to as *a form birefringence*. In the limit of long wavelengths, iso-frequency surfaces of a one-dimensional photonic crystal are similar to the iso-frequency surface of a negative uniaxial crystal [4]. At shorter wavelengths (higher frequencies), the form of iso-frequency surfaces strongly deviates from a sphere (Fig. 3.3). In general, the anisotropy of a periodic medium cannot be described by simple uniaxial or biaxial crystals and this phenomenon is referred to as *a form-anisotropy*.

### 3.2.1 Dispersion relations: plane wave expansion method

Dispersion relation (3.40) for a general periodic medium can be solved only numerically. One of the most popular method to find eigenfrequencies and eigenmodes of two- and three-dimensional photonic crystals is a *plane wave expansion method*. As it was shown in chapter 2, by expressing a Bloch wave as a superposition of plane waves

$$\mathbf{H}_{\mathbf{k}n}(\mathbf{r}) = \sum_{\mathbf{G}} \mathbf{h}_{\mathbf{k}n}(\mathbf{G}) \exp(i(\mathbf{k}_n + \mathbf{G})\mathbf{r}), \tag{3.42}$$

where summation is over reciprocal lattice vectors and $\mathbf{h}_{\mathbf{k}n}(\mathbf{G})$ are Fourier coefficients, the wave equation

$$\nabla \times \left\{ \frac{1}{\varepsilon(\mathbf{r})} \nabla \times \mathbf{H}_{\mathbf{k}n}(\mathbf{r}) \right\} = \frac{\omega_{\mathbf{k}n}^2}{c^2} \mathbf{H}_{\mathbf{k}n}(\mathbf{r}) \tag{3.43}$$

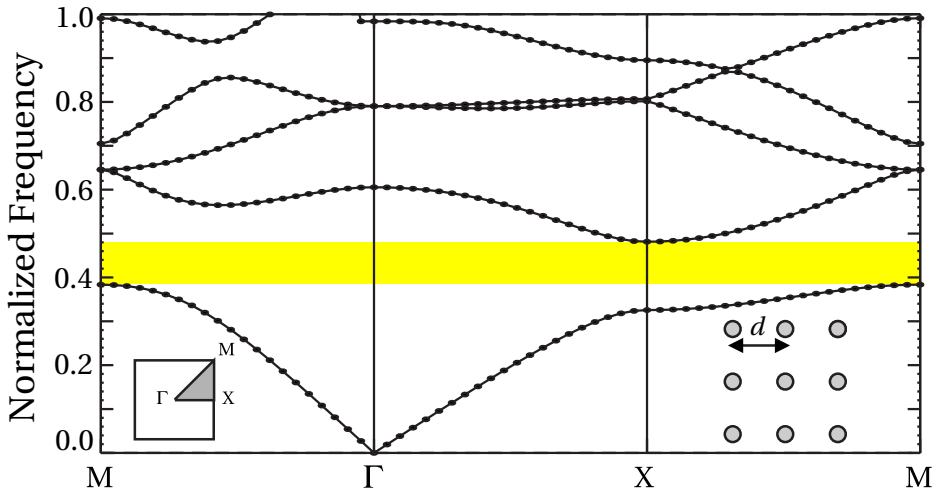


Figure 3.7: Photonic band structure of the square lattice photonic crystal made of dielectric rods in vacuum. Rods have the refractive index 2.9 and radius $r = 0.15d$, where $d$ is the lattice period. The band structure is given for TM polarization. The frequency is normalized to $\Omega = \omega d/2\pi c = d/\lambda$. $c$ is the speed of light in the vacuum. Insets show the first Brillouin zone (left) and a part of the lattice (right). Yellow region is a complete photonic bandgap in TM polarization.

can be transformed to an infinite linear system of homogenous equations for the unknown Fourier coefficients $\mathbf{h}_{\mathbf{k}n}(\mathbf{G})$

$$-\sum_{\mathbf{G}'} \widetilde{\varepsilon}(\mathbf{G}-\mathbf{G}')(\mathbf{k}_n+\mathbf{G}) \times \{(\mathbf{k}_n+\mathbf{G}') \times \mathbf{h}_{\mathbf{k}n}(\mathbf{G}')\} = \frac{\omega_{\mathbf{k}n}^2}{c^2}\mathbf{h}_{\mathbf{k}n}(\mathbf{G}). \tag{3.44}$$

Numerical solution of this linear system of equations gives unknown Fourier coefficients $\mathbf{h}_{\mathbf{k}n}(\mathbf{G})$ and eigenfrequencies, $\omega_{\mathbf{k}n}$, as a function of the wave vector, which allows to obtain a photonic band structure.

In the actual numerical calculations of the photonic bands, an infinite system of equation (3.44) is truncated to a sufficiently large number $N$ of reciprocal lattice vectors $\mathbf{G}$. Then, an eigenvalue problem for each wave vector $\mathbf{k}$ is solved, which is equivalent to the diagonalization of the matrix defined by the left-hand side of (3.44). In fact, the convergence of the plane wave expansion method is not good when the amplitude of the spatial variation of the dielectric function is large. Typically, one needs up to several thousands of plane waves in the expansion (3.42) to keep numerical error below 1%. Computer memory demands of the plane wave expansion methods scales as $N$ with the number of plane wave. The CPU time scales as $N \log N$. Discussions on the convergence of the plane wave expansion method can be found in [6, 7]. Recently, several modifications of the plane wave expansion method were proposed to improve its convergence [8, 9, 10].

In figure 3.7 the photonic band structure of a square lattice photonic crystal made of dielectric rods in vacuum calculated using the plane wave expansion method is depicted. Rods have the refractive index 2.9 and radius $r = 0.15d$, where $d$ is the lattice period. In the case of electromagnetic waves propagation in the plane of periodicity, one can separate Maxwell's equations by polarizations (chapter 2): TE and TM polarization, if the magnetic or electric field is parallel to the axis of the rods, respectively. In figure 3.7 the band structure is presented for TM polarization. One can see, a complete photonic bandgap in TM polarization between the first and the second allowed bands (yellow region). For the calculation of the band structure in figure 3.7 as well as for all plane wave calculations presented in this thesis, a freely available software realization of the plane wave expansion method was used [9].

### 3.2.2 Beam steering

A form-anisotropy of a photonic crystal leads to *the beam steering effect*. In essence, beam steering means, that *the energy velocity direction of the medium's eigenmode does not necessarily coincide with the direction of the eigenmode wave vector.* Here, energy velocity is defined as the velocity of propagation of the electromagnetic energy. This important concept can be illustrated using the Huygens principle [4], i.e., by constructing the wave front from an extended disturbance as a superposition of waves from point sources along the boundary of the disturbance.

An isotropic point source placed in a homogeneous isotropic medium generates a circular wave front [Fig. 3.8(a)]. If a line source generates a plane wave in an isotropic medium, its wave front is easily constructed, as shown in the right panel of figure 3.8(a). For propagation distances smaller than the length of the line source, the electromagnetic energy is radiated outward in the direction perpendicular to the wave front of the plane wave. The energy velocity is parallel to the wave vector.

An isotropic point source placed in an anisotropic medium, like an uniaxial crystal in figure 3.8(b), produces a non-spherical wave front due to the difference in the speed of light in different directions of the crystal. In the case of an uniaxial crystal the corresponding wave front will by an ellipse. A line source placed in an anisotropic medium at an arbitrary angle with respect to the crystal optical axes will generate a plane wave with the wave front shown at the right panel of figure 3.8(b). The energy flux travels along the highest velocity direction of the medium. The energy velocity is in general not parallel to the the wave vector.

In the homogeneous medium the energy velocity coincides with the group velocity, which is defined as the gradient of the dispersion relation (3.40) in $\mathbf{k}$-space

$$\mathbf{V}_g = \nabla_{\mathbf{k}} \omega \left( \mathbf{k} \right). \tag{3.45}$$

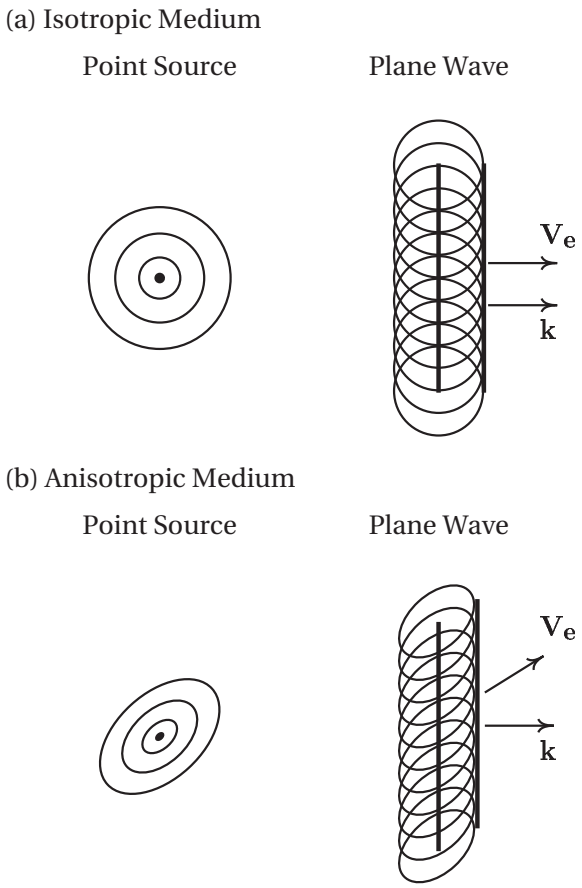


Figure 3.8: (a) Wave fronts emanating from a point isotropic source and a line source in an isotropic medium. (b) Wave fronts emanating from a point isotropic source and a line source in an anisotropic medium. In this case, the wave vector $\mathbf{k}$, which is perpendicular to the wave front, is not parallel to the energy flow, which is along the energy velocity direction, $\mathbf{V}_e$. (After Wolfe [11], p. 24)

From (3.45) follows that the group velocity is a vector which is perpendicular to the iso-frequency surface. An important property of a non-absorbing periodic medium is that, as in the case of a homogeneous medium, the energy velocity vector associated with the Bloch wave coincides with its group velocity vector. So, the iso-frequency surface fully defines directions of electromagnetic energy propagation in a photonic crystal for a given Bloch wave denoted by its wave vector.

The proof of this important statement is given here following [12]. The energy velocity is defined by

$$\mathbf{V}_e \equiv \frac{\langle \mathbf{S} \rangle}{\langle U \rangle}, \tag{3.46}$$

where the brackets $\langle\,\rangle$ denote an average over the unit cell of a periodic medium. $\mathbf{S}$ and $U$ are time-averaged Poynting's vector and electromagnetic energy density, respectively,

defined by

$$\mathbf{S} = \frac{c}{8\pi}\mathrm{Re}\left[\mathbf{E}\times\mathbf{H}^*\right], \tag{3.47}$$

$$U = \frac{1}{16\pi}\mathrm{Re}\left[\mathbf{E}\varepsilon\mathbf{E}^* + \mathbf{H}\mathbf{H}^*\right], \tag{3.48}$$

where $\varepsilon$ is a dielectric function and a periodic medium is assumed to be non-magnetic. Taking into account, that due to the Bloch theorem (chapter 2) electric and magnetic field can be written as $\mathbf{E}_\mathbf{k}(\mathbf{r}) = \mathbf{e}_\mathbf{k}(\mathbf{r})\exp(i\mathbf{kr})$ and $\mathbf{H}_\mathbf{k}(\mathbf{r}) = \mathbf{h}_\mathbf{k}(\mathbf{r})\exp(i\mathbf{kr})$, the following equation for the energy velocity can be obtained

$$\mathbf{V}_e \equiv \frac{\left\langle \frac{c}{8\pi}\mathrm{Re}\left[\mathbf{e}_\mathbf{k}\times\mathbf{h}_\mathbf{k}^*\right]\right\rangle}{\left\langle \frac{1}{16\pi}\mathrm{Re}\left[\mathbf{e}_\mathbf{k}\varepsilon\mathbf{e}_\mathbf{k}^* + \mathbf{h}_\mathbf{k}\mathbf{h}_\mathbf{k}^*\right]\right\rangle}, \tag{3.49}$$

where $\mathbf{e}_\mathbf{k}$ and $\mathbf{h}_\mathbf{k}$ are periodic functions. The Maxwell's equations for the Bloch waves transform to

$$\nabla\times\mathbf{h}_\mathbf{k} + i\mathbf{k}\times\mathbf{h}_\mathbf{k} = i\varepsilon\frac{\omega_\mathbf{k}}{c}\mathbf{e}_\mathbf{k}, \tag{3.50}$$

$$\nabla\times\mathbf{e}_\mathbf{k} + i\mathbf{k}\times\mathbf{e}_\mathbf{k} = -i\frac{\omega_\mathbf{k}}{c}\mathbf{h}_\mathbf{k}. \tag{3.51}$$

Suppose that the wave vector $\mathbf{k}$ is changed by an infinitesimal vector $\delta\mathbf{k}$. The corresponding changes in eigenfrequency, $\omega_\mathbf{k}$, electric, $\mathbf{e}_\mathbf{k}$, and magnetic, $\mathbf{h}_\mathbf{k}$, fields are denoted by $\delta\omega$, $\delta\mathbf{e}_\mathbf{k}$ and $\delta\mathbf{h}_\mathbf{k}$. Rewriting Maxwell's equations (3.50-3.51) for the eigenmode with the wave vector $\mathbf{k}+\delta\mathbf{k}$ and performing several algebraic steps, the following relation can be obtained [12]

$$\delta\omega = \mathbf{V}_e\delta\mathbf{k}, \tag{3.52}$$

where the relation (3.49) giving the energy velocity was taken into account. At the same time, from the definition of the group velocity (3.45) follows that

$$\delta\omega = \left(\nabla_\mathbf{k}\omega_\mathbf{k}\right)\delta\mathbf{k} = \mathbf{V}_g\delta\mathbf{k}. \tag{3.53}$$

The shift wave vector $\delta\mathbf{k}$ is an arbitrary vector, so finally an equality of the energy and group velocities follows from (3.52) and (3.53):

$$\mathbf{V}_e = \mathbf{V}_g. \tag{3.54}$$

Since the group velocity is defined as the derivative of the angular frequency with respect to the wave vector (3.45), it can be calculated by numerical differentiation. To perform this numerical differentiation one needs first to find a numerical solutions of dis-

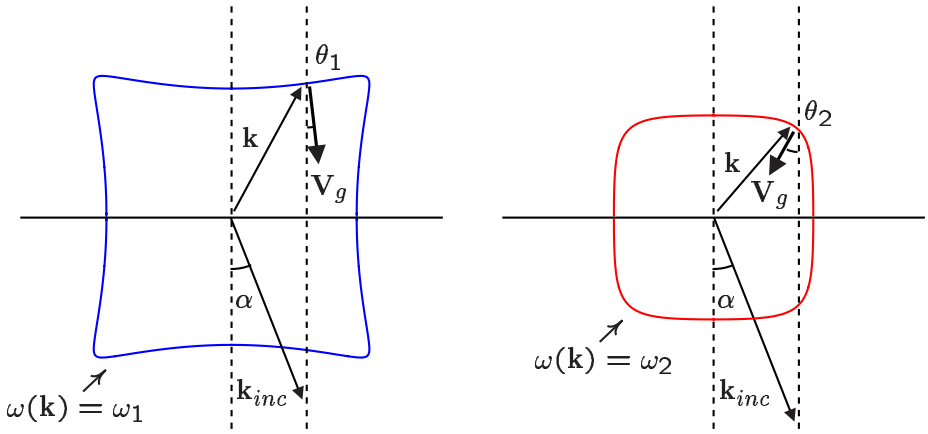


Figure 3.9: Schematic illustration of refraction at the surface of the photonic crystal depicted in figure 3.7). Iso-frequency contours are for normalized frequencies $\Omega_1 = 0.565$ (blue line) and $\Omega_2 = 0.58$ (red line). A plane wave with a wave vector $\mathbf{k}_{inc}$ is incident on the crystal surface at the same angle $\alpha$ for both frequencies. The refracted wave propagates in the direction of the group velocity $\mathbf{V}_g$.

persion relations (3.40) in the form of eigenfrequencies as a function of the wave vector. Alternatively, having a numerical solution both for eigenfrequency and corresponding eigenvector, one can calculate the group velocity avoiding numerical differentiation by application of the Hellmann-Feyman theorem [13].

### 3.2.3 Anomalous refraction

The beam steering effect known to be a reason for the number of anomalies in an electromagnetic beam propagation inside a photonic crystal. Such anomalies are usually referred to as *superprism* or *ultrarefractive phenomena* [14, 15, 16].

Anomalous refraction is a result of both form-anisotropy and strong dispersion of photonic crystal. In figure 3.9 iso-frequency contours of the two-dimensional square lattice photonic crystal (Fig. 3.7) are presented for two normalized frequencies $\Omega_1 = 0.565$ (blue curve) and $\Omega_2 = 0.58$ (red curve). Here it is assumed, that a plane wave with a wave vector $\mathbf{k}_{inc}$ is incident on the surface of the photonic crystal at an angle $\alpha$, first having the frequency $\Omega_1$ (Fig. 3.9-left) and then $\Omega_2$ (Fig. 3.9-right). The tangential component of the wave vector should be conserved at the air–crystal interface. The wave vector of a refracted wave has its end point on the iso-frequency contours given by the band structure. This condition determines the wave vector of the refracted wave. Then, the propagation direction, i. e., the direction of the energy flow, is perpendicular to the iso-frequency surface and parallel to the group velocity of the refracted wave, $\mathbf{V}_g$. In figure 3.9, the difference in the propagation directions are larger than 50° for the plane waves incident on the photonic crystal at the same incident angle $\alpha$, but

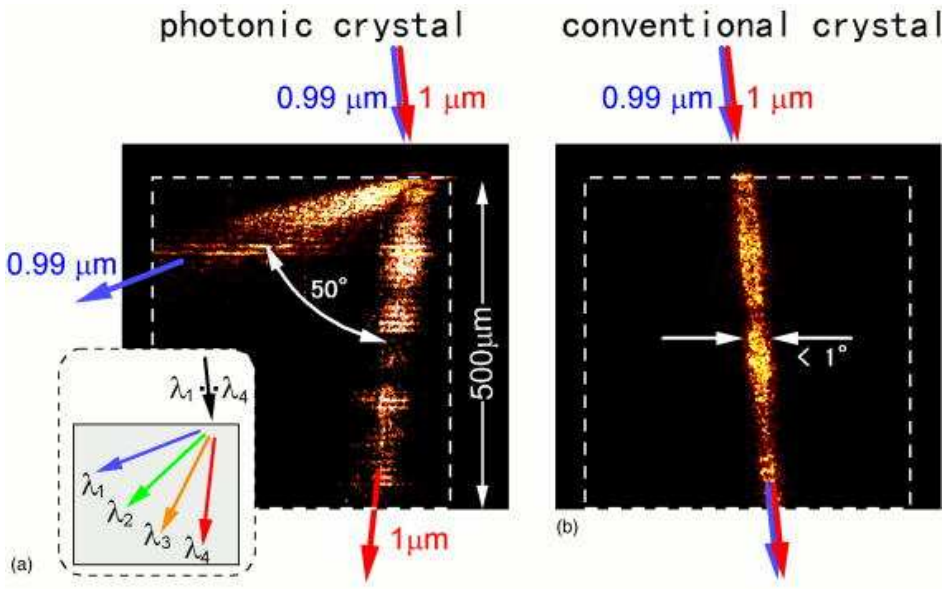


Figure 3.10: Anomalous refraction. Photographs showing refracted beams inside a photonic crystal (left) and a silicon wafer (right) for incident lights with two different wavelengths, 0.99 and 1.0 $\mu$m. The TM polarized laser lights were incident at an tilting angle of 15° measured from normal to the edge of the crystal. The photonic crystal size was 500 × 500 $\mu$m$^2$. (After Kosaka et al. [17])

having different frequencies. The relative shift of frequency is less than 3%.

In figure 3.10, an experimental demonstration of an anomalous refraction is presented in the case of laser beam interaction with a three-dimensional photonic crystal [17]. The difference in the propagation direction of refracted beam reaches 50° with only a 1% shift of incident wavelength at around 1 $\mu$m. In this example a three-dimensional photonic crystal is a graphite-like periodic medium fabricated by mean of the autocloning technique [18].

Among other optical phenomena, the appearance of which are due to beam steering, an extraordinary large or negative beam bending [16] and beam self-collimation [19] can be mentioned.

## 3.3 Spontaneous emission in photonic crystals

Purcell [20] was the first who pointed out, that the spontaneous emission of atom and molecule depends on their environment. Since then, an influence of non-trivial boundary conditions in the vicinity of an excited atom on its emissive properties has been the subject of active research [21, 22, 23]. Important examples of such an influence are an enhancement and inhibition of the spontaneous emission by a resonant environment [20], e.g., microcavity [21, 22]. These phenomena were first demonstrated by Goy

*et. al.* [24] and Kleppner [25], respectively, and continue to be the subject of intense research not only due to their contribution to the better understanding of the light matter interaction, but, to a great extent, due to the practical importance of controlling the light emission process. Light-emitting diodes [26, 27, 28] and thresholdless lasers [29, 30, 31] are just a few examples, where the light extraction and spontaneous emission control by mean of optical microcavity lead to improved performance.

Photonic crystal is a good example of non-trivial boundary conditions on the electromagnetic field, which can lead to modifications of the spontaneous emission. One of the consequence of the complete photonic bandgap is an inhibited spontaneous emission for the atomic transition frequency inside the gap [32, 33, 34].

A number of papers were devoted to the study of the spontaneous emission in photonic crystals, considering the spontaneous emission using both classical [35, 36, 37, 38, 39, 40] and quantum [32, 41, 42, 38, 43, 44, 45, 46] formalisms. It is commonly accepted that a classical description leads to the same results as an entirely quantum electrodynamical approach [35, 38]. In the classical description, the modification of the spontaneous emission is due to the radiation reaction of the back-reflected field on the classical dipole [47, 48, 49]. Then within the framework of the Weisskopf-Wigner approximation [50, 44], the spontaneous emission rate, $\Gamma$, is related to the classical radiated power $P(\mathbf{r}_0) = (\omega/2)\,\mathrm{Im}[\mathbf{d}^* \cdot \mathbf{E}(\mathbf{r}_0)]$ via $\Gamma = P/\hbar\omega$ [48], where $\mathbf{d}$ is a real dipole moment and $\mathbf{E}(\mathbf{r}_0)$ is a field in the system. A well known interpretation of the emission rate modification follows from that relation [47, 49], as the dipole interaction with the out-of-phase part of the radiation reaction field. In the classical picture, a non-relativistic Lamb shift is due to the dipole interacting with the in-phase part of the reaction field [49, 51] and it is also seen to be a purely classical effect [49, 51]. Although the magnitude of the anomalous Lamb shift in a realistic photonic crystal is actively and controversially discussed [41, 42, 43, 45], this question is out of the scope of this work.

### 3.3.1 Radiated power of classical dipole

A light source situated in an inhomogeneous medium is immersed in its own electric field emitted at an earlier time and reflected from inhomogeneities in the medium. By conservation of energy, the decay rate at which energy is radiated is equal to the rate at which the charge distribution of the source does work on the surrounding electromagnetic field. For an arbitrary current density $\mathbf{J}$, the radiated power is given by [52]:

$$P(t) = -\int_V d^3\mathbf{r}\mathbf{J}(\mathbf{r},t)\cdot\mathbf{E}(\mathbf{r},t), \tag{3.55}$$

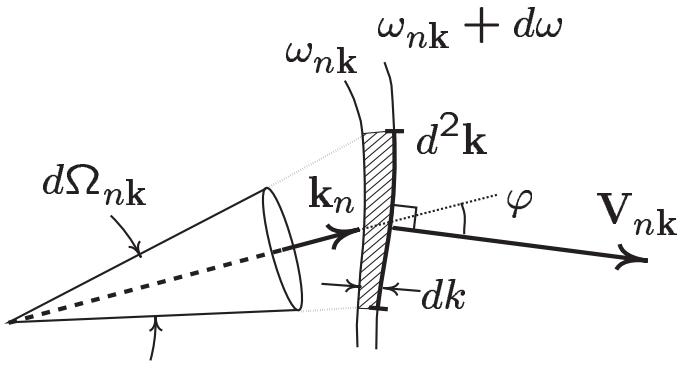


Figure 3.11: Diagram showing the relations between k-space and coordinate space quantities. Iso-frequency contours for frequencies $\omega_{n\mathbf{k}}$ and $\omega_{n\mathbf{k}} + d\omega$ are presented.

where $V$ is a volume containing a current density source $\mathbf{J}$. For the time-averaged radiated power, one has:

$$P = -\frac{1}{2}\mathrm{Re}\left[\int_V d^3\mathbf{r}\mathbf{J}^*(\mathbf{r},t)\cdot\mathbf{E}(\mathbf{r},t)\right], \tag{3.56}$$

or, specializing to a point dipole (2.38)

$$P = \frac{\omega_0}{2}\mathrm{Im}\left[\mathbf{d}^*\cdot\mathbf{E}(\mathbf{r}_0)\right]. \tag{3.57}$$

Consider an excited molecule or atom at a position $\mathbf{r}_0$ in a photonic crystal. Assuming that the presence of the molecule does not change the band structure of the crystal, the only possible mode it can emit in, is an eigenmode of the photonic crystal. In the classical approach, the molecule is modeled by a point dipole $\mathbf{d}$ (2.38). The radiation reaction field will be given by a normal mode expansion (2.41), which is valid for any point $\mathbf{r}$ in the crystal which is distinct from (but as close as required to) the dipole location $\mathbf{r}_0$. Such a choice of radiation reaction field basically corresponds to the Weisskopf-Wigner approximation [50, 44]. Then the radiated power (emission rate) (3.57) of a classical dipole in a photonic crystal is given by:

$$P = \mathrm{Im}\left[\frac{2\pi\omega_0^3}{V}\sum_n\int_{BZ} d^3\mathbf{k}_n \frac{|\mathbf{A}_{n\mathbf{k}}(\mathbf{r}_0)\cdot\mathbf{d}|^2}{(\omega_{n\mathbf{k}}^2-\omega_0^2-i\gamma)}\right]. \tag{3.58}$$

where equation (2.13), relating $\mathbf{E} = -(1/c)\partial\mathbf{A}/\partial t$, was used. With the aid of the integral representation:

$$\frac{1}{x-i\gamma} = -\frac{1}{i}\int_0^\infty d\tau e^{-ix\tau-\gamma\tau}, \tag{3.59}$$

one can transform the integral (3.58) to the form:

$$P = \mathrm{Im}\left[ i\frac{2\pi\omega_0^3}{V} \sum_n \int_{BZ} d^3\mathbf{k}_n \left|\mathbf{A}_{n\mathbf{k}}(\mathbf{r}_0)\cdot\mathbf{d}\right|^2 \int_0^\infty dt e^{i(\omega_0^2-\omega_{n\mathbf{k}}^2)t} \right]. \tag{3.60}$$

Now, making use of the time-reversal symmetry of the Maxwell's equations [53], which for a periodic medium implies that $\omega_{n,\mathbf{k}} = \omega_{n,-\mathbf{k}}$ (2.71), one can rewrite the time integral in (3.60) to obtain:

$$\int_0^\infty dt e^{i(\omega_0^2-\omega_{n\mathbf{k}}^2)t} = \frac{1}{2}\int_{-\infty}^\infty dt e^{i(\omega_0^2-\omega_{n\mathbf{k}}^2)t} = \pi\delta(\omega_0^2-\omega_{n\mathbf{k}}^2).$$

Then, the total time-averaged radiated power of a dipole is given by:

$$P = \frac{2\pi^2\omega_0^3}{V} \sum_n \int d^3\mathbf{k}_n \left|\mathbf{A}_{n\mathbf{k}}(\mathbf{r}_0)\cdot\mathbf{d}\right|^2 \delta(\omega_0^2-\omega_{n\mathbf{k}}^2). \tag{3.61}$$

The volume integral in (3.61) can be transformed to the surface integral over the iso-frequency surface $\omega_{n\mathbf{k}} = \omega_0$. Changing the integration variable to the eigenfrequency $\omega_{n\mathbf{k}}$ by using the relations $|\nabla_\mathbf{k}\omega_{n\mathbf{k}}|\, dk = d\omega_{n\mathbf{k}}$ and $d^3\mathbf{k}_n = dk d^2\mathbf{k}_n$, where $d^2\mathbf{k}_n$ is an element of the iso-frequency surface $\omega_{n\mathbf{k}} = \omega_0$ (Fig. 3.11), one has:

$$P = \frac{2\pi^2\omega_0^3}{V} \sum_n \int d^2\mathbf{k}_n \int d\omega_{n\mathbf{k}} \frac{\left|\mathbf{A}_{n\mathbf{k}}(\mathbf{r}_0)\cdot\mathbf{d}\right|^2}{|\nabla_\mathbf{k}\omega_{n\mathbf{k}}|}\delta(\omega_0^2-\omega_{n\mathbf{k}}^2),$$

where the integral over the eigenfrequency $\omega_{n\mathbf{k}}$ can be easily evaluated to obtain:

$$P = \frac{\pi^2\omega_0^2}{V} \sum_n \int d^2\mathbf{k}_n \frac{\left|\mathbf{A}_{n\mathbf{k}}(\mathbf{r}_0)\cdot\mathbf{d}\right|^2}{|\mathbf{V}_{n\mathbf{k}}|}, \tag{3.62}$$

where, $\mathbf{V}_{n\mathbf{k}} = \nabla_\mathbf{k}\omega_{n\mathbf{k}}$, the group velocity of the eigenwave $(n,\mathbf{k})$ is introduced.

The expressions (3.61) and (3.62) give the total time-averaged radiated power of a dipole situated inside a photonic crystal [35, 37]. This result agrees with fully quantum electrodynamical result for spontaneous emission rate of a two-level atom within the Weisskopf-Wigner approximation [50]. The factor $\left|\mathbf{A}_{n\mathbf{k}}(\mathbf{r}_0)\cdot\mathbf{d}\right|^2$ in (3.61) and (3.62) gives a coupling strength of the dipole moment with a photonic crystal eigenmode at the dipole position.

### 3.3.2 Enhancement and suppression of radiated power

To estimate the influence of photonic crystal upon the spontaneous emission, it is instructive to express radiated power (3.61) by the corresponding photonic total density

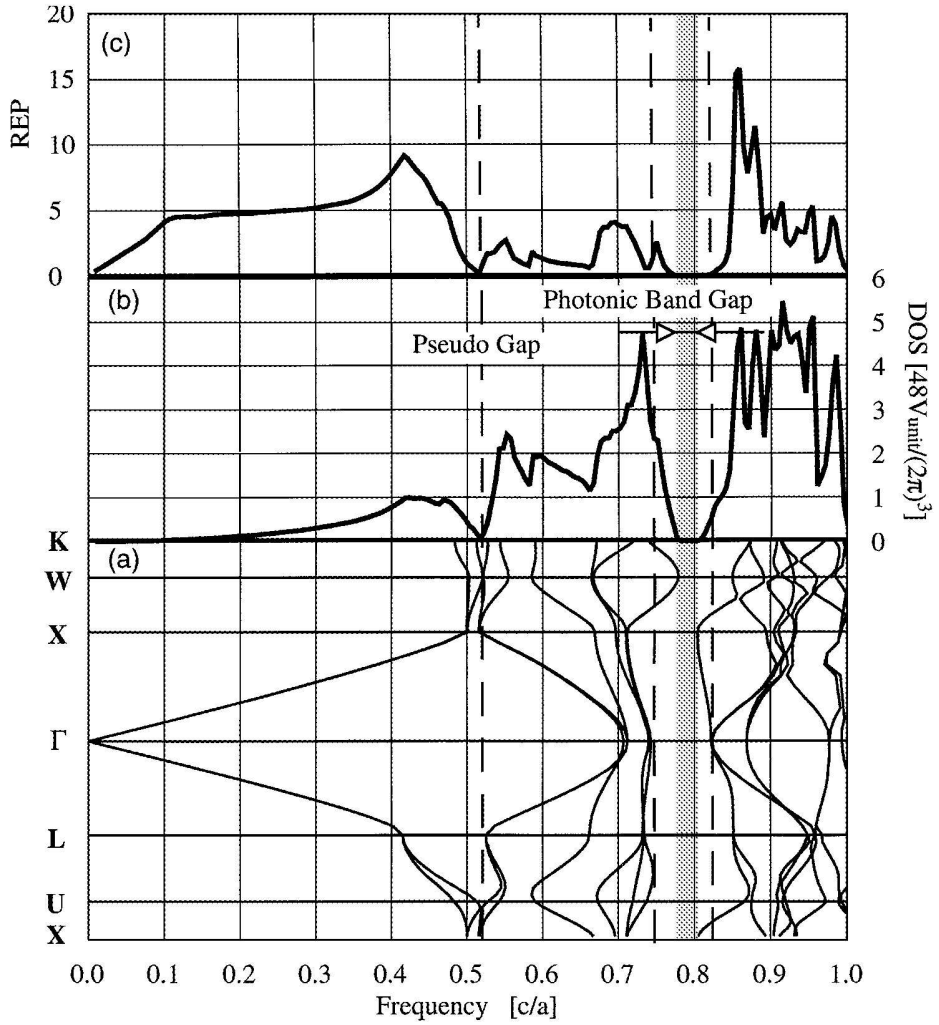


Figure 3.12: (a) Photonic band structure and (b) total DOS of a three-dimensional fcc lattice of closed packed air voids in a dielectric host. Dielectric constant of host material is $\varepsilon = 12.25$. (c) Total radiated power relative to that in free space. The oscillating dipole is situated in the host material between air voids with the dipole moment orientation along [100] direction of the fcc lattice. The frequency is normalized to $\Omega = \omega a/2\pi c = a/\lambda$. $c$ is the speed of light in the vacuum. $a$ is a period of the cubic lattice. (After Suzuki et al. [36])

of states (DOS). The total DOS is defined by

$$\rho(\omega) = \sum_n \int d^3\mathbf{k}_n \delta(\omega - \omega_{n\mathbf{k}}) = 2\omega \sum_n \int d^3\mathbf{k}_n \delta(\omega^2 - \omega_{n\mathbf{k}}^2) \tag{3.63}$$

and gives a total number of avaliable eigenmodes of a periodic medium with eigenfrequency $\omega$. Then, assuming that the coupling strength $|\mathbf{A}_{n\mathbf{k}}(\mathbf{r}_0) \cdot \mathbf{d}|^2$ is on average the same for all photonic crystal eigenmodes, the total radiated power (3.61) can be

approximated as

$$P(\omega) \approx \frac{\pi^2 \omega_0^2}{V} \overline{|\mathbf{A}_{n\mathbf{k}}(\mathbf{r}_0) \cdot \mathbf{d}|^2} \rho(\omega), \tag{3.64}$$

where $\overline{|\mathbf{A}_{n\mathbf{k}}(\mathbf{r}_0) \cdot \mathbf{d}|^2}$ denotes the averaged value of $|\mathbf{A}_{n\mathbf{k}}(\mathbf{r}_0) \cdot \mathbf{d}|^2$. The radiated power of the oscillating dipole is thus proportional to the total DOS $\rho(\omega)$. If the total DOS is equal to zero in a certain frequency range, no dipole radiation takes place. On opposite, if the total DOS is larger than an appropriate DOS in vacuum, the radiated power can be enhanced with respect to the dipole radiation in free space. These lead to the observation that the spontaneous emission rate can be suppressed or enhanced in a photonic crystal environment [32, 33].

The photonic band structure of a three-dimensional face-centered cubic (fcc) lattice of closed packed air voids in a dielectric host and the corresponding total DOS are presented in figure 3.12 [36]. Such a photonic crystal possesses a complete photonic bandgap between 8th and 9th bands, which leads to zero total DOS and radiated power for the corresponding frequency region. In is important to note, that suppression and enhancement of radiated power do not exactly follow the total DOS, because the coupling strength $|\mathbf{A}_{n\mathbf{k}}(\mathbf{r}_0) \cdot \mathbf{d}|^2$ can vary for different dipole locations and dipole moment orientations.

An intrinsic properties of a photonic crystal is that its band structure can be engineered by choosing an appropriate combination of materials and lattice geometry [53, 13]. This opens an opportunity to modify in purpose the spontaneous emission rate, enhancing and suppressing it within specified spectral ranges.

# Bibliography


[1] H. A. Macleod, *Thin-Film Optical Filters* (Adam Hilger, Bristol, 1986).

[2] J. D. Rancourt, *Optical Thin Films: Users' Handbook* (Macmillan Publishing Company, New York, 1987).

[3] P. Yeh, *Optical Waves in Layered Media* (John Wiley and Sons, New York, 1988).

[4] M. Born and E. Wolf, *Principles of Optics* (Pergamon, New York, 1980).

[5] P. Yeh, A. Yariv, and C.-S. Hong, "Electromagnetic propagation in periodic stratified madia. I. General theory," *J. Opt. Soc. Am.* **67,** 423–437 (1977).

[6] K. M. Ho, C. T. Chan, and C. M. Soukoulis, "Existence of a photonic gap in periodic dielectric structures," *Phys. Rev. Lett.* **65,** 3152–3155 (1990).

[7] H. S. Sozuer, J. W. Haus, and R. Inguva, "Photonic bands: Convergence problems with the plane-wave method," *Phys. Rev. B* **45,** 13962–13972 (1992).

[8] R. D. Meade, A. M. Rappe, K .D. Brommer, and J. D. Joannopoulos, "Accurate theoretical analysis of photonic band-gap materials," *Phys. Rev. B* **48,** 8434–8437 (1993).

[9] S. G. Johnson and J. D. Joannopoulos, "Block-iterative frequency-domain methods for Maxwell's equations in a planewave basis," *Optics Express* **8,** 173–190 (2001).

[10] D. Hermann, M. Frank, K. Busch, and P. Wolfle, "Photonic band structure computations," *Optics Express* **8,** 167–172 (2001).

[11] J. P. Wolfe, *Imaging Phonons: Acoustic Wave Propagation in Solid* (Cambridge University Press, Cambridge, 1998).

[12] P. Yeh, "Electromagnetic propagation in birefringent layered media," *J. Opt. Soc. Am.* **69,** 742–756 (1979).

[13] K. Sakoda, *Optical Properties of Photonic Crystals* (Springer, Berlin, 2001).

[14] P. St. J. Russell, "Optics of Floquet-Block waves in dielectric gratings," *Appl. Phys. B: Photophysics & Laser Chemistry* **B39,** 231–246 (1986).

[15] R. Zengerle, "Light propagation in singly and doubly periodic planar waveguides," *J. Mod. Optics* **34,** 1589–1617 (1987).

[16] H. Kosaka, T. Kawashima, A. Tomita, M. Notomi, T. Tamamura, T. Sato, and S. Kawakami, "Superprism phenomena in photonic crystals," *Phys. Rev. B* **58,** R10096–R10099 (1998).

[17] H. Kosaka, T. Kawashima, A. Tomita, M. Notomi, T. Tamamura, T. Sato, and S. Kawakami, "Photonic crystals for micro lightwave circuits using wavelength-dependent angular beam steering," *Appl. Phys. Lett.* **74,** 1370–1372 (1999).

[18] T. Sato, K. Miura, N. Ishino, Y. Ohtera, T. Tamamura, and S. Kawakami, "Photonic crystals for the visible range fabricated by autocloning technique and their applications," *Opt. Quantum Electron.* **34,** 63–77 (2002).

[19] H. Kosaka, T. Kawashima, A. Tomita, M. Notomi, T. Tamamura, T. Sato, and S. Kawakami, "Self-collimating phenomena in photonic crystals," *Applied Physics Letters* **74,** 1212–1214 (1999).

[20] E. M. Purcell, "Modification of spontaneous emission," *Phys. Rev.* **69,** 681 (1946).

[21] *Spontaneous Emission and Laser Oscillation in Microcavities*, H. Yokoyama and K. Ujihara, eds., (CRC Press, Boca Raton, 1995).

[22] *Confined Electrons and Photons: New Physics and Applications*, E. Burstein and C. Weisbuch, eds., (Plenum Press, New York, 1995).

[23] *Electron Theory and Quantum Electrodynamics: 100 Years Later*, J. P. Dowling, ed., (Plenum Press, New York, 1997).

[24] P. Goy, J. M. Raimond, M. Gross, and S. Haroche, "Observation of cavity-enhanced single-atom spontaneous emission," *Phys. Rev. Lett.* **50,** 1903–1906 (1983).

[25] D. Kleppner, "Inhibited spontaneous emission," *Phys. Rev. Lett.* **47,** 233–236 (1981).

[26] H. Benisty, H. De Neve, and C. Weisbuch, "Impact of planar microcavity effects on light extraction-Part I: basic concepts and analytical trends," *IEEE J. Quantum Electron.* **34,** 1612–1631 (1998).

[27] H. Benisty, H. De Neve, and C. Weisbuch, "Impact of planar microcavity effects on light extraction-Part II: selected exact simulations and role of photon recycling," *IEEE J. Quantum Electron.* **34,** 1632–1643 (1998).

[28] D. Delbeke, R. Bockstaele, P. Bienstman, R. Baets, and H. Benisty, "High-efficiency semiconductor resonant-cavity light-emitting diodes: A review," *IEEE J Sel. Top. Quant.* **8,** 189–206 (2002).

[29] H. Yokoyama and S. D Brorson, "Rate equation analysis of microcavity lasers," *J. Appl. Phys.* **66,** 4801–4805 (1989).

[30] G. Bjork, H. Heitmann, and Y. Yamamoto, "Spontaneous-emission coupling factor and mode characteristics of planar dielectric microcavity lasers," *Phys. Rev. A* **47,** 4451–4863 (1993).

[31] G. Bjork, A. Karlsson, and Y. Yamamoto, "Definition of a laser threshold," *Phys. Rev. A* **50,** 1675–1680 (1994).

[32] V. P. Bykov, "Spontaneous emission in a periodic structure," *Soviet Physics - JETP* **35,** 269–273 (1972).

[33] E. Yablonovitch, "Inhibited spontaneous emission in solid-state physics and electronics," *Phys. Rev. Lett.* **58,** 2059–2062 (1987).

[34] S. John, "Strong localization of photons in certain disordered dielectric superlattices," *Phys. Rev. Lett.* **58,** 2486–2489 (1987).

[35] J. P. Dowling and C. M. Bowden, "Atomic emission rates in inhomogeneous media with applications to photonic band structures," *Phys. Rev. A* **46,** 612–622 (1992).

[36] T. Suzuki and P. K. L. Yu, "Emission power of an electrical dipole in the photonic band structure of the fcc lattice," *J. Opt. Soc. Am. B* **12,** 570–582 (1995).

[37] K. Sakoda and K. Ohtaka, "Optical response of three-dimensional photonic lattices: Solutions of inhomogeneous Maxwell's equations and their applications," *Phys. Rev. B* **54,** 5732–5741 (1996).

[38] Y. Xu, R. K. Lee, and A. Yariv, "Quantum analysis and classical analysis of spontaneous emission in a microcavity," *Phys. Rev. A* **61,** 033807 (2000).

[39] V. Lousse, J. P. Vigneron, X. Bouju, and J. M. Vigoureux, "Atomic radiation rates in photonic crystals," *Phys. Rev. B* **64,** 201104R (2001).

[40] C. Hermann and O. Hess, "Modified spontaneous-emission rate in an inverted-opal structure with complete photonic bandgap," *J. Opt. Soc. Am. B* **19,** 3013–3018 (2002).

[41] S. John and J. Wang, "Quantum electrodynamics near a photonic nand gap: photon bound state and dressed atoms," *Phys. Rev. Lett.* **64,** 2418–2421 (1990).

[42] S. Y. Zhu, Y. Yang, H. Chen, H. Zheng, and M. S. Zubairy, "Spontaneous radiation and Lamb shift in three-dimensional photonic crystals," *Phys. Rev. Lett.* **84,** 2136–2139 (2000).

[43] Z. Y. Li, L. L. Lin, and Z. Q. Zhang, "Spontaneous emission from photonic crystals: full vectorial calculations," *Phys. Rev. Lett.* **84,** 4341–4344 (2000).

[44] K. Busch, N. Vats, S. John, and B. C. Sanders, "Radiating dipole in photonic crystals," *Phys. Rev. E* **62,** 4251–4260 (2000).

[45] Z. Y. Li and Y. Xia, "Full vectorial model for quantum optics in three-dimensional photonic crystals," *Phys. Rev. A* **63,** 043817 (2001).

[46] M. Woldeyohannes and S. John, "Coherent control of spontaneous emission near a photonic band edge," *J. Opt. B: Quantum Semiclass. Opt.* **5,** R43–R82 (2003).

[47] J. E. Sipe, "The dipole antenna problen in surface physics: a new approach," *Surf. Sci.* **105,** 489–504 (1981).

[48] G. W. Ford and W. H. Weber, "Electromagnetic interactions of molecules with metal surfaces," *Phys. Rep.* **113,** 195–287 (1984).

[49] J. M. Wylie and J. E. Sipe, "Quantum electrodynamics near an interface," *Phys. Rev. A* **30,** 1185–2043 (1984).

[50] R. J. Glauber and M. Lewenstein, "Quantum optics of dielectric media," *Phys. Rev. A* **43,** 467–491 (1991).

[51] J. P. Dowling, "The classical Lamb shift: why Jackson is wrong!," *Found. Phys.* **28,** 855–862 (1998).

[52] J. D. Jackson, *Classical Electrodynamics* (John Wiley, New York, 1975).

[53] J. D. Joannopoulos, R. D. Meade, and J. N. Winn, *Photonic crystals: molding the flow of light* (Princeton University Press, Princeton NJ, 1995).

# Part II

# Reflection

# Chapter 4

# Omnidirectional Bragg mirror[1]

Probably one of the most widespread application of one-dimensional periodic media is a Bragg mirror. Mirrors come in two basic varieties: a metallic mirror with dissipative losses of few-percent, being in fact an omnidirectional reflector, and a dielectric Bragg mirror. A dielectric Bragg mirror can be made nearly lossless, but it is typically highly reflecting only within a limited angular range. A structure combining the properties of both mirror types, i.e., being omnidirectional and lossless, is of strong interest as it is likely to find many applications in optoelectronics and all-optical systems. Until recently, the possibility to design such a "perfect mirror" was exclusively associated with three-dimensional photonic crystals having a complete photonic bandgap. In this chapter, it is reported, that a simple-to-fabricate Bragg mirror suffices to design a low-loss omnidirectional reflector [1, 2, 3, 4]. In section 4.1 basic design criteria to obtain an omnidirectional reflection with a Bragg mirror are presented. A way to design an omnidirectional mirror with a maximum spectral bandwidth is given in section 4.2. A comparison of the theoretical predictions with experimental results is presented in section 4.3 for optical frequencies. Section 4.4 summarizes this chapter.

## 4.1 Omnidirectional reflectance

A Bragg mirror is a one-dimensional periodic medium. In this case the dielectric function is periodic in one direction, $\varepsilon(z + l\Lambda) = \varepsilon(z)$, where $z$ is the direction of periodicity, $\Lambda = d_1 + d_2$ is the period and $l$ is an integer (Fig. 4.1). The dispersion

[1]This chapter is based on: D. N. Chigrin, A. V. Lavrinenko, D. A. Yarotsky, and S. V. Gaponenko, "Observation of total omnidirectional reflection from a one-dimensional dielectric lattice," *Appl. Phys. A* **68**, 25–28 (1999); D. N. Chigrin, A. V. Lavrinenko, D. A. Yarotsky, and S. V. Gaponenko, "All-dielectric one-dimensional periodic structures for total omnidirectional reflection and partial spontaneous emission control," *J. Lightwave Tech.* **17**, 2018–2024 (1999).

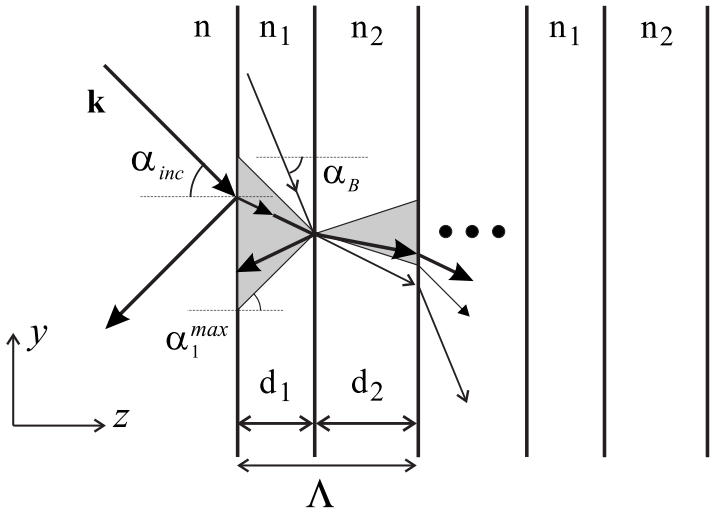


Figure 4.1: Schematic representation of a one-dimensional periodic medium. The coordinate system and light rays refracting and propagating through a stack are shown. Refractive indices of alternating regions and an ambient medium are $n_1$, $n_2$ ($n_1 < n_2$) and $n$, respectively. Thicknesses of alternating regions are $d_1$ and $d_2$. $\Lambda = d_1 + d_2$ is the period. The full domain of incident angles $\alpha_{inc}$ in the range from $-\pi/2$ to $\pi/2$ is mapped onto the internal cone of half-angle $\alpha_1^{max} = \arcsin n/n_1$ (light gray area). $\alpha_B$ is the Brewster angle.

relation of Bloch waves in such a medium can be derived analytically [5, 6] (chapter 3)

$$K\left(\omega, \mathbf{k}_{\|}\right) = \frac{1}{\Lambda} \arccos\left[\frac{1}{2}\left(A + D\right)\right]. \tag{4.1}$$

A particular form of the functions $A\left(\omega, \mathbf{k}_{\|}\right)$ and $D\left(\omega, \mathbf{k}_{\|}\right)$ may be found elsewhere [5, 6] (e.g. chapter 3), here $K$ is the Bloch wave number and $\mathbf{k}_{\|}$ is the tangential component of the Bloch wave vector.

The projected band structure of an infinite periodic layered medium is depicted in the figure 4.2. The refractive indices, $n_1 = 1.4$ and $n_2 = 3.4$, are chosen close to those of $SiO_2$ and Si in the near IR region. The layers have equal thickness ($d_1 = d_2$), which corresponds to the filling fraction $\eta = 0.5$, where the filling fraction is defined via $\eta = d_2/\left(d_1 + d_2\right)$. An infinite periodic structure can support both propagating and evanescent Bloch waves. In figure 4.2, grey areas correspond to the propagating states, whereas white areas contain the evanescent states only and are referred to as photonic bandgaps.

When the frequency and the wave vector of a wave, impinging externally at an angle, $\alpha_{inc}$, from a homogeneous medium of refractive index $n$ onto a one-dimensional periodic medium (Fig. 4.1), lies within the bandgaps, the incident wave undergoes strong reflection. Pronounced high reflection bands depend strongly on frequency and

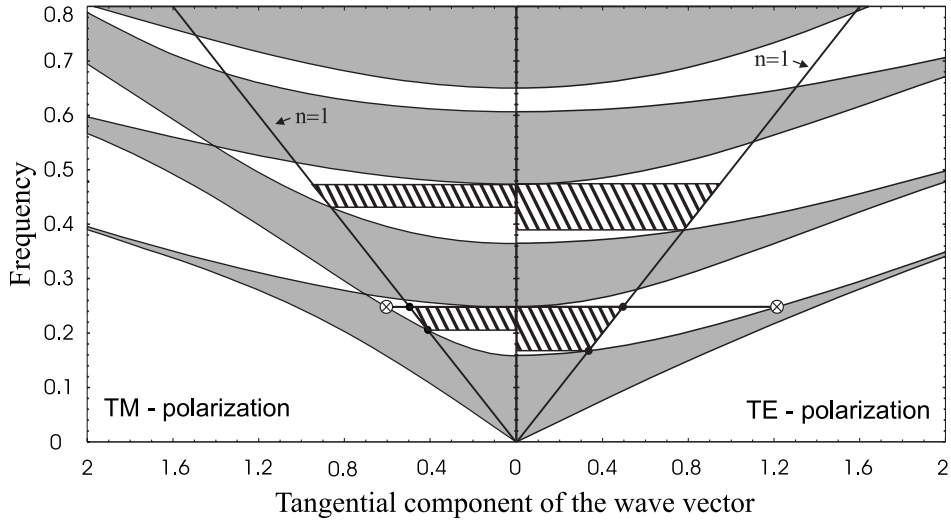


Figure 4.2: Projected band structure of a typical 1D photonic crystal for TE (right panel) and TM (left panel) polarizations. The frequency and the tangential component of the wave vector are defined to be normalized as $\omega\Lambda/2\pi c$ and $\left|\mathbf{k}_{\|}\right|\Lambda/\pi$, respectively. The hatched areas correspond to omnidirectional reflection bands. The solid lines are the ambient-medium light-lines.

angle of incidence. These can be easily understood from figure 4.2. Photonic bandgaps *(i) rapidly move to higher frequencies with increasing incident angle, denoted by the increase of the tangential component of the wave vector,* and *(ii) the TM band gaps tends to zero when approaching the Brewster light-line*, where $\omega = c\left|\mathbf{k}_{\|}\right|/n_1 \sin\alpha_B$ (Fig. 4.2), and $\alpha_B = \arctan n_2/n_1$ is the Brewster angle at $n_1 - n_2$ interface. These properties of the band structure restrict the angular aperture of a polarization insensitive range of high reflectance.

In essence, omnidirectional reflectance can be achieved due to the limitation of the number of modes that can be excited by externally incident waves inside the Bragg mirror. Light coming from the low-index ambient medium ($n < n_1, n_2$) is funneled into the internal cone narrowed by Snell's law (Fig. 4.1). Then, *(i) a sufficiently large contrast between refractive indices of layers constituting the periodic medium with respect to a refractive index of an ambient medium ensures that light coming from the outside will never go below the Brewster's angle inside the crystal* (Fig. 4.1) *and (ii) a sufficiently large refractive index contrast of the layers themselves can keep the bandgaps open up to grazing angles* [1, 2, 3, 4].

A reduced region of **k**-space, where propagating Bloch modes of the photonic crystals can be excited by externally incident wave, lies above the light-line (Fig. 4.2), which is a projection of the band structure of an ambient medium on the $\omega\left|\mathbf{k}_{\|}\right|$ plane. For example, in the case of the $Si/SiO_2$ periodic medium situated in air the first two bandgaps are open for all external angles of incidence (hatched areas in figure 4.2).

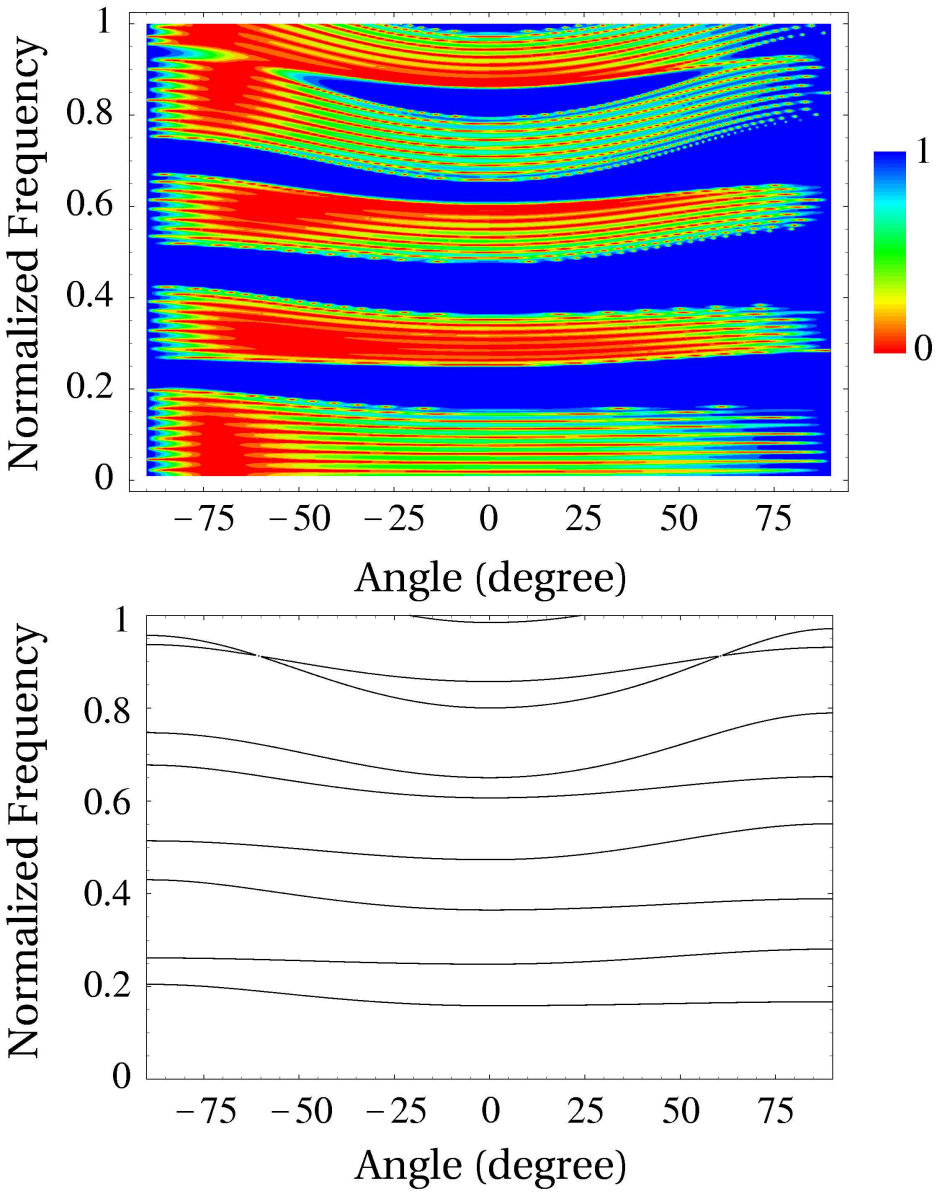


Figure 4.3: Top: A two-dimensional map of reflectivity spectrum of a 10-period Bragg reflector for TE (right) and TM (left) polarizations. Bottom: Photonic band structure of the corresponding infinite periodic medium projected onto the $\omega\alpha_{inc}$ plane. Here $\alpha_{inc}$ is angle of incidence, which is related to the tangential component of the wave vector via $\left|\mathbf{k}_{\|}\right| = (\omega/c)\, n \sin\alpha_{inc}$. The light impinges on the Bragg mirror from air ($n = 1.0$). The indices of refraction are $n_1 = 1.4$ and $n_2 = 3.4$, and the layers thicknesses are equal, $d_1 = d_2$ (see Fig. 4.2).

No propagating mode is allowed in the stack for any propagating mode in the ambient medium for either polarizations. This is how total omnidirectional reflection arises.

The reflectivity of such an omnidirectional Bragg reflector as a function of frequency and angle of incidence is presented in figure 4.3-top. The reflectivity was calculated using the transfer matrix method [7, 5] (chapter 3). The light impinges on the 10-

period Bragg mirror from air ($n = 1$). The total reflection is colored blue; the vanishing reflection is colored red. The bands of high omnidirectional reflection are clearly seen in the reflectivity spectrum.

The photonic band structure of the infinite periodic medium (Fig. 4.2) projected onto the $\omega\alpha_{inc}$ plane is presented in figure 4.3-bottom for comparison. The projected band structure (Fig. 4.2) is related to the projected band structure (Fig. 4.3-bottom) via $\left|\mathbf{k}_{\parallel}\right| = (n\omega/c)\sin\alpha_{inc}$, which relates the tangential component of the wave vector with the angle of incidence $\alpha_{inc}$. Regions of high reflection coincide with the forbidden bands of the periodic medium.

## 4.2 Optimization of an omnidirectional mirror

To design an omnidirectional mirror, one needs to have total reflection for all incident angles and all polarization states. The TM photonic band gap is narrower than the TE one and this determines the bandwidth of an omnidirectional reflection band. The upper edge of the reflection band corresponds to the upper edge of the forbidden gap at normal incidence. The lower edge is defined by the intersection of the ambient-medium light-line with the upper edge of the corresponding TM band (Fig. 4.2).

For given parameters of the periodic structure, the refractive index of an ambient medium may be used to control the bandwidth. By increasing the refractive index of an ambient medium from $n = 1$ to some $n = n_{max}$ the bandwidth decreases till an omnidirectional reflection band is closed. In figure 4.4 the maximum refractive index of the ambient medium $n_{max}$, for which the first omnidirectional reflection band is closed up, is presented as a function of the index ratio $\delta n = n_2/n_1$ for various values of the refractive index of the low index layer $n_1$ and the fixed filling fraction $\eta = d_2/\Lambda = 0.5$.

The filling fraction $\eta = d_2/\Lambda$ optimizes the relative reflection bandwidth $\Delta\omega/\omega_0$ of an omnidirectional reflection band with respect to the given refractive indices of the layers constituting one-dimensional periodic medium and the index of an ambient medium. Here $\Delta\omega$ is the width of the omnidirectional reflection band and $\omega_0$ is its central frequency. In figure 4.5 overall band gaps leading to the omnidirectional total reflection bands are presented versus the filling fraction. For the first overall band gap, gaps corresponding to the normal and grazing incidence are presented. The solid curves correspond to normal incidence. The dashed (dotted) curves are for grazing incidence of TE (TM) polarized light. The omnidirectional reflection band, which is due to the overlap of the gaps corresponding to the normal and grazing incidence, is depicted as the hatched area. The omnidirectional reflection bands of the higher order are opened. The inset in figure 4.5 shows the relative bandwidth of the first total reflection band

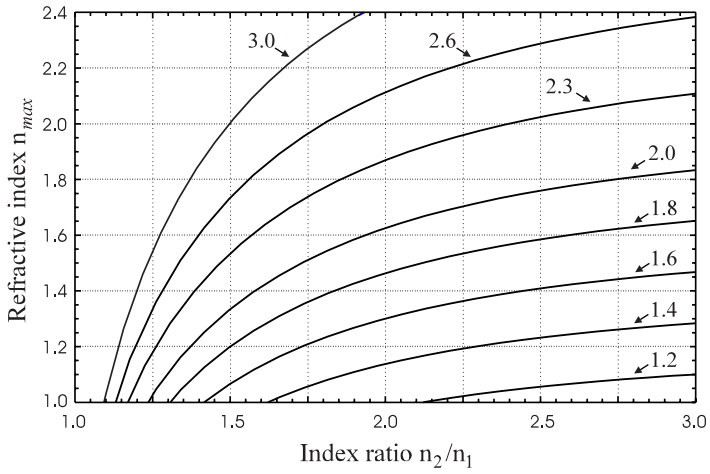


Figure 4.4: Maximum refractive index of an ambient medium, for which the omnidirectional reflection band is closedobtained, as a function of the index ratio $\delta n = n_2/n_1$ for different values of refractive index of the low index layer, $n_1$, and fixed filling fraction $\eta = 0.5$. Numbers at the curves indicate the refractive index of the low index layer, $n_1$.

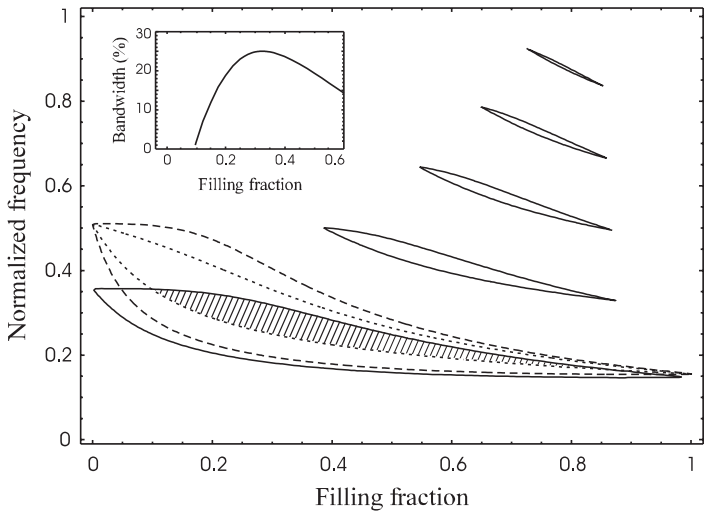


Figure 4.5: Overall band gaps leading to omnidirectional total reflection bands. For the first overall band gap, gaps corresponding to normal and grazing incidence are presented. The hatched area denotes the first omnidirectional reflection band. The solid curves indicates normal incidence. The dashed (dotted) curves are for grazing incidence for TE (TM) polarization. The inset shows the relative bandwidth versus filling fraction. Here $n = 1$, $n_1 = 1.4$ and $n_2 = 3.4$.

versus filling fraction. There is a clear optimum filling fraction $\eta_{opt}$ leading to the maximum of the relative bandwidth.

In figure 4.6 a set of contour plots, which provides full information about the first omnidirectional total reflection band for given parameters of the system is presented. An optimal filling fraction and corresponding central frequency are shown in

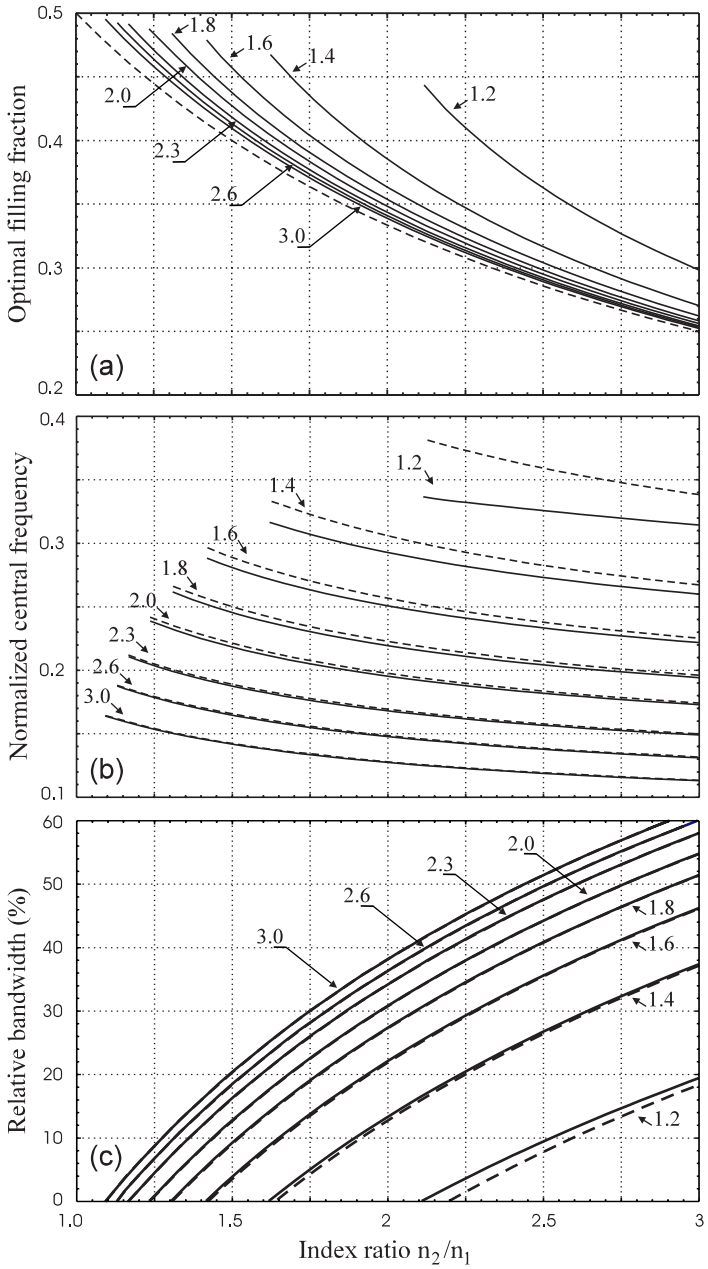


Figure 4.6: (a) Optimal filling factor $\eta_{opt}$ as a function of the index ratio $\delta n$ for different values of index ratio $\delta n_0$. (b) Central frequency $\omega_0$ as a function of the index ratio $\delta n$ for different values of index ratio $\delta n_0$ for optimal filling factor $\eta_{opt}$. (c) Relative bandwidth $\Delta\omega/\omega_0$ as a function of the index ratio $\delta n$ for different values of index ratio $\delta n_0$ for optimal filling factor $\eta_{opt}$. Numbers at the curves indicate the index ratio $\delta n_0$. Dashed curves correspond to the quarter-wave stack.

figures 4.6 (a) and 4.6 (b), respectively, as functions of the index ratio $\delta n = n_2/n_1$ for different values of index ratio $\delta n_0 = n_1/n$. The dashed curve in figure 4.6 (a) corresponds to the filling factor of a quarter-wave stack, which is $\eta_{\lambda/4} = 1/(1+\delta n)$. Within a given parameter range a quarter-wave stack is not an optimal configuration to reach a

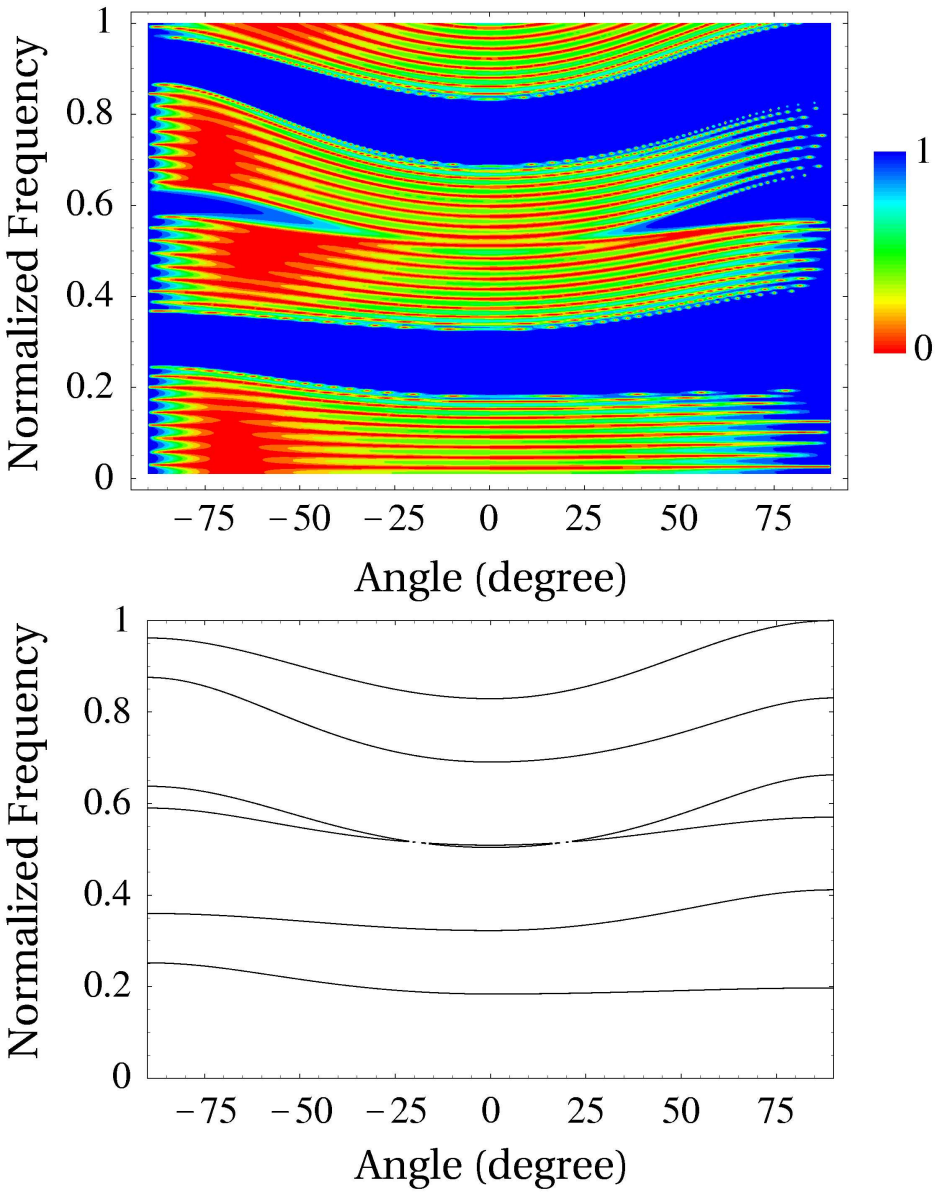


Figure 4.7: Top: A two-dimensional map of the reflectivity spectrum of a 10-period Bragg reflector for TE (right) and TM (left) polarizations. Bottom: Photonic band structure of the corresponding infinite periodic medium projected onto the $\omega\alpha_{inc}$ plane. Here $\alpha_{inc}$ is angle of incidence, which is related to the tangential component of the wave vector via $\left|\mathbf{k}_{\|}\right| = (\omega/c)\, n \sin\alpha_{inc}$. The light impinges on the Bragg mirror from air ($n = 1.0$). The indices of refraction are $n_1 = 1.4$ and $n_2 = 3.4$, and filling fraction is $\eta_{opt} = d_2/\Lambda = 0.324$.

maximum relative bandwidth for the omnidirectional reflection band, however it gives the relative bandwidth, which is usually a few percent smaller than for optimal one [Fig. 4.6 (c)]. In figure 4.6 (c) the optimal relative bandwidth is depicted as a function of the index ratio $\delta n$ for different values of index ratio $\delta n_0$. A wide omnidirectional total reflection band exists for reasonable values of both $\delta n$ and $\delta n_0$. To obtain an

omnidirectional band with bandwidth larger than 5% the index ratio should be larger than 1.5 ($\delta n > 1.5, \delta n_0 > 1.5$). A decrease in one of the index ratios is partially compensated by an increase in the other one.

For the $SiO_2$/Si ($n_1 = 1.4$, $n_2 = 3.4$) structure in air ($n = 1.0$) the omnidirectional reflection band is centered at the normalized frequency $\omega\Lambda/2\pi c = 0.275$ with the optimal filling fraction $\eta_{opt} = 0.324$. The relative bandwidth is about 25%. For example, to obtain an omnidirectional reflection centered at the wavelength $\lambda = 1.5\,\mu m$, the period of the structure should be about $0.412\,\mu m$.

The reflectivity of a 10-period $SiO_2$/Si omnidirectional Bragg reflector as a function of frequency and angle of incidence together with its corresponding photonic band structure projected onto the $\omega\alpha_{inc}$ plane are presented in figure 4.7 for the optimal filling fraction $\eta_{opt} = 0.324$. The reflectivity was calculated using the transfer matrix method [7, 5] (chapter 3). The light impinges on the 10-period Bragg mirror from air ($n = 1$). The total reflection is colored blue; the vanishing reflection is colored red. A wide omnidirection band of high reflection is clearly seen in the reflectivity spectrum for frequencies near $\omega\Lambda/2\pi c = 0.275$.

## 4.3 Comparison with experiment

In this section, experimental results obtained at the Institute of Molecular and Atomic Physics (Belarusian Academy of Sciences, Minsk, Belarus) [2, 4], on the omnidirectional Bragg mirror are compared with theoretical predictions presented in section 4.1. To check theoretical predictions, a Bragg mirror in the optical wavelength range was chosen.

A lattice consisting of 19 layers of $Na_3AlF_6$ and ZnSe ($n_1 = 1.34$ and $n_2 \in [2.5, 2.8]$ correspondingly) was fabricated by standard optical technology using layer by layer deposition of the materials on a glass substrate [2, 4]. The multilayer stack was terminated at both ends with ZnSe layer. The thickness of each layer was $d_1 = d_2 =$ 90 nm. An omnidirectional total reflection was expected within the spectral band $\Delta\lambda \in [604.3, 638.4]$ nm with a relative bandwidth of 5.3%.

Transmission spectra for TE- and TM- polarizations at different incident angles in the range of $0 - 60^\circ$ were measured using a Cary 500 spectrophotometer (right panel in figure 4.8). The calculated transmission spectra are depicted in the left panel of the figure 4.8, a good agreement is obtained. From figure 4.8 one can see that for spectral range 600–700 nm the transmission coefficient is very low for both polarizations. For example, the absolute values of transmission for TE-polarization in spectral range 600–700 nm was less than 0.001 within the $\pm 0 - 60^\circ$ aperture, corresponding to a reflection

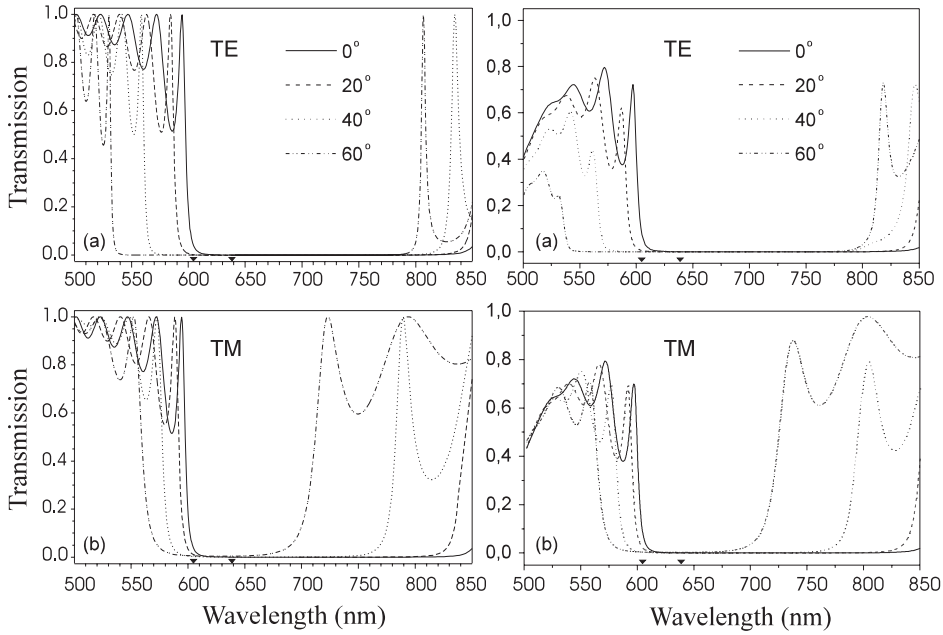


Figure 4.8: Calculated transmission spectra (left panel) and measured transmission spectra (right panel) of $Na_3AlF_6$/ZnSe 19-layer structure for TE-polarized (a) and TM-polarized (b) light at different angles of incidence (0°–solid line, 20°–dashed line, 40°–dotted line, 60°–dash-dotted line). The triangles indicate the calculated edges of the omnidirectional reflection band.

coefficient of 99.9%.

To reach larger values of angle of incidence a simple set-up consisting of a He-Ne laser and a CCD detector was used. The intensity of the laser beam passed through the sample was detected by CCD camera. The sample was mounted on rotational stage to allow different angles of incidence. With this set-up one can directly determine the transmission coefficient of samples at angles up to 70°. For larger angles it is necessary to measure the reflection coefficient of samples. The dependence of the transmission coefficients for TE- and TM-polarized incident radiation of a He-Ne laser at 632.8 nm on angle of incidence is presented in the figure 4.9. For TM-polarization circles depict the directly measured transmission coefficient, and squares depict data obtained from reflection measurements. Mismatch between them can be explained by additional reflection from air–ZnSe, ZnSe–substrate and substrate–air interfaces. The solid (dashed) curve in the figure 4.9 gives theoretically calculated transmission coefficients for TE-(TM-) polarized light.

As can be seen in figure 4.9, the transmission coefficient of TM-polarized radiation remains below $10^{-3}$ over a wide angular range. Due to the Brewster effect at the air–ZnSe, ZnSe–substrate and substrate–air interfaces at large angles, it increases to 0.33 at 80° and then decreases again. In contrast, the transmission of TE-polarized

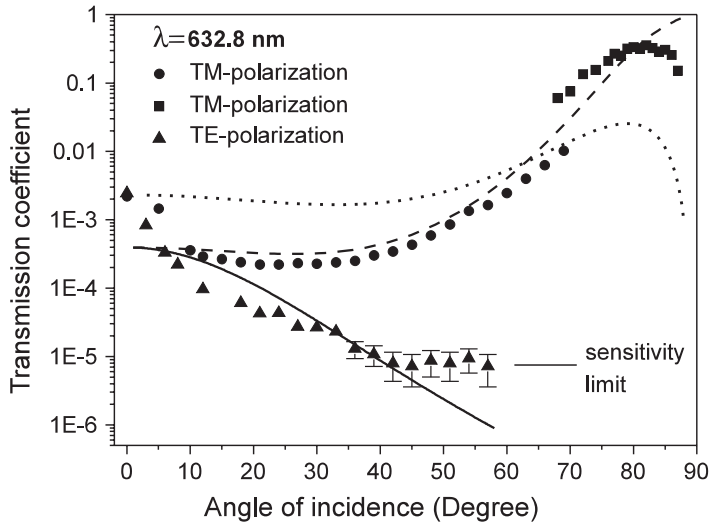


Figure 4.9: Dependence of the transmission coefficient of a $Na_3AlF_6$/ZnSe structure on angles of incidence at 632.8 nm (HeNe laser) for two polarizations of incident light. Circles denote the measured transmission coefficients for TM polarized light. Squares mark transmission coefficients calculated from reflection measurement data. For TE-polarization (triangles) the signal at angles larger than 60° is out of the sensitivity range of the experimental set-up. The solid (dashed) curve is the theoretically calculated transmission coefficient for TE- (TM-) polarized light. The dotted curve corresponds to the transmission coefficient of the structure terminated at both ends with a low index layer, $Na_3AlF_6$, for TM-polarized light.

radiation decreases monotonically with growing angle of incidence being less than $10^{-5}$ for angles larger than 40°. Transmission coefficients of less than $10^{-5}$ are beyond the capabilities of the experimental set-up used. For this reason, the transmitted signal at angles of incidence larger than 60° cannot be detected and therefore no data points for TE-polarization at these angles are presented in the figure 4.9.

The reflectivity of TM-polarized radiation at large angles can be enhanced in structures terminated at both ends with a low index layer, $Na_3AlF_6$, (Fig. 4.9). In this case, the transmission at 80° is as small as 0.03, corresponding to a reflection coefficient of 97%. The overall reflectivity can be enhanced in structures with larger number of layers.

## 4.4 Summary

In conclusion, the possibility to achieve a total omnidirectional reflection with one-dimensional periodic dielectric structures was demonstrated in this chapter. The origin of the total omnidirectional reflection has been discussed. Optimization criteria to design totally reflecting omnidirectional mirror were presented. It was found that for

reasonable values of Bragg mirror parameters ($\delta n > 1.5, \delta n_0 > 1.5$) a relatively large omnidirectional total reflection band ($> 5\%$) may be obtain, making the fabrication of an omnidirectional dielectric Bragg mirror feasible. The experimental demonstration of the omnidirectional reflection from a Bragg mirror was presented in the optical range in a full agreement with theoretical prediction of the phenomenon.

Since the first prediction and demonstration of the omnidirectional reflection from a one-dimensional periodic medium in 1998 [1, 2, 3, 4], several further developments have been made. The idea of omnidirectional mirror has also obtained a favorable press coverage [8, 9, 10, 11] over last years. The total number of publication devoted to this subject exceeds one hundred and many new publications appear every year. To mention a few examples of the successful applications of this idea, an improved planar microcavity [12], optical fibers [13, 14, 15] and Fabry-Perot resonator [16] can be cited.

# Bibliography


[1] Y. Fink, J. N. Winn, S. Fan, C. Chen, J. Michel, J. D. Joannopoulos, and E. L. Thomas, "A dielectric omnidirectional reflector," *Science* **282,** 1679–1682 (1998).

[2] D. N. Chigrin, A. V. Lavrinenko, D. A. Yarotsky, and S. V. Gaponenko, "Observation of total omnidirectional reflection from a one-dimensional dielectric lattice," *Appl. Phys. A: Materials Science and Processing* **68,** 25–28 (1999).

[3] P. St. J. Russell, S. Tredwell, and P. J. Roberts, "Full photonic bandgaps and spontaneous emission control in 1d multilayer dielectric structures," *Opt. Commun.* **160,** 66–71 (1999).

[4] D. N. Chigrin, A. V. Lavrinenko, D. A. Yarotsky, and S. V. Gaponenko, "All-dielectric one-dimensional periodic structures for total omnidirectional reflection and partial spontaneous emission control," *J. Lightwave Technol.* **17,** 2018–2024 (1999).

[5] P. Yeh, *Optical Waves in Layered Media* (John Wiley and Sons, New York, 1988).

[6] P. St. J. Russell, T. A. Birks, and F. D. Lloyd-Lucas, "Photonic Bloch waves and photonic band gaps," in *Confined electron and Photon: New physics and Applications*, E Burstein and C Weisbuch, eds., (Plenum Press, New York, 1995), pp. 585–633.

[7] M. Born and E. Wolf, *Principles of Optics* (Pergamon, New York, 1980).

[8] J. P. Dowling, "Mirror on the Wall: You're Omnidirectional After All?," *Science* **282,** 1841–1842 (1998).

[9] B. Schecter, "MIT Scientists Turn Simple Idea Into 'Perfect Mirror'," *New York Times* (December 15, 1998).

[10] S. Bains, "Photonic lattices stitch together new class of reflectors," *EE-Times* **1062,** 59–60 (May 24, 1999).

[11] R. Gaughan, "Visible light reflects nearly perfectly," *Photonics Spectra,* pp. 34–38 (July, 1999).

[12] J. A. E. Wasey and W. L. Barnes, "Efficiency of spontaneous emission from planar microcavities," *J. Mod. Optics* **47,** 725–741 (2000).

[13] Y. Fink, D. J. Ripin, S. Fan, Chen. C., J. D. Joannopoulos, and E. L. Thomas, "Guiding optical light in air using an all-dielectric structure," *J. Lightwave Technol.* **17,** 2039–2041 (1999).

[14] M. Ibanescu, Y. Fink, S. Fan, E. L. Thomas, and J. D. Joannopoulos, "An all-dielectric coaxial waveguide," *Science* **289,** 415–419 (2000).

[15] B. Temelkuran, S. D. Hart, G. Benoit, J. D. Joannopoulos, and Y. Fink, "Wavelength-scalable hollow optical fibres with large photonic bandgaps for CO2 laser transmission," *Nature* **420,** 650–653 (2002).

[16] I. Abdulhalim, "Reflective polarization conversion Fabry-Perot resonator using omnidirectional mirror of periodic anisotropic stack," *Opt. Commun.* **215,** 225–230 (2003).

# Part III

# Emission

# Chapter 5

# Radiation pattern of a classical dipole in a photonic crystal: photon focusing[1]

As it was shown in chapter 3, a photonic crystal can be a promising artificial material to control the spontaneous emission. Being able to modify in purpose the emission rate within a specific spectral range and simultaneously in specific directions could add a significant flexibility in improving light sources. In this chapter, questions like modification of the emission rate in a specific direction and modification of the emission pattern due to the photonic crystal environment are considered.

Special opportunities in controlling directionality of emission exist within spectral ranges of allowed photonic bands, where photonic crystals display strong dispersion and anisotropy. The consequence of anisotropy is *photon focusing* phenomenon [1, 2]. Photon focusing is similar to phonon focusing, a phenomenon observed in the ballistic transport of phonons in crystalline solid [3]. The term phonon focusing refers to the strong anisotropy of heat flux in crystalline solid. First observed in 1969 by Taylor *et. al.* [4], phonon focusing is a property of all crystals at low temperatures. The term "focusing" does not imply a bending of particle paths, as in the geometrical-optics sense of the term. The physical reason of the phonon focusing is the beam steering. In particular, waves with significantly different wave vectors can have nearly the same group velocity, so the energy flux associated with those waves bunches along certain crystalline directions. In some special cases, a heat flux can display intricate focusing caustics, along which flux tends to infinity [3]. This happens than the direction of

[1]This chapter is based on: D. N. Chigrin, "Radiation pattern of a classical dipole in a photonic crystal: photon focusing," submitted to *Phys. Rev. E*

the group velocity is stationary with respect to a small variation of the wave vector. An optical cousin of the acoustic phenomenon opens a unique opportunity to design a caustics pattern in purpose, enhancing and suppressing emission in specific directions.

In this chapter a description of an angular distribution of radiated power of a classical dipole embedded in a photonic crystal is presented. In section 5.1 the evaluation of the asymptotic form of the radiated field is given in the radiation zone. In section 5.2, an angular distribution of radiated power is introduced. A modification of the radiation pattern is discussed in terms of photon focusing in section 5.3. Numerical examples of an angular distribution of emission power radiated from a point isotropic light source are presented in section 5.4 for the case of a two-dimensional square lattice photonic crystal of dielectric rods in air. Section 5.5 summarizes the main results of the chapter.

## 5.1 Asymptotic form of dipole field

To obtain the dipole field in the radiation zone, an asymptotic form of normal mode expansion (2.41)

$$\mathbf{A}(\mathbf{r}) = -i\frac{4\pi c\omega_0}{V}\sum_n \int_{BZ} d^3\mathbf{k}_n \frac{(\mathbf{a}^*_{n\mathbf{k}}(\mathbf{r}_0)\cdot\mathbf{d})}{(\omega^2_{n\mathbf{k}} - \omega_0^2 - i\gamma)}\mathbf{a}_{n\mathbf{k}}(\mathbf{r})e^{i\mathbf{k}_n\cdot(\mathbf{r}-\mathbf{r}_0)} \tag{5.1}$$

is evaluated and analyzed. Here the Bloch theorem, $\mathbf{A}_{n\mathbf{k}}(\mathbf{r}) = \mathbf{a}_{n\mathbf{k}}(\mathbf{r})e^{i\mathbf{k}_n\cdot\mathbf{r}}$, has been used. Further, an asymptotic analysis of the Green's function presented by Maradudin [5] for the phonon scattering problem is followed.

Using the integral representation (3.59) one can rewrite (5.1) as:

$$\mathbf{A}(\mathbf{r}) = \frac{4\pi c\omega_0}{V}\sum_n \int_{BZ} d^3\mathbf{k}_n \int_0^\infty d\tau \left(\mathbf{a}^*_{n\mathbf{k}}(\mathbf{r}_0)\cdot\mathbf{d}\right)\mathbf{a}_{n\mathbf{k}}(\mathbf{r})e^{iF_{n\mathbf{k}}(\tau)}, \tag{5.2}$$

where

$$F_{n\mathbf{k}}(\tau) = \mathbf{k}_n\cdot(\mathbf{r}-\mathbf{r}_0) - \tau(\omega^2_{n\mathbf{k}} - \omega_0^2) \tag{5.3}$$

and a limit $\gamma \to 0$ was taken.

In a typical experiment $|\mathbf{x}| = |\mathbf{r}-\mathbf{r}_0| \gg \lambda$, where $\lambda$ is the wavelength of the electromagnetic wave. For large $\mathbf{x}$ an exponential function in the integral (5.2) will oscillate very rapidly and one can use the method of stationary phase to evaluate the integral.

The principal contribution to the integral comes from the neighborhood of those points in $\tau$- and $\mathbf{k}$-space where the variation of $F_{n\mathbf{k}}(\tau)$ is the smallest. This means that one can set the gradient of the function $F_{n\mathbf{k}}(\tau)$ in $\mathbf{k}$-space equal to zero as well as the

derivative of the function with respect to $\tau$. This gives the conditions:

$$\frac{\partial F_{n\mathbf{k}}}{\partial \tau} = \omega_{n\mathbf{k}}^2 - \omega_0^2 = 0 \tag{5.4}$$

$$\nabla_{\mathbf{k}} F_{n\mathbf{k}} = \mathbf{x} - \tau \nabla_{\mathbf{k}} \omega_{n\mathbf{k}}^2 = 0. \tag{5.5}$$

Equations (5.4-5.5) determine the values of $\tau$ and $\mathbf{k}_n$ around which the principal contributions to the integral (5.2) arise. These points are called stationary points. Further, the stationary points are denoted by $\tau_\nu$ and $\mathbf{k}_n^\nu$. Assuming that value of the eigenvector $\mathbf{a}_{n\mathbf{k}}(\mathbf{r})$ is approximately constant $\mathbf{a}_{n\mathbf{k}}(\mathbf{r}) \approx \mathbf{a}_{n\mathbf{k}}^\nu(\mathbf{r})$ for $\tau$ close to $\tau_\nu$ and for the wave vectors close to $\mathbf{k}_n^\nu$, the integral (5.2) is reduced to the sum of the integrals in the vicinities of the stationary points $(\tau_\nu, \mathbf{k}_n^\nu)$ [5, 6]

$$\mathbf{A}(\mathbf{r}) \approx \frac{4\pi c\omega_0}{V} \sum_\nu \sum_n \left(\mathbf{a}_{n\mathbf{k}}^{\nu *}(\mathbf{r}_0) \cdot \mathbf{d}\right) \mathbf{a}_{n\mathbf{k}}^\nu(\mathbf{r}) \int_{\mathbf{k}_n^\nu} d^3\mathbf{k}_n \int_{\tau_\nu} d\tau e^{iF_{n\mathbf{k}}(\tau)}, \tag{5.6}$$

Here an extra summation is over all possible solutions of Eqs. (5.4-5.5).

Due to Eq. (5.4) the principal contribution to the asymptotic behavior of $\mathbf{A}(\mathbf{r})$ comes from the iso-frequency surface in $\mathbf{k}$-space defined by $\omega_{n\mathbf{k}}^2 = \omega_0^2$ or equivalently defined by $\omega_{n\mathbf{k}} = \omega_0$ (eigenfrequency $\omega_{n\mathbf{k}}$ is positive and real). At the same time, due to Eq. (5.5) the portion of the iso-frequency surface, $\omega_{n\mathbf{k}} = \omega_0$, which contributes to the asymptotic field is the portion near the point on this surface where the gradient $\nabla_{\mathbf{k}}\omega_{n\mathbf{k}}^2$ is parallel to $\mathbf{x}$. One can express the latter condition in an alternative fashion. Equation (5.5) can be simplified as:

$$\mathbf{x} = 2\tau\omega_{n\mathbf{k}}\mathbf{V}_{n\mathbf{k}},$$

where $\mathbf{V}_{n\mathbf{k}} = \nabla_{\mathbf{k}}\omega_{n\mathbf{k}}$ is the group velocity of the eigenwave $(n, \mathbf{k})$. So, equation (5.5) just says that the principal contribution to the asymptotic behavior of the field $\mathbf{A}(\mathbf{r})$ at large $|\mathbf{x}| = |\mathbf{r} - \mathbf{r}_0| \gg \lambda$ comes from the neighborhood of the points $\mathbf{k}_n^\nu$ on the iso-frequency surface $\omega_{n\mathbf{k}} = \omega_0$ at which the eigenwave group velocity is parallel to observation direction $\mathbf{x}$. Since $\tau$ is positive by definition (3.59), $\mathbf{V}_{n\mathbf{k}}^\nu$ and $\mathbf{x}$ should not only be parallel, but should point in the same direction as well, $\mathbf{x} \cdot \mathbf{V}_{n\mathbf{k}}^\nu > 0$.

Assuming that the major contribution comes from the regions near the stationary points, a small error is made by extending the integration in (5.6) over all space

$$\mathbf{A}(\mathbf{r}) \approx \frac{4\pi c\omega_0}{V} \sum_\nu \sum_n \left(\mathbf{a}_{n\mathbf{k}}^{\nu *}(\mathbf{r}_0) \cdot \mathbf{d}\right) \mathbf{a}_{n\mathbf{k}}^\nu(\mathbf{r}) \int_{-\infty}^{\infty} d^3\mathbf{k}_n \int_{-\infty}^{\infty} d\tau e^{iF_{n\mathbf{k}}(\tau)}. \tag{5.7}$$

Then, the integral over $\tau$ is simply given by Dirac $\delta$-function:

$$\int_{-\infty}^{\infty} d\tau e^{i\tau(\omega_0^2-\omega_{n\mathbf{k}}^2)} = 2\pi\delta(\omega_0^2-\omega_{n\mathbf{k}}^2)$$

and one can further convert the volume integration in $\mathbf{k}$-space to an integral over the iso-frequency surface $\omega_{n\mathbf{k}} = \omega_0$. In fact, by using the relations $|\nabla_{\mathbf{k}}\omega_{n\mathbf{k}}|\, dk = d\omega_{n\mathbf{k}}$ and $d^3\mathbf{k} = dkd^2\mathbf{k}$, and integrating over the eigenfrequency $\omega_{n\mathbf{k}}$, the volume integration over $\mathbf{k}$ transforms to:

$$\int_{-\infty}^{\infty} d^3\mathbf{k}_n e^{i\mathbf{k}_n\cdot(\mathbf{r}-\mathbf{r}_0)}\delta(\omega_0^2-\omega_{n\mathbf{k}}^2) = \oint_{-\infty}^{\infty} d^2\mathbf{k}_n \frac{\pi}{\omega_0}\frac{e^{i\mathbf{k}_n\cdot(\mathbf{r}-\mathbf{r}_0)}}{|\mathbf{V}_{n\mathbf{k}}|}.$$

So, the asymptotic form of the field $\mathbf{A}(\mathbf{r})$ is finally given by:

$$\mathbf{A}(\mathbf{r}) \approx \frac{4\pi^2 c}{V}\sum_{\nu}\sum_{n}\frac{(\mathbf{a}_{n\mathbf{k}}^{\nu *}(\mathbf{r}_0)\cdot\mathbf{d})\,\mathbf{a}_{n\mathbf{k}}^{\nu}(\mathbf{r})}{|\mathbf{V}_{n\mathbf{k}}^{\nu}|}\oint_{-\infty}^{\infty} d^2\mathbf{k}_n e^{i\mathbf{k}_n\cdot(\mathbf{r}-\mathbf{r}_0)}, \tag{5.8}$$

where the comparatively slow varying function $\mathbf{V}_{n\mathbf{k}}$ was replaced by its value at stationary point $\mathbf{k}_n^{\nu}$ and was taken outside the integral over $\mathbf{k}$.

To evaluate the integrals in the Eq. (5.8) an analysis of the form of the iso-frequency surface in the vicinity of one of the stationary points, $\mathbf{k}_n^{\nu}$, should be done. It is convenient to introduce the local curvilinear coordinates $\xi_i$ with the origin at the stationary point and with one of the coordinate aligned perpendicular to the iso-frequency surface, e.g., $\xi_3$. One can expand the function $h(\xi_1,\xi_2) = \mathbf{k}_n\cdot\widehat{\mathbf{x}}$ near the stationary point as:

$$h(\xi_1,\xi_2) = \mathbf{k}_n^{\nu}\cdot\widehat{\mathbf{x}} + \frac{1}{2}\sum_{i,j=1}^{2}\alpha_{ij}^{\nu}\xi_i\xi_j + \frac{1}{6}\sum_{i,j,k=1}^{2}\beta_{ijk}^{\nu}\xi_i\xi_j\xi_k + O(\xi_1,\xi_2)^4, \tag{5.9}$$

where

$$\alpha_{ij}^{\nu} = \left(\frac{\partial^2 h}{\partial\xi_i\partial\xi_j}\right)_{\nu}, \qquad \beta_{ijk}^{\nu} = \left(\frac{\partial^3 h}{\partial\xi_i\partial\xi_j\partial\xi_k}\right)_{\nu}$$

and $\widehat{\mathbf{x}}$ is a unit vector in the observation direction. All derivatives are evaluated at the stationary point $\mathbf{k}_n^{\nu}$.

The result of the integration in (5.8) depends on the local topology of the iso-frequency surface near the stationary point. One can generally classify the local topology of the surface by its Gaussian curvature [7]. The Gaussian curvature $K$ is the product of the two principal curvatures (inverse radii, $K_1$ and $K_2$) at a point on the surface, i.e., $K = K_1K_2$. The points on an iso-frequency surface can be elliptical, hyperbolic and parabolic. If the Gaussian curvature $K > 0$, the corresponding point on the iso-frequency surface is called elliptical, and if $K < 0$ it is called hyperbolic. For a complex surface, such as the iso-frequency surface in Fig. 5.1, the regions with positive

and negative Gaussian curvature alternate. The surface is parabolic at the borders between regions with curvatures of opposite signs, e.g, convex and saddle. The lines along which the curvature changes its sign are called parabolic lines. The Gaussian curvature at a parabolic point is equal to zero.

Further, an analysis of the asymptotic form of the integral (5.8) is undertaken, when the stationary points are elliptical or hyperbolic. Then in the close vicinity of such a stationary point the following expansion holds:

$$h\left(\xi_1,\xi_2\right)=\mathbf{k}_n^\nu\cdot\widehat{\mathbf{x}}+\frac{1}{2}\sum_{i,j=1}^{2}\alpha_{ij}^\nu\xi_i\xi_j, \tag{5.10}$$

where only quadratic terms in the expansion (5.9) were kept. By choosing the orientation of the local coordinate axes $\xi_1$ and $\xi_2$ along the main directions of the surface curvature at that point $\mathbf{k}_n=\mathbf{k}_n^\nu$, one can diagonalize the matrix $\alpha_{ij}^\nu$. Then:

$$h\left(\xi_1,\xi_2\right)=\mathbf{k}_n^\nu\cdot\widehat{\mathbf{x}}+\frac{1}{2}\left(\alpha_1^\nu\xi_1^2+\alpha_2^\nu\xi_2^2\right),\qquad\alpha_1^\nu=\alpha_{11}^\nu,\ \alpha_2^\nu=\alpha_{22}^\nu. \tag{5.11}$$

With such a choice of local coordinates in $\mathbf{k}$-space, the product $K_{n\mathbf{k}}^\nu=\alpha_1^\nu\alpha_2^\nu$ determines the Gaussian curvature of the iso-frequency surface at the stationary point $\mathbf{k}_n=\mathbf{k}_n^\nu$.

Using expansion (5.11) the asymptotic form of the field (5.8) is now given by:

$$\begin{aligned}\mathbf{A}(\mathbf{r}) &\approx \frac{4\pi^2c}{V}\sum_\nu\sum_n\frac{\left(\mathbf{a}_{n\mathbf{k}}^{\nu*}(\mathbf{r}_0)\cdot\mathbf{d}\right)\mathbf{a}_{n\mathbf{k}}^\nu(\mathbf{r})}{\left|\mathbf{V}_{n\mathbf{k}}^\nu\right|}e^{i\mathbf{k}_n^\nu\cdot\mathbf{x}}\\ &\times \oint_{-\infty}^{\infty}d\xi_1d\xi_2\exp\left(\frac{i\left|\mathbf{x}\right|}{2}\left(\alpha_1^\nu\xi_1^2+\alpha_2^\nu\xi_2^2\right)\right).\end{aligned} \tag{5.12}$$

The integral in Eq. (5.12) is calculated simply to be:

$$\int_{-\infty}^{\infty}d\xi\exp\left(i\frac{x\alpha}{2}\xi^2\right)=\sqrt{\frac{2\pi}{x\left|\alpha\right|}}\exp\left(-\frac{i\pi}{4}\mathrm{sign}\left(\alpha\right)\right) \tag{5.13}$$

and an asymptotic form of the vector potential (5.1) at the position $\mathbf{r}$ far from the dipole is given by

$$\begin{aligned}\mathbf{A}(\mathbf{r},t) &\approx \sum_\nu\sum_n\exp\left(-i\left(\omega_0t+\frac{\pi}{4}\left(\mathrm{sign}(\alpha_1^\nu)+\mathrm{sign}(\alpha_2^\nu)\right)\right)\right)\\ &\times \frac{c}{V}\frac{\left(\mathbf{A}_{n\mathbf{k}}^{\nu*}(\mathbf{r}_0)\cdot\mathbf{d}\right)\mathbf{A}_{n\mathbf{k}}^\nu(\mathbf{r})}{\left|\mathbf{V}_{n\mathbf{k}}^\nu\right|}\frac{8\pi^3}{\left|K_{n\mathbf{k}}^\nu\right|^{1/2}\left|\mathbf{r}-\mathbf{r}_0\right|},\end{aligned} \tag{5.14}$$

where $\mathbf{A}_{n\mathbf{k}}^\nu(\mathbf{r})=\mathbf{a}_{n\mathbf{k}}^\nu(\mathbf{r})e^{i\mathbf{k}_n^\nu\cdot\mathbf{r}}$ and summation is over all stationary points with $\mathbf{x}\cdot\mathbf{V}_{n\mathbf{k}}^\nu>0$.

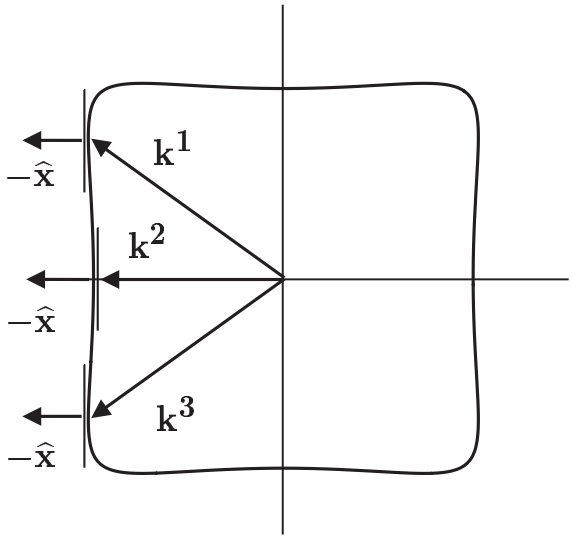


Figure 5.1: The central region of the iso-frequency contour for normalized frequency $\Omega = \omega d/2\pi c = d/\lambda = 0.569$ of the infinite square lattice 2D photonic crystal made out of dielectric rods placed in vacuum. Rods have the optical index 2.9 and radius $r = 0.15d$, where $d$ is the period of the lattice (see Sec. 5.4 for details). The stationary points, $\mathbf{k}^1$, $\mathbf{k}^2$ and $\mathbf{k}^3$, corresponding to the same observation direction $\widehat{\mathbf{x}}$ are indicated.

According to the Eq. (5.14) the electromagnetic field inside a photonic crystal represents a superposition of several diverging waves, the number of which equals the number of stationary phase points on the iso-frequency surface $\omega_{n\mathbf{k}} = \omega_0$ (Fig. 5.1). Each of these waves has its own shape and its own propagation velocity. One comment is important here, the asymptotic expansion (5.14) describes an outgoing wave ($\mathbf{k}_n^\nu \cdot \mathbf{x} > 0$) only if the corresponding group velocity is an outward normal to the iso-frequency surface $\omega_{n\mathbf{k}} = \omega_0$ at point $\mathbf{k}_n^\nu$. It can happen, however, that the group velocity becomes an inward normal for some frequencies and regions of $\mathbf{k}$-space (Fig. 5.1). In such a case the dot product $\mathbf{k}_n^\nu \cdot \mathbf{x}$ is not positive in the asymptotic expansion (5.14) and the expansion describes incoming waves. In such a situation, one should change a sign of the small imaginary part $\gamma$ in regularized equation (5.1) [5]:

$$\mathbf{A}(\mathbf{r}) = -i\frac{4\pi c\omega_0}{V}\sum_n \int_{BZ} d^3\mathbf{k}_n \frac{(\mathbf{a}^*_{n\mathbf{k}}(\mathbf{r}_0)\cdot\mathbf{d})}{(\omega^2_{n\mathbf{k}} - \omega_0^2 + i\gamma)}\mathbf{a}_{n\mathbf{k}}(\mathbf{r})e^{i\mathbf{k}_n\cdot(\mathbf{r}-\mathbf{r}_0)} \tag{5.15}$$

and proceed as it has been describe above (5.2-5.14), but using the integral representation

$$\frac{1}{x+i\gamma} = \frac{1}{i}\int_0^\infty d\tau e^{ix\tau-\gamma\tau} \tag{5.16}$$

instead of (3.59).

## 5.2 Angular distribution of radiated power

Using the definition of the solid angle, $d\Omega_{n\mathbf{k}} = d^2\mathbf{k}\cos\varphi/\left|\mathbf{k}_n\right|^2$, where $d\Omega_{n\mathbf{k}}$ is the solid angle subtended by the surface element $d^2\mathbf{k}_n$, $\varphi$ is the angle between the wave vector $\mathbf{k}_n$ and the group velocity $\mathbf{V}_{n\mathbf{k}} = \nabla_{\mathbf{k}}\omega_{n\mathbf{k}}$ (Fig. 5.2), on changing the integration variables, one can modify the equation for the total radiated power (3.62) to the form:

$$P = \sum_n \int_0^{4\pi} d\Omega_{n\mathbf{k}} \left( \frac{\pi^2\omega_0^2}{V} \frac{\left|\mathbf{A}_{n\mathbf{k}}(\mathbf{r}_0)\cdot\mathbf{d}\right|^2}{\left|\mathbf{V}_{n\mathbf{k}}\right|} \frac{\left|\mathbf{k}_n\right|^2}{\cos\varphi} \right), \tag{5.17}$$

where the function enclosed in the brackets basically defines the radiated power of the dipole per solid angle in $\mathbf{k}$-space

$$\frac{dP}{d\Omega_{n\mathbf{k}}} = \frac{\pi^2\omega_0^2}{V} \frac{\left|\mathbf{A}_{n\mathbf{k}}(\mathbf{r}_0)\cdot\mathbf{d}\right|^2}{\left|\mathbf{V}_{n\mathbf{k}}\right|} \frac{\left|\mathbf{k}_n\right|^2}{\cos\varphi}. \tag{5.18}$$

To derive an angular distribution of radiated power in coordinate space, one should change the integration variables in (5.17) from $\mathbf{k}$-space to coordinate space.

The $\mathbf{k}$-space distribution of radiated power (5.18) is a function of a $\mathbf{k}$-space direction, given by the polar, $\theta_{n\mathbf{k}}$, and azimuthal, $\phi_{n\mathbf{k}}$, angles of the wave vector $\mathbf{k}_n$. The direction of energy propagation in a non-absorbing periodic medium coincides with the group velocity direction [8]. Whereas the angular dependence of the radiated power in coordinate space is given by the corresponding group velocity direction in coordinate space $(\theta, \phi)$. Here $\theta$ and $\phi$ are the polar and azimuthal angles of the group velocity in coordinate space. The $\mathbf{k}$-space to coordinate space transformation may be expressed formally as:

$$\cos\theta = f(\cos\theta_{n\mathbf{k}}, \phi_{n\mathbf{k}}), \tag{5.19}$$

$$\phi = g(\cos\theta_{n\mathbf{k}}, \phi_{n\mathbf{k}}), \tag{5.20}$$

where the functions $f$ and $g$ are determined from the components of the group velocity vector $\mathbf{V}^{\nu}_{n\mathbf{k}} \parallel \widehat{\mathbf{x}}$, where $\widehat{\mathbf{x}}$ is the unit vector in the observation direction. The Jacobian of the transformation (5.19-5.20):

$$J_{n\mathbf{k}} = \frac{\partial f}{\partial\cos\theta_{n\mathbf{k}}}\frac{\partial g}{\partial\phi_{n\mathbf{k}}} - \frac{\partial f}{\partial\phi_{n\mathbf{k}}}\frac{\partial g}{\partial\cos\theta_{n\mathbf{k}}} \tag{5.21}$$

relates a small solid angle in coordinate space with a corresponding solid angle in $\mathbf{k}$-space via:

$$d\Omega = d(\cos\theta)d\phi = J_{n\mathbf{k}}d(\cos\theta_{n\mathbf{k}})d\phi_{n\mathbf{k}} = J_{n\mathbf{k}}d\Omega_{n\mathbf{k}}. \tag{5.22}$$

According to the result presented in the Section 5.1, different wave vectors can result

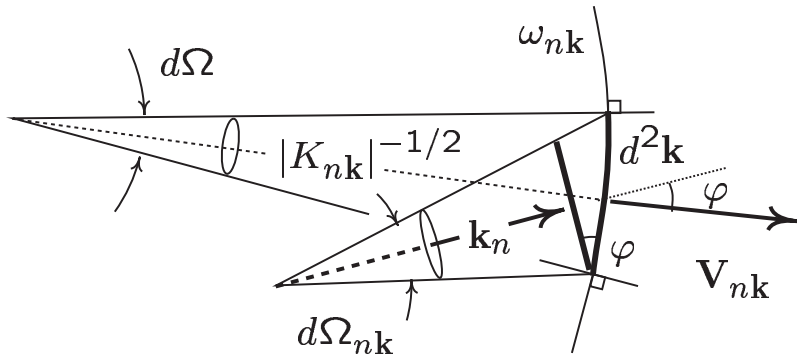


Figure 5.2: Diagram to derive the relation between solid angles in the **k**-space and coordinate space. An iso-frequency contour for frequency $\omega_{n\mathbf{k}}$ is presented. The Jacobian of the transformation (5.19-5.20) is given by the ratio $d\Omega/d\Omega_{n\mathbf{k}}$. By the definition of the solid angle, a solid angle in **k**-space is $d\Omega_{n\mathbf{k}} = d^2\mathbf{k}\cos\varphi/\left|\mathbf{k}_n\right|^2$, while a corresponding solid angle in coordinate space is $d\Omega = d^2\mathbf{k}\,|K_{n\mathbf{k}}|$. That gives a Jacobian $J_{n\mathbf{k}} = \left|\mathbf{k}_n\right|^2 |K_{n\mathbf{k}}| / \cos\varphi$. Here $\varphi$ is an angle between the wave vector and the group velocity vector. $d^2\mathbf{k}$ is a surface element of the iso-frequency surface.

in the group velocity with same direction in coordinate space. That means that the following equation:

$$d\Omega^{\nu}_{n\mathbf{k}} = \frac{1}{J^{\nu}_{n\mathbf{k}}} d\Omega$$

should hold for each stationary wave vector, which satisfies $\widehat{\mathbf{x}} \cdot \mathbf{V}^{\nu}_{n\mathbf{k}} > 0$. Changing the integration variables in (5.17) one should then sum individual contributions from all these wave vectors:

$$P = \sum_n \sum_{\nu} \int_0^{4\pi} \frac{1}{J^{\nu}_{n\mathbf{k}}} d\Omega \left( \frac{\pi^2 \omega_0^2}{V} \frac{\left|\mathbf{A}^{\nu}{}_{n\mathbf{k}}(\mathbf{r}_0) \cdot \mathbf{d}\right|^2}{|\mathbf{V}^{\nu}_{n\mathbf{k}}|} \frac{|\mathbf{k}^{\nu}_n|^2}{\cos\varphi} \right), \tag{5.23}$$

The geometrical relationship between solid angles in **k**-space and coordinate space (Fig. 5.2) results in the following formula for the Jacobian (5.21)

$$J^{\nu}_{n\mathbf{k}} = \left|\mathbf{k}^{\nu}_n\right|^2 |K^{\nu}_{n\mathbf{k}}| / \cos\varphi.$$

Then, equation (5.23) can be transformed to the form:

$$P = \int_0^{4\pi} d\Omega \left( \sum_n \sum_{\nu} \frac{\pi^2 \omega_0^2}{V} \frac{\left|\mathbf{A}^{\nu}_{n\mathbf{k}}(\mathbf{r}_0) \cdot \mathbf{d}\right|^2}{|\mathbf{V}^{\nu}_{n\mathbf{k}}|\,|K^{\nu}_{n\mathbf{k}}|} \right), \tag{5.24}$$

where $\mathbf{V}^{\nu}_{n\mathbf{k}} = \nabla_{\mathbf{k}}\omega_{n\mathbf{k}}$ is the group velocity and $K^{\nu}_{n\mathbf{k}}$ determines the Gaussian curvature of the iso-frequency surface at the stationary point $\mathbf{k}_n = \mathbf{k}^{\nu}_n$. Finally, the radiated power of the dipole per solid angle in coordinate space is given by the function enclosed in

the brackets in (5.24)

$$\frac{dP}{d\Omega} = \sum_n \sum_\nu \frac{\pi^2 \omega_0^2}{V} \frac{\left|\mathbf{A}^\nu_{n\mathbf{k}}(\mathbf{r}_0) \cdot \mathbf{d}\right|^2}{\left|\mathbf{V}^\nu_{n\mathbf{k}}\right| \left|K^\nu_{n\mathbf{k}}\right|}. \tag{5.25}$$

Formula (5.25) provides a simple route to calculate the angular distribution of radiated power of a point dipole (2.38) inside a photonic crystal. It can be interpreted as a decay rate, at which a dipole transfers energy to the electromagnetic waves with the group velocity in the observation direction. Then, $(d\Gamma/d\Omega) = (dP/d\Omega)/\hbar\omega_0$ is related to the probability of the radiative transition of an excited atom emitting a photon traveling in the given direction of observation.

Basically, formulae (5.24-5.25) involve calculations of the Bloch wave vectors $\mathbf{k}^\nu_n$, ending at the iso-frequency surface $\omega_{n\mathbf{k}} = \omega_0$, the corresponding group velocity vectors $\mathbf{V}^\nu_{n\mathbf{k}}$, the Gaussian curvature of the iso-frequency surface $K^\nu_{n\mathbf{k}}$ and the local coupling strength of the dipole moment with a Bloch eigenwave $(n, \mathbf{k})$, given by the factor $|\mathbf{A}^\nu_{n\mathbf{k}}(\mathbf{r}_0) \cdot \mathbf{d}|$. The primary difficulty in obtaining the coordinate space distribution of radiated power $(dP/d\Omega)$ (5.25) is that the wave vector, the group velocity and the Gaussian curvature are all functions of a $\mathbf{k}$-space direction, whereas, the angular dependence of the radiative power $(dP/d\Omega)$ is given by the corresponding group velocity direction $(\theta, \phi)$. To calculate a radiated power $(dP/d\Omega)$ (5.25) one should take an inverse of the mapping (5.19-5.20). However, this inverse is not necessarily unique. In the case of multiple stationary points (5.4-5.5), one direction $(\theta, \phi)$ results from several different $\mathbf{k}$-space directions $(\theta_\mathbf{k}, \phi_\mathbf{k})$ (Fig. 5.1). This requires that the inversion of the mapping (5.19-5.20) must be done point-by-point.

As a simple exercise, formula (5.25) is applied here to calculate the angular distribution of power radiated by a dipole in free space. The wave vector and the group velocity in free space are parallel and their values are simply given by $|\mathbf{k}| = \omega_0/c$ and $c$, respectively. The Gaussian curvature of the iso-frequency surface is a square of the inverse wave vector $1/\left|\mathbf{k}\right|^2$ and the appropriate normal modes are plane waves:

$$\mathbf{A}_{n\mathbf{k}}(\mathbf{r}) = \sqrt{\frac{V}{(2\pi)^3}} e^{i\mathbf{k}\cdot\mathbf{r}} \widehat{\mathbf{a}}_{n\mathbf{k}},$$

where $\widehat{\mathbf{a}}_{n\mathbf{k}}$ is a polarization vector orthogonal to the wave vector $\mathbf{k}$. Then, the radiated power is given by (5.25):

$$\left(\frac{dP}{d\Omega}\right)_{free} = \frac{1}{8\pi} \frac{\omega_0^4}{c^3} \left|\mathbf{d}\right|^2 \sin^2\theta \tag{5.26}$$

yielding the usual results for radiation pattern in free space [9].

## 5.3 Photon focusing

The factor $|\mathbf{A}^{\nu}_{n\mathbf{k}}(\mathbf{r}_0)\cdot\mathbf{d}|^2$ in relation (5.25), giving the coupling strength of dipole moment with a photonic crystal eigenmode at the dipole position, can display a complex angular behavior, which depends on eigenmode structure and dipole orientation with respect to the crystal lattice. To study the net result of the influence of a photonic crystal on the radiation pattern of an emitter, it is instructive to model an isotropic light source producing a uniform distribution of wave vectors. Moreover, an isotropic point source is usually a good model for a common experimental situation of emitters with random distribution of dipole moments (dye molecules [10, 11, 12], quantum dots [10, 13], etc.). Then, the radiated power (5.25) should be averaged over the dipole moment orientation, which simply yields a factor of $|\mathbf{d}|^2/3$:

$$\left(\frac{dP}{d\Omega}\right)_i = \sum_n \sum_\nu \frac{(2\pi c)^3}{V\omega_0^2} \frac{|\mathbf{A}^{\nu}_{n\mathbf{k}}(\mathbf{r}_0)|^2}{|\mathbf{V}^{\nu}_{n\mathbf{k}}|\,|K^{\nu}_{n\mathbf{k}}|}. \tag{5.27}$$

Here the result was normalized to the radiated power in free space. Now, the factor $|\mathbf{A}^{\nu}_{n\mathbf{k}}(\mathbf{r}_0)|^2$ gives the field strength at the source position and has no angular dependence. Thus, the radiation pattern of a point isotropic emitter is defined by:

$$\left(\frac{dP}{d\Omega}\right)_i \sim \sum_n \sum_\nu |\mathbf{V}^{\nu}_{n\mathbf{k}}|^{-1}\,|K^{\nu}_{n\mathbf{k}}|^{-1}\,. \tag{5.28}$$

The radiated power (5.28) is proportional to the inverse group velocity, $|\mathbf{V}^{\nu}_{n\mathbf{k}}|^{-1}$, and to the inverse Gaussian curvature, $|K^{\nu}_{n\mathbf{k}}|^{-1}$ of iso-frequency surface (Sec. 5.2). A large enhancement of emission rate is expected when the group velocity is small. This can be interpreted as a consequence of the long interaction time of the emitter and the radiation field [14, 15, 16]. In a similar fashion, a small Gaussian curvature formally implies an enhancement of radiated power along a certain observation direction. While spontaneous emission enhancement due to a small group velocity involves non-linear interaction of radiation and emitter, an enhancement due to a small Gaussian curvature is a linear phenomenon related to the anisotropy of a photonic crystal and is a result of the beam steering effect. Being a measure of the rate, at which an emitter transfers energy in photons with a given group velocity, the radiated power (5.28) will be enhanced if many photons with different wave vectors reach the same detector. An enhancement of the radiated power, which is due to a small Gaussian curvature will be called *photon focusing* [1, 2] and has a major influence on the radiation pattern of a point source in a photonic crystal.

The physical picture of the *photon focusing* can be illustrated in the following manner (Fig. 5.3). An iso-frequency surface of an isotropic and homogeneous medium

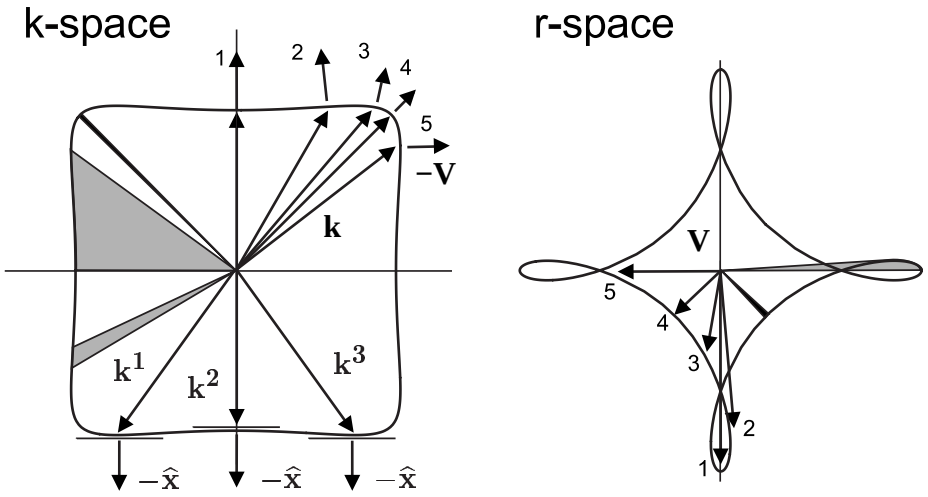


Figure 5.3: Iso-frequency and wave contours. Left: The central region of the iso-frequency contour for normalized frequency $\Omega = \omega d/2\pi c = d/\lambda = 0.569$ of the infinite square lattice 2D photonic crystal made out of dielectric rods placed in vacuum. Rods have the optical index 2.9 and radius $r = 0.15d$, where $d$ is the period of the lattice (see Sec. 5.4 for details). The stationary points, $\mathbf{k}^1$, $\mathbf{k}^2$ and $\mathbf{k}^3$, corresponding to the same observation direction $\widehat{\mathbf{x}}$ are indicated. Right: Corresponding wave contour with folds. The shaded and black regions show how two equal solid angle sections in coordinate space (right) map to widely varying solid angle sections in $\mathbf{k}$-space (left). The wave and group velocity vectors with numbers illustrate the folds formation of the wave contour.

is a sphere. There is only one stationary point with $\widehat{\mathbf{x}} \cdot \mathbf{V}^{\nu}_{n\mathbf{k}} > 0$ and thus only one wave propagating in the given direction. Figure 5.3-left is an example of a part of the actual iso-frequency contour of a two-dimensional photonic crystal made out of dielectric rods placed in vacuum (see Sec. 5.4 for further details). The anisotropy of the crystal implies a complex non-spherical iso-frequency surface, which can have several stationary points with $\widehat{\mathbf{x}} \cdot \mathbf{V}^{\nu}_{n\mathbf{k}} > 0$ (Fig. 5.3-left). Several waves can propagate in a given direction inside a photonic crystal. It is illustrative to construct the *wave surface* in coordinate space. To construct the wave surface one should plot a ray in the observation direction $\widehat{\mathbf{x}}$ starting from the point source position and having the length of the group velocity $|\mathbf{V}^{\nu}_{n\mathbf{k}}|$. An example of the wave contour is presented in figure 5.3-right. The existence of multiple stationary point implies that the wave surface is a complex multivalued surface parameterized by wave vector $\mathbf{k}_n$. Figure 5.3 illustrates how this can result in a fold of the wave surface.

In the vicinity of the parabolic point with zero Gaussian curvature an iso-frequency surface is flat. That implies, that a very large number of eigenwaves with wave vectors in the vicinity of a parabolic point have nearly the same group velocity, contributing to the energy flux in the direction parallel to that group velocity. In the figure 5.3, it is illustrated this by mapping two equal solid angle sections along different obser-

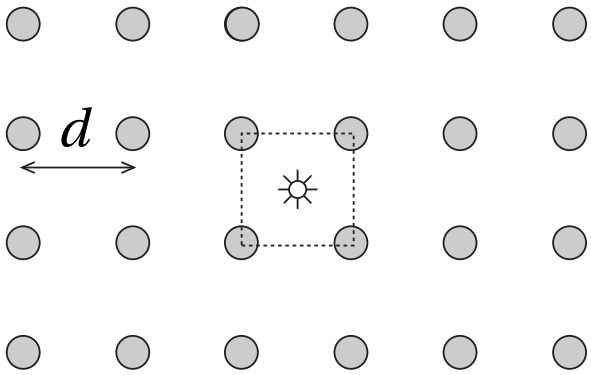


Figure 5.4: A two-dimensional photonic crystal: square lattice of dielectric rods in vacuum, with lattice constant $d$ and radius $0.15d$. The point light source is situated inside the crystal. The square represents a unit cell of the lattice.

vation direction in the coordinate space onto the corresponding solid angle sections in **k**-space [17]. The black solid angle section in coordinate space maps onto a single smaller solid angle section in **k**-space implying a "defocusing" of the energy flux. The shaded solid angle section in coordinate space, which crosses three different branches of the wave contour, maps onto two different and larger solid angle sections in **k**-space implying enhancement ("focusing") of the energy flux in this group velocity direction. This results in strongly varying angular distribution of emission intensity with sharp singularities (caustics).

## 5.4 Numerical example

In this section theoretical approach developed in previous sections is applied to numerical calculations of the radiation pattern of a point source placed inside a two-dimensional photonic crystal. A point source is placed in the crystal and it produces an isotropic and uniform distribution of wave vectors $\mathbf{k}_n$ with the frequency $\omega_0$.

An infinite two-dimensional square lattice of dielectric rods in vacuum (Fig. 5.4) is considered in the case of in-plane propagation of TM polarized light. The photonic band structure of the crystal made of rods with the refractive index $n = 2.9$ and radius $0.15d$ is presented in figure 5.5. Here $d$ is a period of the lattice. The refractive index is chosen close to that of alumina in the microwave region. In this case the separation between the center of rods along the lattice vectors should be on the order of a few centimeters.

In figure 5.6 iso-frequency contours of the two-dimensional square lattice photonic crystal (Fig. 5.4) are presented for two frequencies belonging to the first photonic band (Fig. 5.5). To plot an iso-frequency contour, the photonic band structure for all

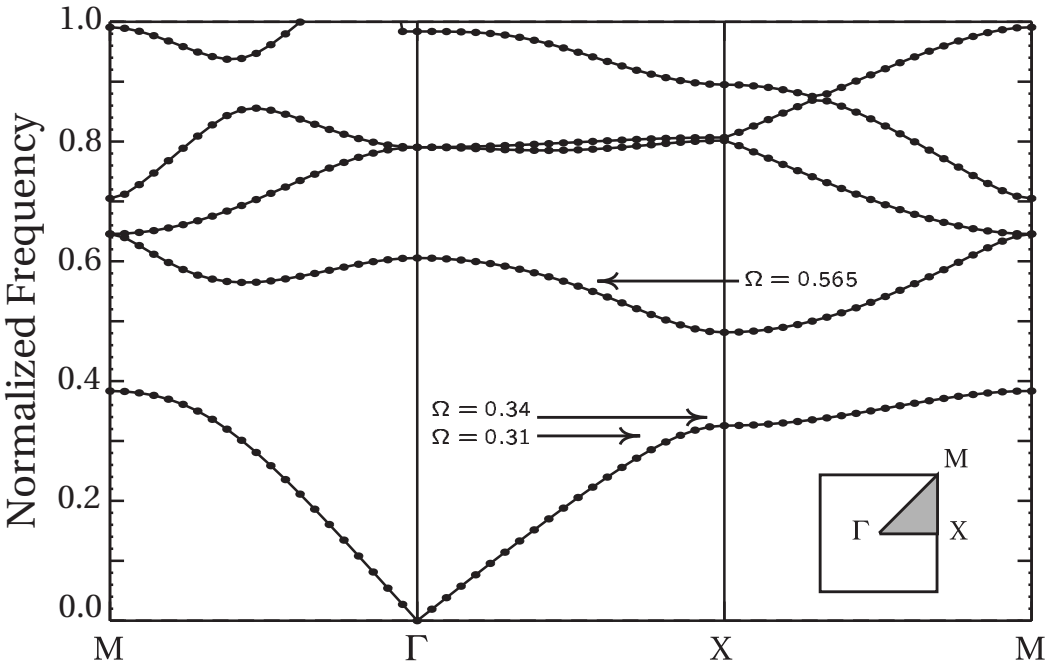


Figure 5.5: Photonic band structure of TM modes for the square lattice photonic crystal (Fig. 5.4) with refractive index of the rods $n = 2.9$. The frequency is normalized to $\Omega = \omega d/2\pi c = d/\lambda$. $c$ is the speed of light in vacuum. Inset shows the first Brillouin zone of the crystal with the irreducible zone shaded light gray.

wave vectors within the irreducible Brillouin zone was calculated and then an equation $\omega(\mathbf{k}) = \omega_0$ was solved for a given frequency $\omega_0$. Frequencies have been chosen below ($\Omega = 0.31$) and above ($\Omega = 0.34$) the low edge frequency of the stopband in the ΓX direction of the crystal (Fig. 5.5). The iso-frequency contours below and above the stopband edge frequency show an important difference.

As the frequency stays below the stopband, an iso-frequency contour is *closed* and almost circular (Fig. 5.6). The corresponding wave contour (see Section 5.3 for definition) is presented in the figure 5.7. The group velocity $|\mathbf{V}^{\nu}_{n\mathbf{k}}|$ and the Gaussian curvature $|K^{\nu}_{n\mathbf{k}}|$ of the iso-frequency contours are relatively slow functions of the wave vector. The Gaussian curvature does not vanish for any wave vector. This implies a small anisotropy in the energy flux inside the crystal (5.28).

To find how the radiated power varies in coordinate space, one should calculate the group velocity and the Gaussian curvature on the iso-frequency contour $\omega(\mathbf{k}) = \omega_0$ as functions of an angle in coordinate space. As the wave contour is a single-valued function, the inverse of the mapping (5.19-5.20) from $\mathbf{k}$-space to coordinate space is one-to-one and can be easily done. In figure 5.8 a polar plot of radiated power (5.28) is presented, which shows a small amount of anisotropy. The angular distribution of the radiated power possesses the four-fold rotational symmetry of the crystal.

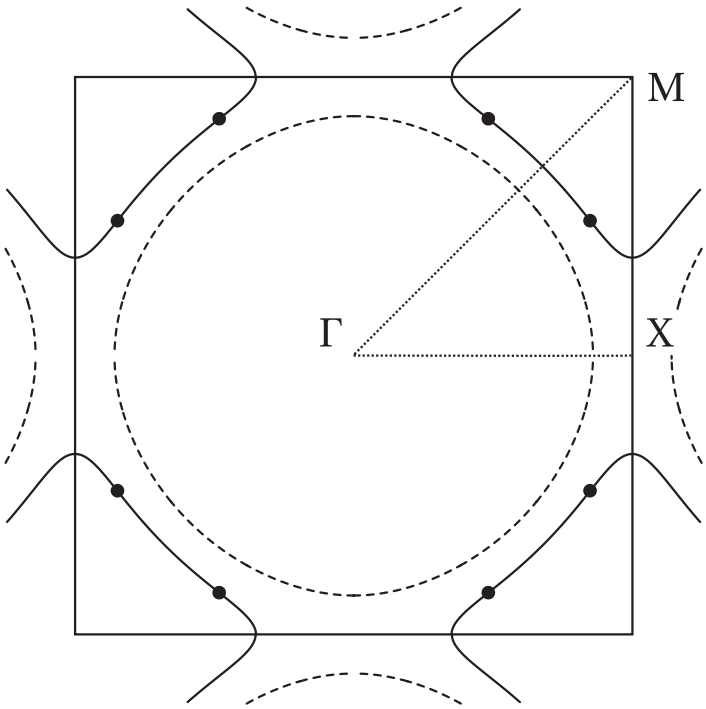


Figure 5.6: Iso-frequency contours of the square lattice photonic crystal (Fig. 5.4) for the normalized frequencies $\Omega = 0.31$ (dashed line) and $\Omega = 0.34$ (solid line). Parabolic points are marked by black dots. The first Brillouin zone of the lattice is plotted in order to show the spatial relation between zone boundary and iso-frequency contours.

Increasing the frequency up to the stopband, the topology of an iso-frequency contour changes abruptly. The stopband developed in the ΓX direction and the iso-frequency contour becomes *open* (Fig. 5.6). This topology changes result in a complex contour with alternating regions of Gaussian curvature with a different sign. Parabolic points, where the Gaussian curvature vanishes, are marked by black dots in the figure 5.6. As discussed in section 5.3, a vanishing curvature results in the folds of the wave contour. The wave contour corresponding to the iso-frequency $\Omega = 0.34$ is presented in figure 5.9. A pair of parabolic points in the first quarter of the Brillouin zone results in a cuspidal structure of the wave contours in the first quarter of the coordinate space. This dramatically increases anisotropy of the energy flux.

The folds in the wave contours yields that inverse of the mapping (5.19-5.20) from **k**-space to coordinate space is no longer one-to-one any more. To apply formula (5.28) to calculate an angular distribution of radiated power in such a case, one should proceed as follows. First, the Gaussian curvature as a function of the wave vector should be calculated. Then, wave vectors and group velocities corresponding to the parabolic points on the iso-frequency surface should be found. An inversion of the mapping (5.19-5.20) should be calculated separately for each of the branches of the wave contour. The total radiated power is the sum of the different contributions from these branches.

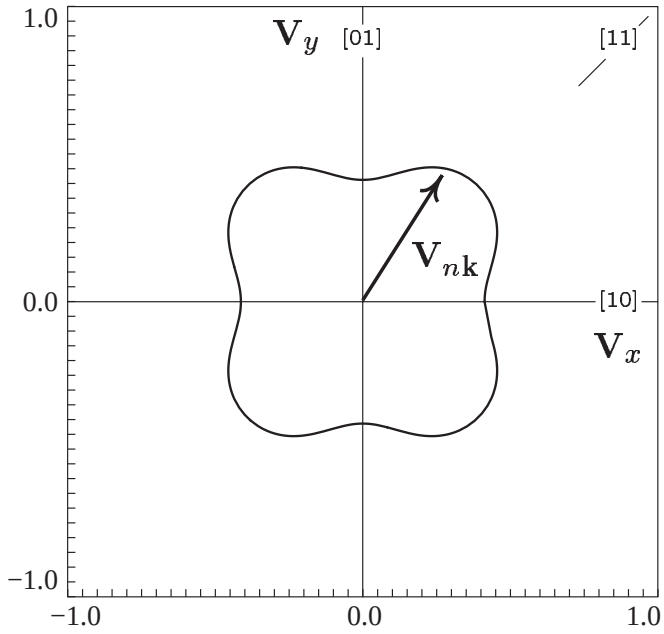


Figure 5.7: Wave contour corresponding to the normalized frequency $\Omega = 0.31$. The group velocity is plotted in units of the speed of light in vacuum. The symmetry directions of the square lattice are specified.

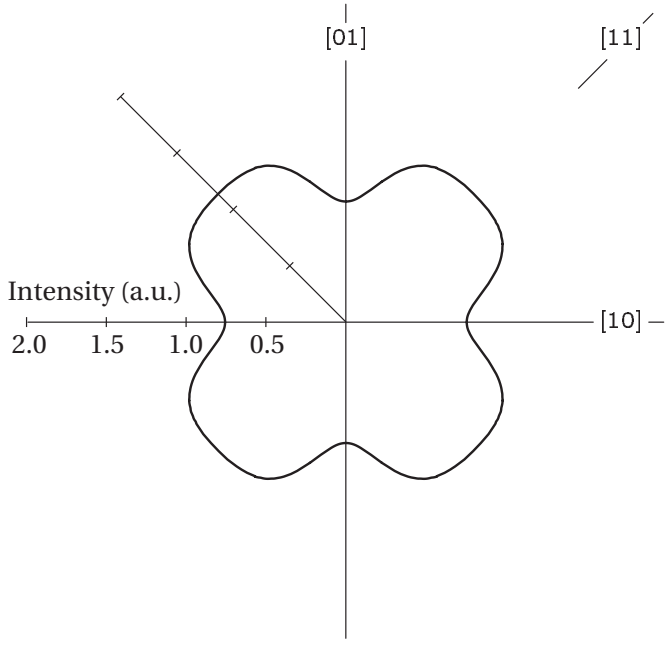


Figure 5.8: Angular distribution of radiative power corresponding to the normalized frequency $\Omega = 0.31$. High symmetry directions of the square lattice are specified.

In figure 5.10 a polar plot of radiated power (5.28) corresponding to the normalized frequency $\Omega = 0.34$ is presented. The energy flux is strongly anisotropic for this frequency, showing relatively small intensity in the directions of the stopband, and

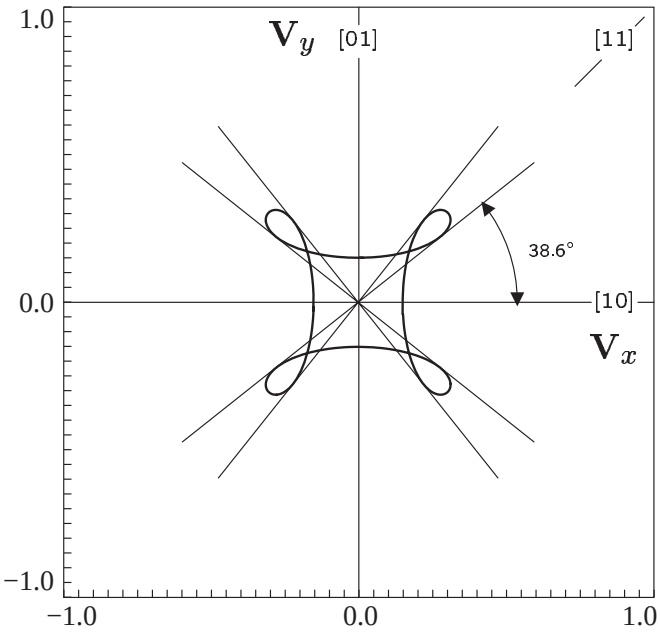


Figure 5.9: Wave contour corresponding to the normalized frequency $\Omega = 0.34$. The group velocity is plotted in the units of the speed of light in vacuum. The directions corresponding to the folds of the wave contour are shown.

infinite intensity (caustics) in the directions of the folds.

To substantiate this behavior, a finite difference time domain (FDTD) calculations was done [18, 19]. The simulated structure was a $50 \times 50$ lattice of rods in vacuum. The crystal is surrounded by an extra $5d$ wide layer of a free space. The simulation domain was discretized into squares with a side $\Delta = d/32$. The total simulation region was $1920 \times 1920$ cells plus 8-cell wide perfectly matched layer (PML) [20]. A point isotropic light source was modeled by a soft source [18, 19] with a homogeneous spatial dependence and sinusoidal temporal dependence of the signal. All FDTD calculations presented in this thesis were performed with a commercial tool [21].

In figure 5.11 a map of the modulus of the Poynting vector field is shown, when the crystal is excited by an isotropic point source at the normalized frequency $\Omega = 0.34$. The point source is placed in the middle of the crystal. A field map is shown for one instant time step. The snap-shots were captured after 10000 time steps, where the time step was $4.38 \times 10^{-17}$ s (0.99 of the Courant value). The structure of the crystal is superimposed on the field map. The highest values of the field are colored red, while the lowest are colored blue. From figure 5.11 one can see, that the emitted light is focused in the directions coinciding with the predicted directions of the folds (black lines in Fig. 5.11).

In figures 5.12-5.14, a more complicated example of the anisotropy of a photonic crystal is presented. Iso-frequency contours for three frequencies belonging to the

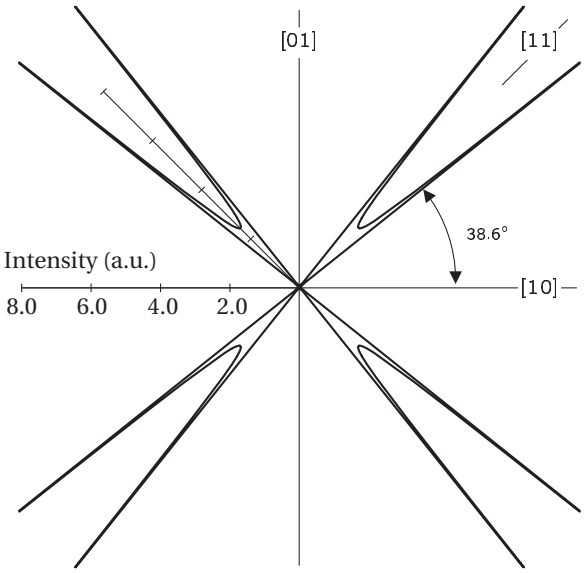


Figure 5.10: Angular distribution of radiative power corresponding to the normalized frequency $\Omega = 0.34$. The directions of infinite radiative power (caustic) coincide with the directions of the folds of the wave contour (Fig.5.9).

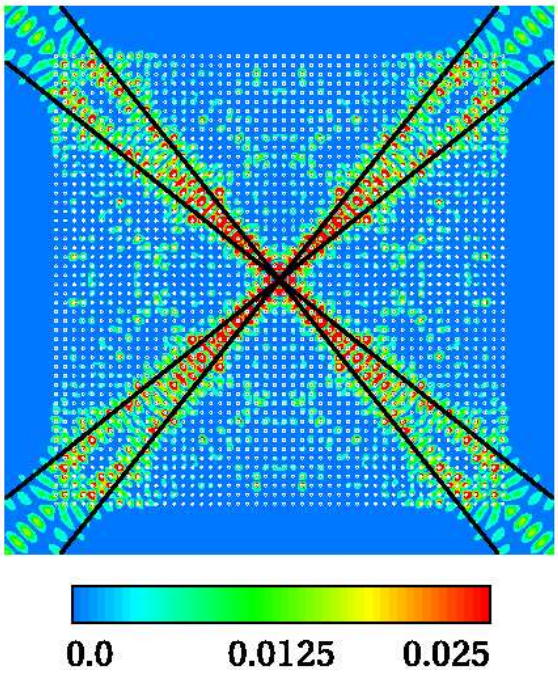


Figure 5.11: FDTD calculation. Map of the modulus of the Poynting vector field for a $50 \times 50$ rod photonic crystal excited by a isotropic point source at the normalized frequency $\Omega = 0.34$. The location of the crystal in the simulation is shown together with asymptotic directions of photon focusing caustics.

second photonic band of the crystal are plotted in the figure 5.12. While iso-frequency contours for the normalized frequencies $\Omega = 0.55$ and $\Omega = 0.58$ have non-vanishing

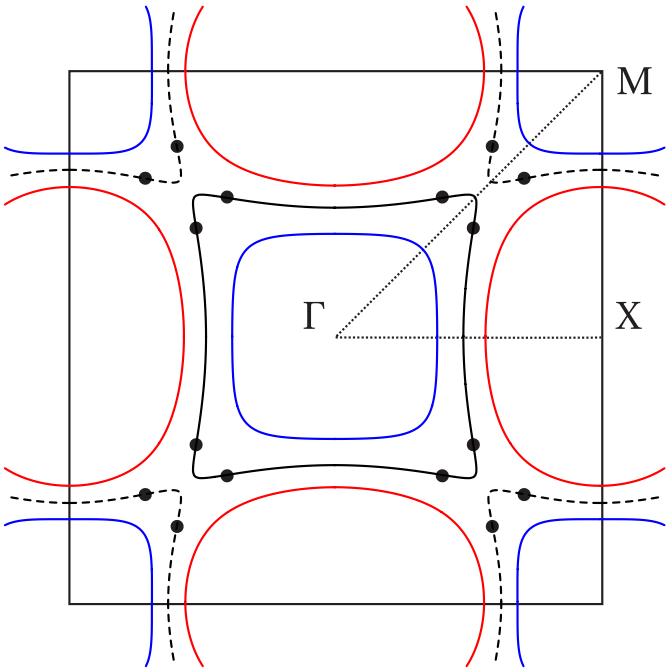


Figure 5.12: Iso-frequency contours of the square lattice photonic crystal (Fig.5.4) for the normalized frequencies $\Omega = 0.55$ (red line), $\Omega = 0.565$ (solid and dashed line) and $\Omega = 0.58$ (blue line). Two branches of the iso-frequency contour of $\Omega = 0.565$ are plotted as solid and dashed lines. Parabolic points are marked by black dots. The first Brillouin zone of the lattice is plotted in order to show the spatial relationship between zone boundary and iso-frequency contours.

Gaussian curvature for all wave vectors leading to only limited anisotropy of the energy flux, an iso-frequency contour for the normalized frequencies $\Omega = 0.565$ displays several parabolic points. More over the iso-frequency contour consists of two branched with slightly different shapes (solid and dashed lines in figure 5.12). Two branches yield two wave contours with cuspidal folds in coordinate space (Fig. 5.13). Applying the formula (5.28) to the radiative power calculation, one should sum over contributions coming from all branches of the wave contours in coordinate space. The angular distribution of the radiative power at the normalized frequency $\Omega = 0.565$ is presented in figure 5.14. Within the first quarter of the coordinate space, four caustics with infinite radiated power present in the energy flux corresponded to four parabolic points on two branches of the iso-frequency contours.

## 5.5 Summary

By analyzing a dipole field in the radiation zone it was shown, that the principal contribution to the far-field of the dipole radiating in a photonic crystal comes from regions of the iso-frequency surface in the wave vector space, where the eigenwave group

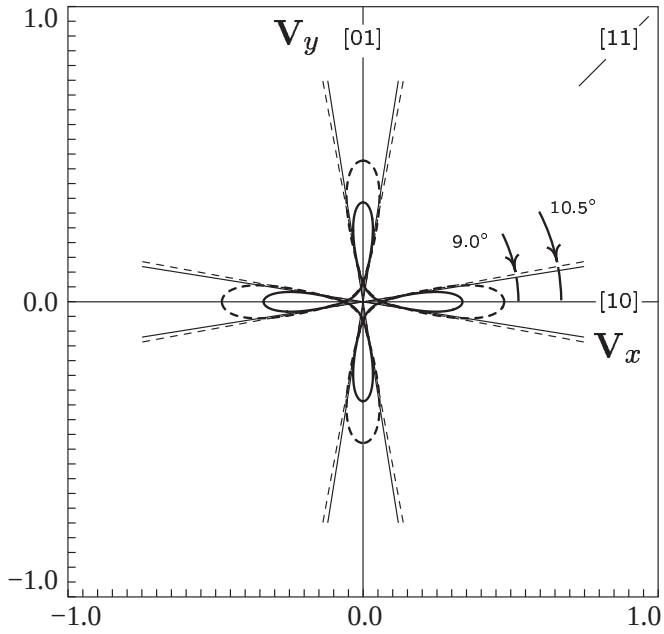


Figure 5.13: Wave contours corresponding to the normalized frequency $\Omega = 0.565$. Solid (dashed) wave contour corresponds to solid (dashed) iso-frequency contour in figure 5.12. The group velocity is plotted in the units of the speed of light in vacuum. The directions corresponding to the folds of the wave contour are shown.

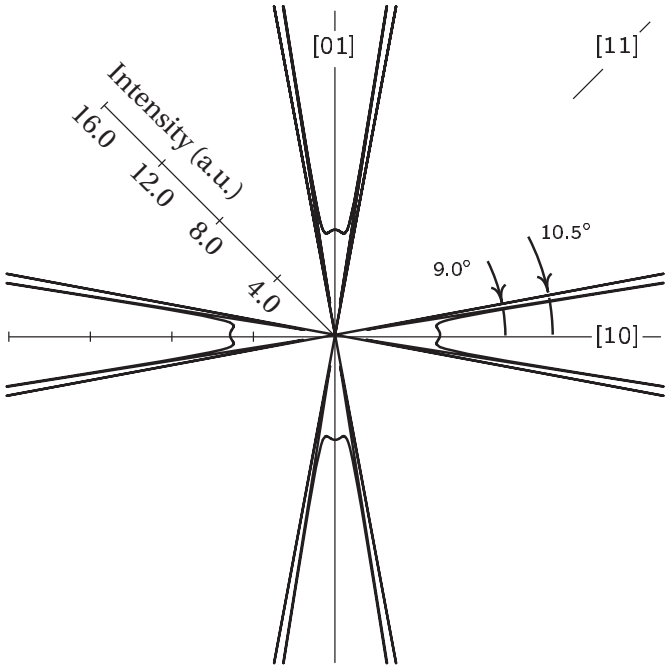


Figure 5.14: Angular distribution of radiative power corresponding to the normalized frequency $\Omega = 0.565$. The directions of infinite radiative power (caustic) coincide with the directions of the folds of the wave contour.

velocity is parallel to observation direction $\widehat{\mathbf{x}}$. It was also shown that the anisotropy of a photonic crystal reveals itself in the strongly non-spherical wave front leading to modifications of both far-field radiation pattern and spontaneous emission rate. By systematic analysis of the Maxwell equations a simple formulae to calculate the angular distribution of radiated power due to a point dipole placed in a photonic crystal was derived. The formulae only involves calculations of the wave vectors, the group velocity and the Gaussian curvature on an iso-frequency surface corresponding to the frequency of the oscillating dipole. This can be done by simple plane wave expansion method and is not computationally demanding. A numerical example was given for a square-lattice two-dimensional photonic crystal. It was shown by applying developed formalism and substantiated by FDTD calculations, that if a dipole frequency is within a partial photonic band gap, a far-field radiation pattern is strongly modified with respect to the dipole radiation pattern in vacuum, demonstrating suppression in the directions of the spatial stopband and enhancement in the direction of the group velocity, which is stationary with respect to a small variation of the wave vector.

# Bibliography


[1] P. Etchegoin and R. T. Phillips, "Photon focusing, internal diffraction, and surface states in periodic dielectric structures," *Phys. Rev. B* **53,** 12674–12683 (1996).

[2] D. N. Chigrin and C. M. Sotomayor Torres, "Periodic thin-film interference filters as one-dimensional photonic crystals," *Optics and Spectroscopy* **91,** 484–489 (2001).

[3] J. P. Wolfe, *Imaging Phonons: Acoustic Wave Propagation in Solid* (Cambridge University Press, Cambridge, 1998).

[4] B. Taylor, H. J. Maris, and C. Elbaum, "Phonon focusing in solids," *Phys. Rev. Lett.* **23,** 416–419 (1969).

[5] A. A. Maradudin, "Phonons and Lattice Inperfection," in *Phonons and Phonon Interactions*, T. A. Bak, ed., (Benjamin, New York, 1964), pp. 424–504.

[6] H. J. Maris, "Effect of finite phonon wavelength on phonon focusing," *Phys. Rev. B* **28,** 7033–7037 (1983).

[7] A. Gray, *Modern Differential Geometry of Curves and Surfaces with Mathematica* (CRC Press, Boca Raton, 1998).

[8] P. Yeh, *Optical Waves in Layered Media* (John Wiley and Sons, New York, 1988).

[9] J. D. Jackson, *Classical Electrodynamics* (John Wiley, New York, 1975).

[10] S. V. Gaponenko, V. N. Bogomolov, E. P. Petrov, A. M. Kapitonov, A. A. Eychmueller, A. L. Rogach, I. I. Kalosha, F. Gindele, and U. Woggon, "Spontaneous emission of organic molecules and semiconductor nanocrystals in a photonic crystal," *J. Lightwave Technol.* **17,** 2128–2137 (1999).

[11] H. P. Schiemer, H. M. van Driel, A. F. Koenderink, and W. L. Vos, "Modified spontaneous emission spectra of laser dye in inverse opal photonic crystal," *Phys. Rev. A* **63,** 011801R (2000).

[12] S. G. Romanov, T. Maka, C. M. Sotomayor Torres, M. Muller, and R. Zentel, "Emission in a $SnS_2$ inverted opaline photonic crystal," *Appl. Phys. Lett.* **79,** 731–733 (2001).

[13] S. G. Romanov, D. N. Chigrin, V. G. Solovyev, T. Maka, N. Gaponik, A. Eychmuller, A. L. Rogach, and Sotomayor Torres, "Light emission in a directional photonic bandgap," *Phys. Stat. Sol. (a)* **197,** 662–672 (2003).

[14] J. P. Dowling, M. Scalora, M. J. Bloemer, and C. M. Bowden, "The photonic band edge laser: a new approach to gain enhancement," *J. Appl. Phys.* **75,** 1896–1899 (1994).

[15] S. Nojima, "Enhancement of optical gain in two-dimensional photonic crystals with active lattice points," *Jpn. J. Appl. Phys. 2* **37,** L565–L567 (1998).

[16] K. Sakoda, "Enhanced light aplification due to group-velocity anomaly peculiar to two- and three-dimensional photonic crystals," *Optics Express* **4,** 167–176 (1999).

[17] G. A. Northrop and J. P. Wolfe, "Ballistic phonon imaging in germanium," *Phys. Rev. B* **22,** 6196–6212 (1980).

[18] A. Taflove, *Computational Electrodynamics: The Finite-Difference Time-Domain Method* (Artech House, Norwood, 1995).

[19] D. M. Sullivan, *Electromagnetic Simulation Using the FDTD Method* (IEEE Press, New York, 2002).

[20] J. P. Berenger, "A perfectly matched layer for absorption of electromagnetic waves," *J. Comp. Phys.* **114,** 185–200 (1994).

[21] *Emlab, ISE AG Integrated Systems Engineering*

# Chapter 6

# Radiation pattern of a classical dipole in a photonic crystal: self-interference of Bloch eigenwaves[1]

The signal detected in the given observation direction far from the radiating dipole is proportional to the emission rate in this direction. Due to the anisotropy of a photonic crystal, eigenwaves with significantly different wave vectors can have the same direction of their group velocities. As it was demonstrated in chapter 5, that leads to the enhancement of the radiated power of a point dipole in the corresponding group velocity direction. In the same time, if there are several waves reaching the detector and there is a relative difference in the lengths or directions of their wave vectors, these waves can interfere yielding an oscillation in the energy flux distribution at the detector plane. Thus, the modulation of angle resolved emission spectra from a coherent light source can be interpreted as the result of both emission rate modification and light interference at the detector position.

In this chapter, a physical picture of an interference fringes formation in the far-field radiation pattern of a classical dipole is discussed in the framework of the asymptotic analysis of Maxwell equations. The evaluation of the asymptotic form of the radiated field is given in section 6.1. A physical explanation and a relevance of results for experimental observation are discussed in section 6.2. In section 6.3 numerical examples are given. The main results of the chapter are summarized in section 6.4.

[1]This chapter is based on: D. N. Chigrin, "Radiation pattern of a classical dipole in a photonic crystal: self-interference of Bloch eigenwaves," manuscript in preparation for *Phys. Rev. E*

## 6.1 Asymptotic form of dipole field

Strictly speaking, the asymptotic behavior of the vector potential (5.14) is valid only if quadratic terms in the expansion (5.9) do not vanish, so that all higher order terms in the expansion can be neglected. A parabolic point of the iso-frequency surface is an example of vanishing quadratic terms in (5.9). Generally, the Gaussian curvature is zero at a parabolic point and one (both) of the principal curvatures of the iso-frequency surface is zero. Actually, the asymptotic behavior of the vector potential changes at parabolic points, i.e., the dependence of the vector potential on the inverse distance ($\sim |\mathbf{x}|^{-1}$), changes to a power dependence upon the inverse distance.

As an illustration one can consider the simple parabolic point $\mathbf{k}_0 = \mathbf{k}_n^0$ in the vicinity of which the function $h(\xi_1, \xi_2) = \mathbf{k}_n \cdot \widehat{\mathbf{x}}$ has the expansion:

$$h(\xi_1, \xi_2) = \mathbf{k}_0 \cdot \widehat{\mathbf{x}}_0 + \frac{1}{2}\alpha\xi_1^2 + \frac{1}{6}\beta\xi_2^3, \qquad \alpha = \alpha_{11}^0,\ \beta = \beta_{111}^0, \tag{6.1}$$

where $\widehat{\mathbf{x}}_0$ is the unit vector in the direction normal to the iso-frequency surface at the parabolic point $\mathbf{k}_0$. The local curvilinear coordinates $\xi_i$ has the origin at the parabolic point $\mathbf{k}_0$, with the coordinates $\xi_1$ and $\xi_2$ aligned along the directions of the principal curvatures of the iso-frequency surface at this point and with the coordinate $\xi_3$ aligned along $\widehat{\mathbf{x}}_0$. For the parabolic point $\mathbf{k}_0$ one of the principal curvatures vanishes ($\alpha_{22}^0 = 0$), while another principal curvature remains non-zero. Using the expansion (6.1) the asymptotic form of the field (5.8) is given by:

$$\begin{aligned} \mathbf{A}(\mathbf{r}) &\approx \frac{4\pi^2 c}{V} \frac{(\mathbf{a}_0^*(\mathbf{r}_0) \cdot \mathbf{d})\, \mathbf{a}_0(\mathbf{r})}{|\mathbf{V}_0|} e^{i\mathbf{k}_0 \cdot \mathbf{x}} \\ &\times \oint_{-\infty}^{\infty} d\xi_1 d\xi_2 \exp\left( i\,|\mathbf{x}| \left( \frac{\alpha}{2}\xi_1^2 + \frac{\beta}{6}\xi_2^3 \right) \right), \end{aligned} \tag{6.2}$$

where $\mathbf{A}_0(\mathbf{r}) = \mathbf{a}_0(\mathbf{r}) e^{i\mathbf{k}_0 \cdot \mathbf{r}}$ and $\mathbf{V}_0$ are the vector potential and the group velocity of the Bloch eigenwave associated with the parabolic point $\mathbf{k}_0$, respectively. Calculating the integral in (6.2), apart from the integral

$$\int_{-\infty}^{\infty} d\xi \exp\left( i\frac{x\alpha}{2}\xi^2 \right) = \sqrt{\frac{2\pi}{x\,|\alpha|}} \exp\left( -\frac{i\pi}{4} \mathrm{sing}(\alpha) \right) \tag{6.3}$$

for the direction $\xi_1$, one has another integral for direction $\xi_2$, namely:

$$\int_{-\infty}^{\infty} d\xi \exp\left( i\frac{x\beta}{6}\xi^3 \right) = \frac{3}{\sqrt[3]{x\,|\beta|}} \Gamma\left( \frac{4}{3} \right), \tag{6.4}$$

where $\Gamma\left(\frac{4}{3}\right)$ is the Gamma function. Now, combining (6.3) and (6.4) the following

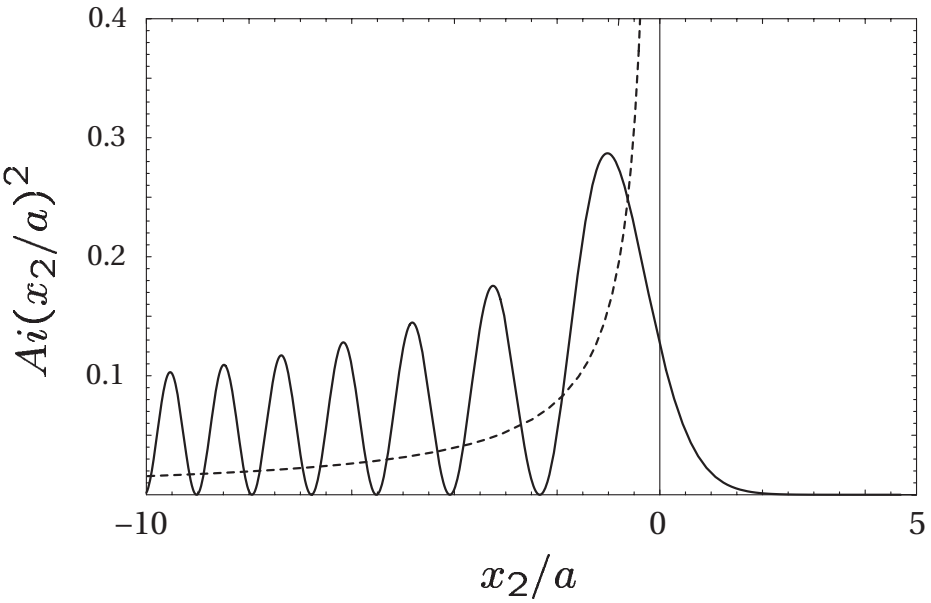


Figure 6.1: Plot of the Airy function $\left[\mathrm{Ai}\left(x_2/a\right)\right]^2$ (solid line) and its mean value $\left(1/4\pi\right)^{-1}\left(x_2/a\right)^{-1/2}$ (dashed line). The dashed line can be considered as the "geometrical optics" approximation of the Airy function.

expression for the asymptotic vector potential associated with the parabolic point (6.1) can be obtained:

$$\begin{aligned}\mathbf{A}(\mathbf{r},t) &\approx \exp\left(-i\left(\omega_0 t+\frac{i\pi}{4}\left(\mathrm{sign}(\alpha)\right)\right)\right)\Gamma\left(\frac{4}{3}\right)\\ &\times \frac{c}{V}\frac{\left(\mathbf{A}_0^*(\mathbf{r}_0)\cdot\mathbf{d}\right)\mathbf{A}_0(\mathbf{r})}{|\mathbf{V}_0|}\frac{12\sqrt{2\pi^5}}{|\alpha|^{1/2}\,|\beta|^{1/3}\,|\mathbf{r}-\mathbf{r}_0|^{5/6}}.\end{aligned} \tag{6.5}$$

The amplitude of the vector potential in (6.5) is proportional to $|\mathbf{x}|^{-5/6}$ in contrast to the inverse dependence on distance of the asymptotic vector potential (5.14). Then the emission intensity associated with a parabolic point falls off with the distance as $|\mathbf{x}|^{-5/3}$ in contrast to the usual inverse square law $|\mathbf{x}|^{-2}$ for other directions. If there are no additional singularities on the parabolic line, the product $|\alpha|\,|\beta|^{1/2}\sim K$, where $K$ is the Gaussian curvature at an arbitrary point of the iso-frequency surface. Then the emission intensity is also proportional to $K^{-1}\,|\beta|^{-1/6}$. Thus, at large $|\mathbf{x}|$, the energy flux along the direction corresponding to a parabolic point on the iso-frequency surface exceeds the energy flux along the direction corresponding to an elliptical point by a factor $|\mathbf{x}|^{1/3}\,|\beta|^{1/6}$.

The expression (6.5) gives an asymptotic vector potential in the direction $\widehat{\mathbf{x}}_0$ associated with a parabolic point on the iso-frequency surface $\mathbf{k}_0$, i. e., in the direction of the group velocity at the parabolic point. Now, the asymptotic field for directions $\widehat{\mathbf{x}}$

near the direction of that group velocity will be calculated. As before, the origin of the coordinates $\xi_i$ is chosen at the parabolic point, where the direction $\widehat{\mathbf{x}}$ is coincides with direction $\widehat{\mathbf{x}}_0$. It is assumed, that the principal curvature vanishes in the $\xi_2$ direction. Let the position $\mathbf{x}$ $(\mathbf{x}\|\widehat{\mathbf{x}})$ be described by coordinates $x_i$, which have the same orientation as the coordinates $\xi_i$. Then, since $\mathbf{x}$ is nearly parallel to $\widehat{\mathbf{x}}_0$ one has from (6.1):

$$\xi_3 = \frac{1}{2}\alpha\xi_1^2 + \frac{1}{6}\beta\xi_2^3$$

and

$$\begin{aligned} \mathbf{k}_n \cdot \mathbf{x} &\approx \mathbf{k}_0 \cdot \mathbf{x} + \xi_1 x_1 + \xi_2 x_2 \\ &+ \left(\frac{1}{2}\alpha\xi_1^2 + \frac{1}{6}\beta\xi_2^3\right) x_3. \end{aligned} \tag{6.6}$$

Using expansion (6.6) the asymptotic form of the field (5.8) is given by:

$$\begin{aligned} \mathbf{A}(\mathbf{r}) &\approx \frac{4\pi^2 c}{V}\frac{\left(\mathbf{a}_0^*(\mathbf{r}_0)\cdot\mathbf{d}\right)\mathbf{a}_0(\mathbf{r})}{|\mathbf{V}_0|}e^{i\mathbf{k}_0\cdot\mathbf{x}} \\ &\times \int_{-\infty}^{\infty} d\xi_1 e^{i\left(x_1\xi_1 + \frac{1}{2}\alpha|\mathbf{x}|\xi_1^2\right)} \int_{-\infty}^{\infty} d\xi_2 e^{i\left(x_2\xi_2 + \frac{1}{6}\beta|\mathbf{x}|\xi_2^3\right)} \end{aligned} \tag{6.7}$$

where the fact that $|\mathbf{x}|$ and $x_3$ are approximately equal was used. The integral in (6.7) over $\xi_1$ is calculated simply to be:

$$\int_{-\infty}^{\infty} d\xi_1 e^{i\left(x_1\xi_1 + \frac{1}{2}\alpha|\mathbf{x}|\xi_1^2\right)} = \frac{\sqrt{2\pi}}{|\alpha|^{1/2}|\mathbf{x}|^{1/2}} e^{-i\frac{x_1^2}{2\alpha|\mathbf{x}|}} e^{-\frac{i\pi}{4}\mathrm{sign}(\alpha)},$$

while the integral over $\xi_2$ results in:

$$\int_{-\infty}^{\infty} d\xi_2 e^{i\left(x_2\xi_2 + \frac{1}{6}\beta|\mathbf{x}|\xi_2^3\right)} = \frac{2^{4/3}\pi}{|\beta|^{1/3}|\mathbf{x}|^{1/3}} \mathrm{Ai}\left(x_2 \frac{2^{1/3}}{|\beta|^{1/3}|\mathbf{x}|^{1/3}}\right),$$

where Ai is the Airy function. Then the asymptotic vector potential (6.7) is finally given by:

$$\begin{aligned} \mathbf{A}(\mathbf{r},t) &\approx \frac{c}{V}\exp\left(-i\left(\omega_0 t + \frac{x_1^2}{2\alpha|\mathbf{x}|} + \frac{\pi}{4}\mathrm{sign}(\alpha)\right)\right) \\ &\times \frac{\left(\mathbf{A}_0^*(\mathbf{r}_0)\cdot\mathbf{d}\right)\mathbf{A}_0(\mathbf{r})}{|\mathbf{V}_0|} \frac{8\pi^3 2^{5/6}\pi}{|\alpha|^{1/2}|\beta|^{1/3}|\mathbf{r}-\mathbf{r}_0|^{5/6}} \mathrm{Ai}\left(\frac{x_2}{a}\right), \end{aligned} \tag{6.8}$$

where $a = (|\beta||\mathbf{x}|/2)^{1/3}$.

As in the case of the asymptotic field (6.5), the amplitude of the vector potential in (6.8) is proportional to $|\mathbf{x}|^{-5/6}$ and $K^{-1/2}|\beta|^{-1/12}$. This causes the energy flux in the

direction $\mathbf{x}$ to fall off as $|\mathbf{x}|^{-5/3}$ and exceeds the energy flux along the other directions in the ratio $|\mathbf{x}|^{1/3}|\beta|^{1/6}$. The dependence of the energy flux in the plane of the vanishing principal curvature is given by the square of the Airy function $[\mathrm{Ai}\,(x_2/a)]^2$. When $x_2/a$ is positive, the energy flux is small and drops exponentially while the angle between the direction of observation and the direction corresponding to the parabolic point increases (Fig. 6.1). For negative $x_2/a$, the flux oscillates rapidly and has a mean value averaged over one cycle proportional to $\sim (x_2/a)^{-1/2}$ (Fig. 6.1). The mean value of the energy flux is then proportional to $|\alpha|^{-1}|\beta|^{-1/2} \sim K^{-1}$ and $|\mathbf{x}|^{-2}$ and coincides with the asymptotic energy flux associated with an elliptical point of the iso-frequency surface (5.14), demonstrating focusing of the energy flux in the direction corresponding to the parabolic point of the iso-frequency surface.

## 6.2 Interference of Bloch eigenwaves

In the far field, where the source-to-detector distance is much larger than the source size and the wavelength, the part of the wave surface limited to the small solid angle can be approximated to a Bloch eigenwave with its group velocity within this angle. Then, for the direction near the fold of the wave surface (Figs. 5.3 and 6.2) the field is a superposition of three Bloch eigenwaves (Fig. 6.2). If there is a relative difference in the lengths or directions of the wave vectors of these Bloch eigenwaves, the eigenwaves can interfere yielding oscillations in the energy flux distribution. Two general conditions are required for interference to occur. The polarization states of the Bloch eigenwaves must be nonorthogonal and the Bloch eigenwaves must overlap in space [1]. This kind of interference of the Bloch eigenwaves will be called further *a self-interference*, to stress the fact that the field produced by the light source inside a photonic crystal can interfere with itself producing an interference patten in the energy flux distribution. A similar self-interference effect also happens in the case of ballistic phonons propagation in an acoustically anisotropic crystals [2, 3].

For a more qualitative measure of the self-interference effect an iso-frequency surface superimposed on a photonic crystal is considered in figure 6.3. Here the evaluation presented by Hauser et al. [3] for the self-interference of ultrasound in a crystal is followed. In figure 6.3, dots are parabolic points of zero curvature. A light source is located near the bottom surface of a photonic crystal and generates an uniform distribution of wave vectors. A Bloch eigenwave with wave vector $\mathbf{k}_0$ propagates with the group velocity $\mathbf{V}_0$, normal to the iso-frequency surface at $\mathbf{k}_0$, arriving at a point $\mathbf{R}_0$ on the opposite surface of the crystal. Near a parabolic point the iso-frequency surface is practically flat, neighboring wave vectors have nearly the same group velocity. This gives rise to the high-intensity caustic in the detected intensity distribution (Fig. 6.3-

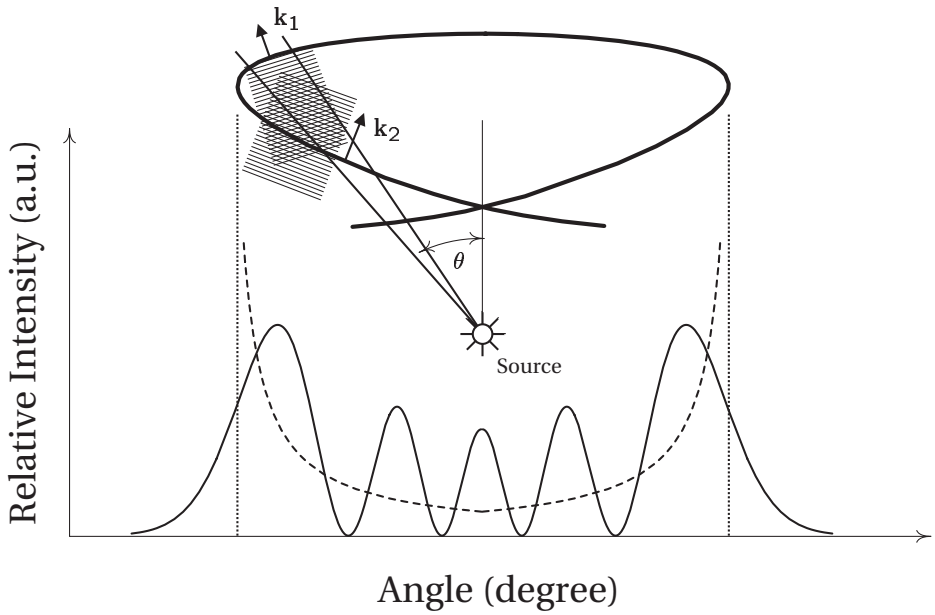


Figure 6.2: Diagram illustrating the self-interference of the Bloch eigenwaves in a photonic crystal. A section of the wave surface with a fold is shown (thick solid line). An asymptotic intensity (solid line) displays oscillations as the angle passes the fold section of the wave surface. An asymptotic intensity in the "geometrical optics" limit demonstrates focusing caustics in the direction of the folds (dashed line). Within a small solid angle the far-field of a point source arises from the superposition of three Bloch eigenwaves with different wave vectors. These Bloch eigenwaves interfere leading to oscillations in the intensity distribution. For clarity only two wave vectors are illustrated.

left). If the detector is moved to a point $\mathbf{R}_1$ slightly away from $\mathbf{R}_0$, two distinct Bloch eigenwaves with different wave vectors $\mathbf{k}'_1$ and $\mathbf{k}'_2$ near $\mathbf{k}_0$ arrive at the detector (Fig. 6.3-right). If the surface were perfectly flat near $\mathbf{k}_0$, then $\mathbf{k}'_1 \cdot \mathbf{R}_1 = \mathbf{k}'_2 \cdot \mathbf{R}_1$, and the two eigenwaves would always remain in phase at the detector, interfering constructively. In reality the iso-frequency surface is curved near the parabolic point, so as $\mathbf{R}_1$ is rotated downward the corresponding waves begin to interfere destructively, producing an Airy pattern (Figs. 6.1-6.3). If $\mathbf{k}'_1$ and $\mathbf{k}'_2$ are close to $\mathbf{k}_0$, and $q \equiv \mathbf{k}'_1 - \mathbf{k}_0 \approx \mathbf{k}'_2 - \mathbf{k}_0$, then destructive interference will take place, if the total phase difference of the light as it travels through the sample, $2\mathbf{q} \cdot \mathbf{R}_1$, is an odd integer multiple of $\pi$.

Strictly speaking, there is one more Bloch eigenwave following in the observation direction in the fold region of the wave surface (Figs. 6.2-6.3). This eigenwave is depicted as $\mathbf{k}_1$ and $\mathbf{k}'_3$ in the left and right panels of figure 6.3, respectively. To obtain a complete picture of the self-interference near the fold of the wave surface, a three-wave interference should be taken into account, which would lead to more complicated interference patterns in the intensity distribution. Here, the influence of this third eigenwave is neglected for simplicity, hence this eigenwave usually has a relatively

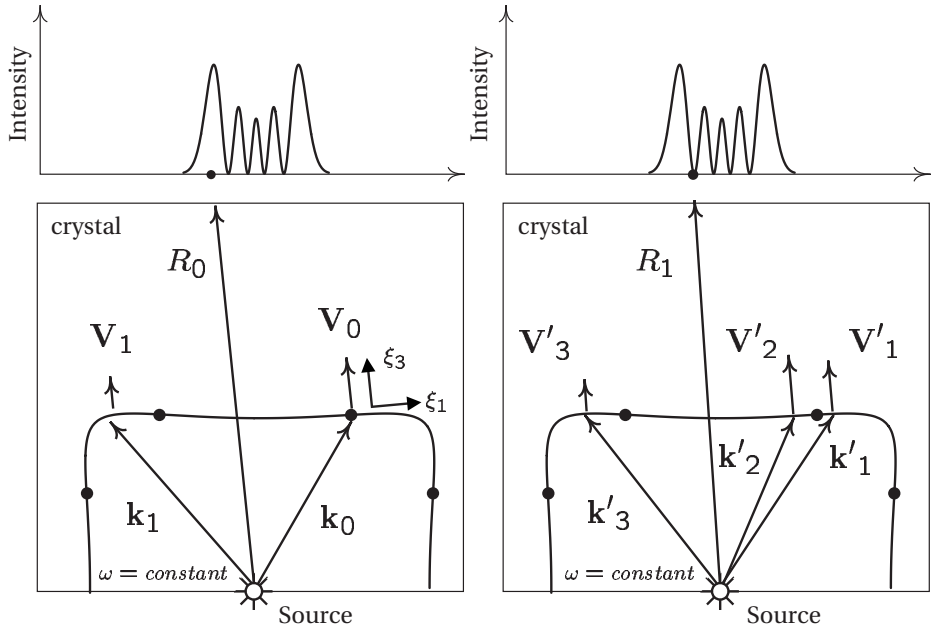


Figure 6.3: Schematics of self-interference in a photonic crystal. The iso-frequency surface is a sketch of the iso-frequency surface of a real 2D photonic crystal. The plot on the top is the detected intensity distribution. Left: For the wave vector $\mathbf{k}_0$, the group velocity is $\mathbf{V}_0$ and the wave arrives at $\mathbf{R}_0$. Right: There are two eigenwaves with different wave vectors $\mathbf{k}'_1$ and $\mathbf{k}'_2$, the group velocities of which ( $\mathbf{V}'_1$ and $\mathbf{V}'_2$ respectively) point in the same direction $\mathbf{R}_1$. The difference in the wave vectors of these eigenwaves results in the waves arriving at $\mathbf{R}_1$ with different phases leading to interference. Slow eigenwaves contributing to the total flux in the observation direction are depicted as $\mathbf{k}_1$ and $\mathbf{k}'_3$ (see text for further details).

small group velocity and could arrive at the detector too late to interfere with the eigenwaves $\mathbf{k}'_1$ and $\mathbf{k}'_2$.

From the perspective of the self-interference effect, the mean value of the asymptotic energy flux (6.8) averaged over one cycle of Airy oscillations can be viewed as a "geometrical optics" approximation of the actual energy flux. This approximation then corresponds to the ray description of wave propagation, where the energy flux is simply proportional to the density of rays crossing a detector surface. In this picture the interference among different rays is neglected. As it has been mentioned above, the mean value of the asymptotic flux (6.8) coincides with the asymptotic energy flux (5.14) derived for elliptical points of the iso-frequency surface. So, the asymptotic energy flux corresponding to an elliptical point can be also considered as a "geometrical optics" approximation, and can be used for all points of the iso-frequency surface within this approximation.

In a typical experiment the differences between the energy flux (6.8) and its "geometrical optics" approximation (5.14) will be reduced by the effect of the finite size of

the light source and the detector. It is clear that if the linear dimensions of the source area and detector are $L$, the intensity is averaged over $x_2$ values with a spread of $L$. To see the oscillations of the energy flux one therefore needs $L \leq \Delta\theta \times R_1$, where $R_1$ is the distance between the source and the detector and $\Delta\theta$ is an angular separation of the fringes of intensity distribution.

To estimate this angular separation, Bloch eigenwaves $\mathbf{k}'_1$ and $\mathbf{k}'_2$ are further approximated by plane waves. Then their superposition at the detector position $\mathbf{R}_1$, assuming that they have the same polarization, is:

$$e^{i\mathbf{k}'_1\cdot\mathbf{R}_1} + e^{i\mathbf{k}'_2\cdot\mathbf{R}_1} = 2\cos\left(\Delta\mathbf{k}\cdot\mathbf{R}_1\right) e^{i\mathbf{k}_0\cdot\mathbf{R}_1},$$

which is a plane wave with average wave vector $\mathbf{k}_0 = \left(\mathbf{k}'_1 + \mathbf{k}'_2\right)/2$, modulated by a cosine function with effective wave vector $\Delta\mathbf{k}/2 = \left(\mathbf{k}'_2 - \mathbf{k}'_1\right)/2$. When $\Delta\mathbf{k}\cdot\mathbf{R}_1 = \Delta k_\parallel R_1 = \pi$, the waves interfere destructively at the detector. To estimate $\Delta k_\parallel$ a local Cartesian coordinate system $\xi_i$ with the origin at $\mathbf{k}_0$ and $\xi_3$ along $\mathbf{V}_0$ is chosen as it is shown in figure 6.3-left. Then, an iso-frequency surface near the parabolic point can by parameterized as $\xi_3 = -a\xi_2^3/k_0$ and $\Delta k_\parallel = -2\xi_3 = 2a\xi_2^3/k_0^2$. Therefore, the first minimum in the intensity will occur when

$$\xi_2 = \left(\pi k_0^2/2aR_1\right)^{1/3} \sim R_1^{-1/3}\lambda^{-2/3},$$

where $\lambda = 2\pi/k_0$ is the average wavelength. Finally, the coordinate-space angle between the intensity maximum and the first minimum is given by [3]:

$$\Delta\theta \approx \left|\mathbf{V}'_1 - \mathbf{V}_0\right|/\mathbf{V}_0 = 3a\left(\pi/2ak_0R_1\right)^{2/3} \sim \left(\lambda/R_1\right)^{2/3}. \tag{6.9}$$

Then for an optical wavelength, e.g., 500 nm, and a distance to the detector of 1 cm, the linear dimension of the light source and the spatial resolution of the detector should be smaller than 10 $\mu$m. Thus, in most experiments the "geometrical optics" approximation reasonably represents an asymptotic emission intensity of a light source inside a photonic crystal.

## 6.3 Numerical example

In this section different approximations of the light emission pattern discussed in previous sections are compared. Numerical calculations are performed for a point source placed inside a two-dimensional polymer photonic crystal. A point source produces an isotropic and uniform distribution of wave vectors $\mathbf{k}_n$ with the frequency $\omega_0$. Polymer has the refractive index 1.56 . Radius of holes is $r = 0.15d$, where $d$ is the lattice

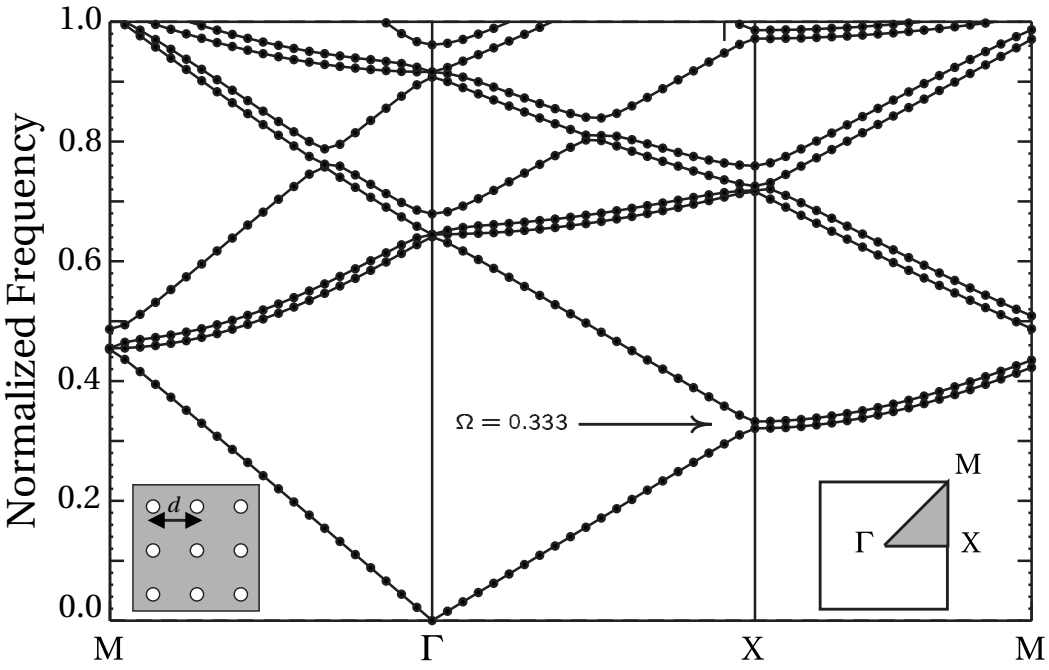


Figure 6.4: Photonic band structure of the square lattice of air holes made in a polymer with refractive index 1.56. Radius of holes is $r = 0.15d$, where $d$ is the lattice period. The band structure is given for TM polarization. The frequency is normalized to $\Omega = \omega d/2\pi c = d/\lambda$. $c$ is the speed of light in the vacuum. Insets show the first irreducible Brillouin zone (right) and a part of the lattice (left).

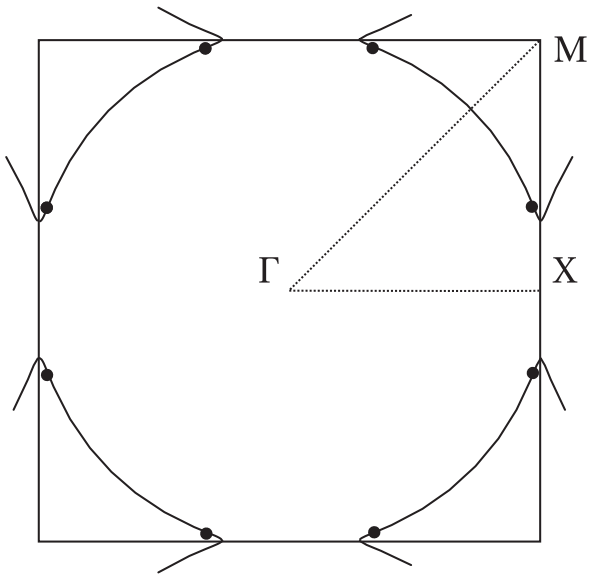


Figure 6.5: Iso-frequency contour of the square lattice photonic crystal (Fig. 6.4) for the normalized frequence $\Omega = 0.333$. Parabolic point are marked by the black dots. The first Brillouin zone of the lattice is plotted in order to show the spatial relation between zone boundary and iso-frequency contours.

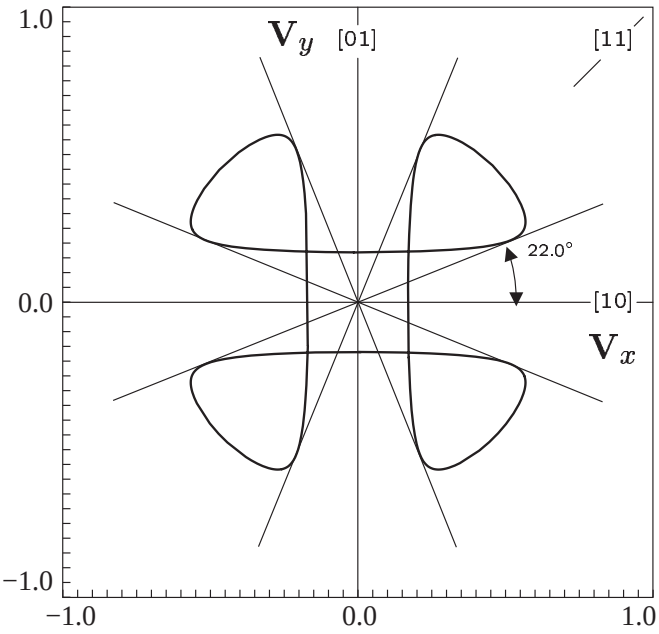


Figure 6.6: Wave contour corresponding to the normalized frequency $\Omega = 0.333$. The group velocity is plotted in units of the speed of light in vacuum. The directions corresponded to the folds of the wave contour are shown.

period. The refractive index is chosen close to that of polystyrene in the optical region. In this case the separation between the center of rods along the lattice vectors should be on the order of a few hundreds micrometers. The photonic band structure for TM polarized light is presented in the figure 6.4.

As it was pointed out in section 6.1, the main contribution to the far-field of a point source inside a photonic crystal comes from the vicinity of the wave vector of the eigenmodes with the group velocity in the observation direction. That means that the far-field emission intensity of a point source is mainly given by the square of the integral in (5.8)

$$I_w \sim \sum_n \left| \oint_{-\infty}^{\infty} d^2\mathbf{k}_n e^{i\mathbf{k}_n\cdot(\mathbf{r}-\mathbf{r}_0)} \right|^2 . \tag{6.10}$$

In the "geometrical optics" approximation (5.14) the main contribution to the far-field emission intensity is given by an inverse Gaussian curvature of the iso-frequency surface,

$$I_g \sim \sum_\nu \sum_n \left| K^\nu_{n\mathbf{k}} \right| .^{-1} \tag{6.11}$$

The iso-frequency contours for the normalized frequency $\Omega = 0.333$ is presented in figure 6.5. The frequency belongs to the first photonic band and it is within the first stopband in the ΓX direction of the crystal. The iso-frequency contour is an open contour and has alternating regions of Gaussian curvature with a different sign.

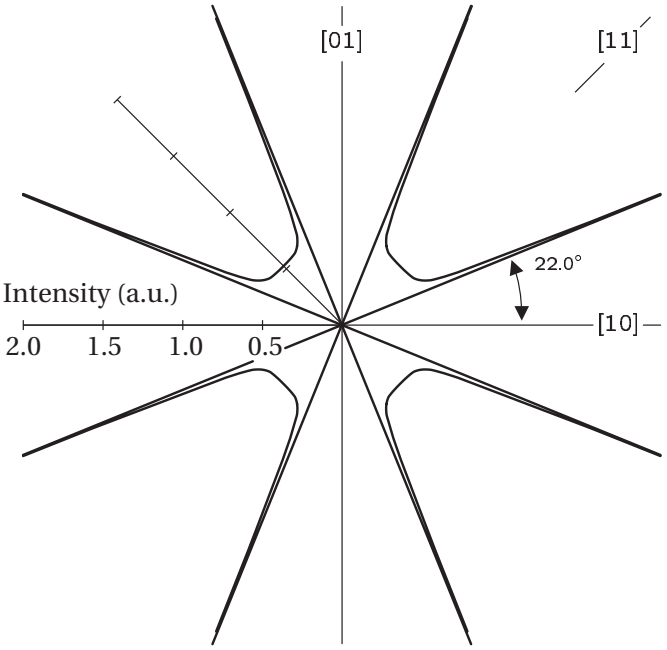


Figure 6.7: Angular distribution of radiative power corresponding to the normalized frequency $\Omega = 0.333$. The directions of infinite radiative power (caustic) coincide with the directions of the folds of the wave contour (Fig. 6.6).

Parabolic points, where the Gaussian curvature vanishes, are marked by black dots in the figure 6.5. A vanishing curvature results in the folds of the wave contour and in the focusing of the light in the folds direction. The wave contour corresponding to the iso-frequency $\Omega = 0.333$ is presented in figure 6.6. A pair of parabolic points in the first quarter of the Brillouin zone results in a cuspidal structure of the wave contours in the first quarter of the coordinate space. In the figure 6.7 a polar plot of the main contribution to the far-field intensity (6.11) is presented. The energy flux is strongly anisotropic, showing relatively small intensity in the directions of the stopband, and infinite intensity (caustics) in the directions of the folds.

In figure 6.8 a comparison of the "geometrical optics" (6.11) and "wave optics" (6.10) approximations of the far-field emission intensity is given. A normalized inverse Gaussian curvature of the iso-frequency surface $\Omega = 0.333$ is presented in the top panel. Focusing directions, 23° apart from the [11] direction of the square lattice, are clearly seen. The integral (6.10) evaluated at a distance 100 periods apart from the point source is given in the middle and bottom panels of figure 6.8. A normalized intensity distribution presented in the middle panel was calculated by reducing the integration limits in (6.10) to the close neighborhood of the parabolic point of the iso-frequency surface. Then the result of the integration is similar to one in (6.8) and an angular distribution of the emission intensity resembles the square of the Airy function. In practice, this approximation takes into account an interference of only

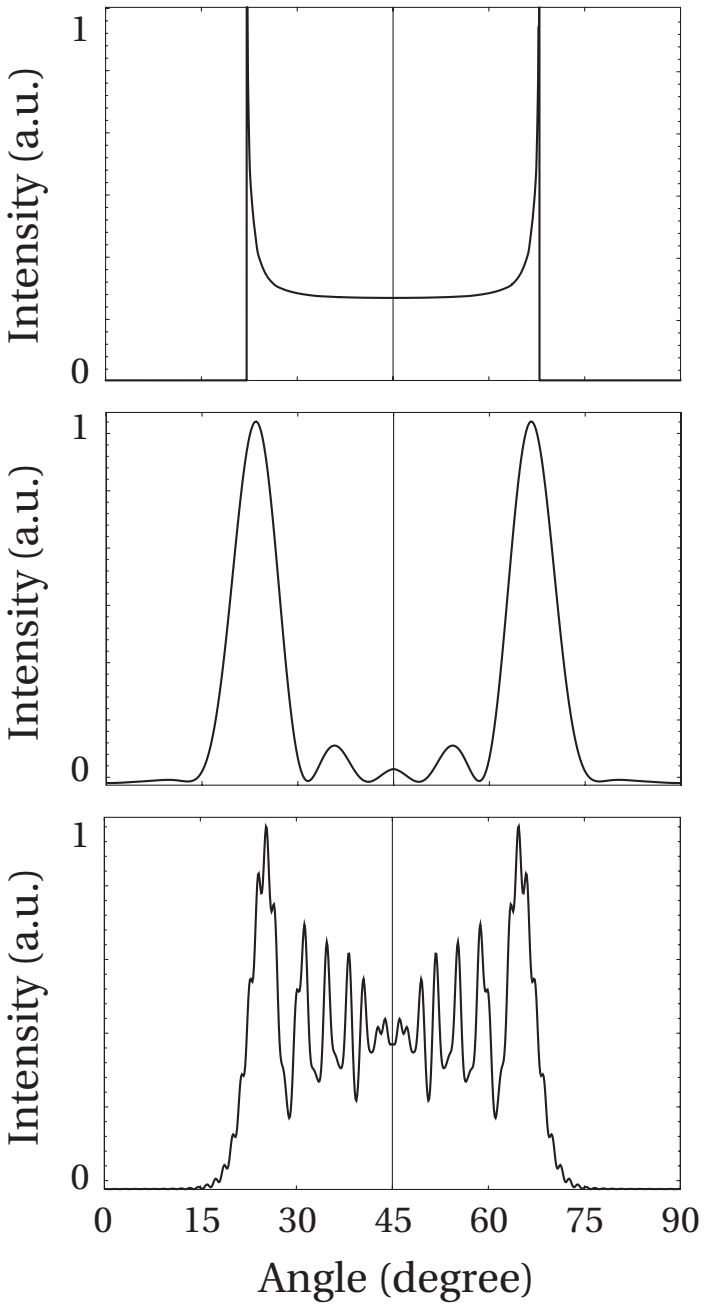


Figure 6.8: "Geometrical optics" Eq. (6.11) and "wave optics" Eq. (6.10) approximations of the far-field emission intensity. Normalized frequency is $\Omega = 0.333$. The distance between a point source and a detector is 100 lattice periods. The top panel is for the "geometrical optics" approximation. The middle and bottom panels are for the "wave optics" approximations. See text for more details.

two Bloch eigenwaves in the fold region. If the three wave interference is taken into account, by extending the integration limits in (6.10) over all iso-frequency surface in the first quarter of the Brillouin zone, a more complex interference pattern appears in the angle resolved emission intensity distribution (Fig. 6.8-bottom). Both "wave

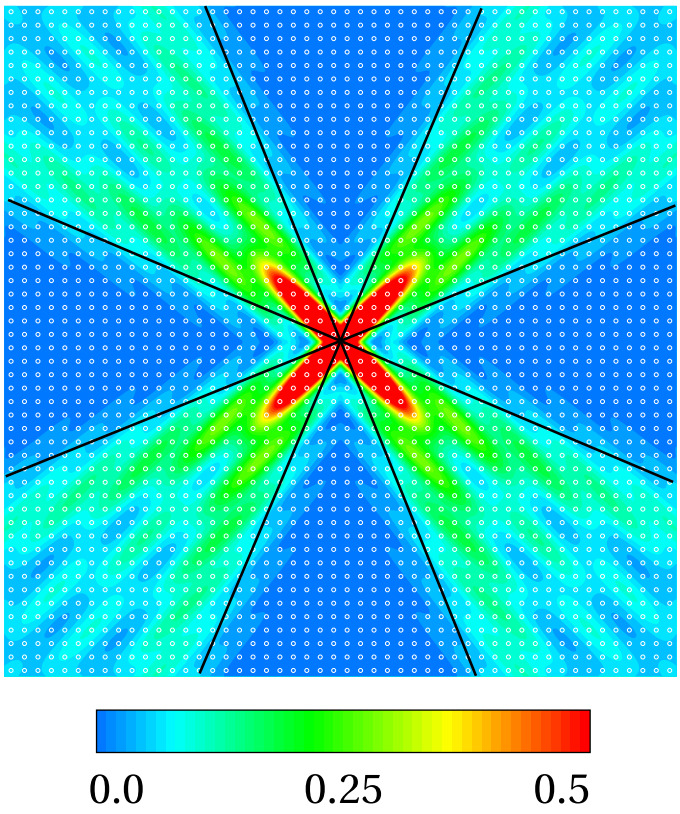


Figure 6.9: An asymptotic map of the intensity distribution inside a $50 \times 50$ periods photonic crystal. The normalized frequency is $\Omega = 0.333$. The structure of the crystal is superimposed on the field map. The highest values of the field are colored red; the lowest are colored blue. Fold directions are shown by black lines.

optics" approximations show an intensity enhancement along the fold directions.

In figure 6.9 a two dimensional map of the intensity distribution inside a $50 \times 50$ periods photonic crystal is presented. The intensity distribution was calculated using (6.10) by integrating over the complete iso-frequency contour $\Omega = 0.333$. The structure of the crystal is superimposed on the field map. The highest values of the field are colored red; the lowest are colored blue. Fold directions are shown by black lines. A focusing of the light in the fold direction together with an Airy-like oscillations between folds directions are clearly seen in figure 6.9.

To substantiate the results of the asymptotic analysis, FDTD calculations were done [4, 5]. The simulated structure was a $50 \times 50$ lattice of air holes in a polymer with refractive index $n = 1.56$ and holes radius is $r = 0.15d$. The crystal is surrounded by an extra $2d$ wide layer of polymer. The simulation domain was discretized into squares with a side $\Delta = d/32$. The total simulation region was $1728 \times 1728$ cells plus 8-cell wide perfectly matched layer (PML) [6]. An isotropic point light source was modeled by a soft source [4, 5] with a homogeneous spacial dependence and sinusoidal temporal

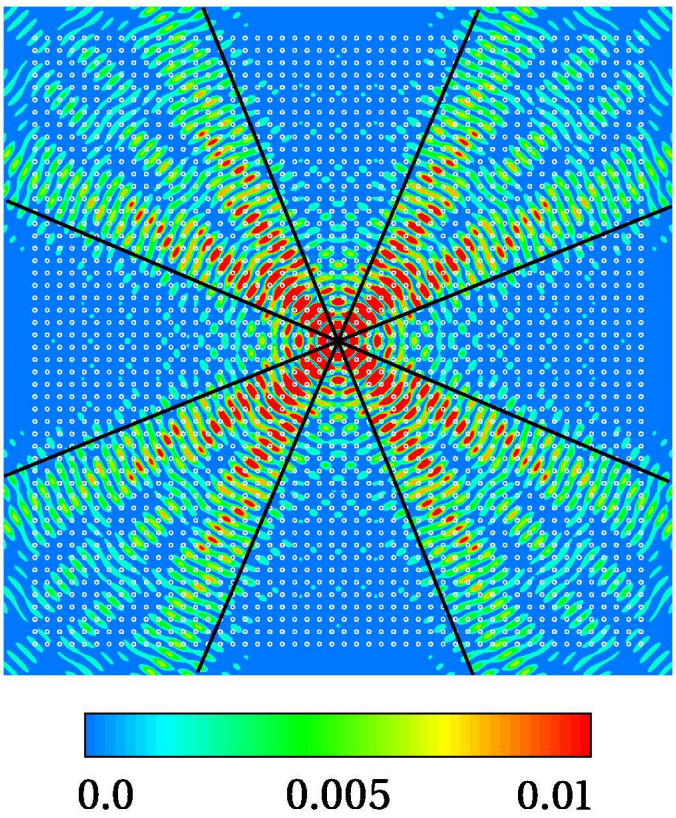


Figure 6.10: FDTD calculation. Map of the modulus of the Poynting vector field for a $50 \times 50$ rod photonic crystal excited by an isotropic point source at the normalized frequency $\Omega = 0.333$. The location of the crystal in the simulation is shown together with asymptotic directions of photon focusing caustics.

dependence of the signal.

In figure 6.10 the map of the modulus of the Poynting vector field is shown, when a $50 \times 50$ periods crystal is excited by an isotropic point source at the normalized frequency $\Omega = 0.333$. The point source is placed in the middle of the crystal. A field map is shown for one instant time step. The snap-shots were captured after 10000 time steps, where the time step was $4.38 \times 10^{-17}$ s (0.99 of the Courant value). The structure of the crystal is superimposed on the field map. The highest values of the field are colored red; the lowest are colored blue. It is seen, that the emitted light is focused in the directions of the folds (black lines). Moreover, an interference pattern between the folds directions is in a reasonable agreement with an interference pattern predicted using an asymptotic analysis (Fig. 6.9). For the FDTD calculations, a periodic modulation of the intensity in the radial direction (Fig. 6.10) will go away if time averaging is performed. A comparison of the intensity distribution 20 periods apart from the point source is given in figure 6.11. A reasonable agreement between interference minima and maxima positions for the asymptotic (solid line) and the FDTD (dashed line)

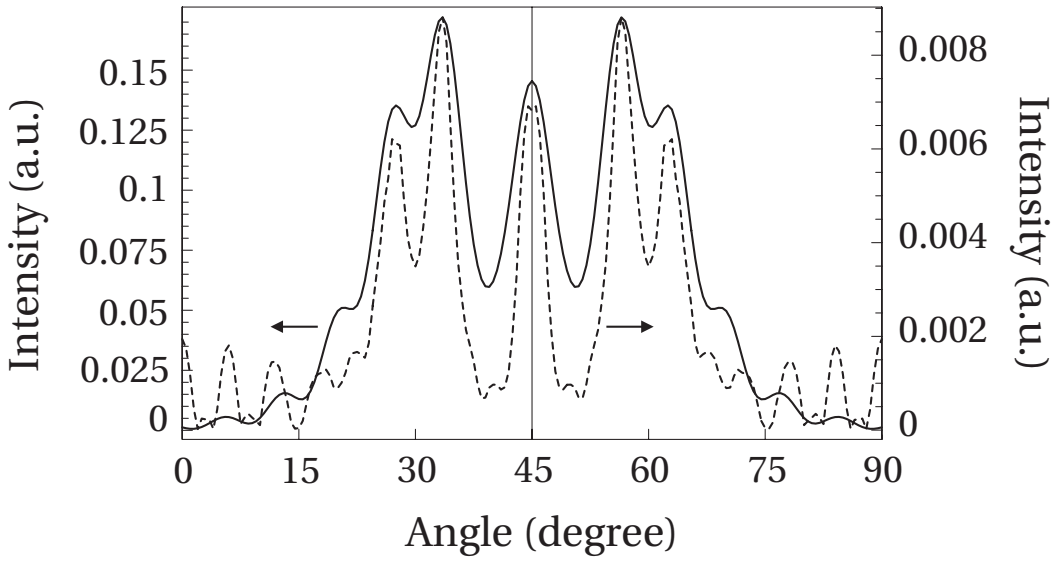


Figure 6.11: A comparison of the intensity distribution of the asymptotic (solid line) and the FDTD (dashed line) calculations. The distance between a point source and a detector is 20 lattice periods in both cases.

calculations is shown. A disagreement in the absolute values of the angular intensity distributions is mainly because of prefactor of the integral in (5.8) which was neglected in (6.10) for simplicity.

## 6.4 Summary

In this chapter it was shown that the intensity modulation of angle resolved emission spectra can be both due to the emission rate modification and the interference of several photonic crystal eigenmodes with different wave vectors approaching detector at the same time. Using an asymptotic analysis of Maxwell's equations, "geometrical optics" and "wave optics" approximations of the dipole field in the radiation zone were introduced. The physical reasons for the interference pattern formation and the possibilities of experimental observation of them were discussed. A numerical example was given in the case of polymer two-dimensional photonic crystal. It was shown that rigorous FDTD calculations are in a reasonable agreement with the developed approximate analysis.

# Bibliography


[1] P. St. J. Russell, "Interference of intagrated Floquet-Bloch waves," *Phys. Rev. A* **33,** 3232–3242 (1986).

[2] H. J. Maris, "Effect of finite phonon wavelength on phonon focusing," *Phys. Rev. B* **28,** 7033–7037 (1983).

[3] M. R. Hauser, R. L. Weaver, and J. P. Wolfe, "Interference of integrated Floquet-Bloch waves," *Phys. Rev. A* **33,** 3232–3242 (1986).

[4] A. Taflove, *Computational Electrodynamics: The Finite-Difference Time-Domain Method* (Artech House, Norwood, 1995).

[5] D. M. Sullivan, *Electromagnetic Simulation Using the FDTD Method* (IEEE Press, New York, 2002).

[6] J. P. Berenger, "A perfectly matched layer for absorption of electromagnetic waves," *J. Comp. Phys.* **114,** 185–200 (1994).

# Chapter 7

# Angular distribution of emission intensity in inverted opals[1]

In general, photonic crystal possesses a lattice periodicity on the light wavelength scale. This constraint sets a serious challenge to fabricate a three-dimensional photonic crystal operating in the visible. There are several approacher towards three-dimensional photonic crystals, such as a sequential layer-by-layer stacking of two-dimensional structures fabricated by electron-beam lithography [1, 2] or parallel processing by focused ion beam etching [3], autocloning [4] or light interference lithography [5, 6, 7]. So far, the only three-dimensional photonic crystal in the visible are opals [8, 9, 10]. In this chapter, experimental results, obtained at the University of Wuppertal (Wuppertal, Germany) [11], on the photoluminescence (PL) of dye molecules embedded in a three-dimensional opaline photonic crystal with a directional bandgap are analyzed within the theoretical model developed in chapter 5.

Opals are composed from identical-size dielectric spheres self-assembled in the face-centered cubic (fcc) lattice [8]. Empty interstitials between dielectric spheres can be infilled with another material to produce complex composites from, e.g. high refractive index semiconductors [9]. Spheres of opal can be then dissolved leaving behind inverted opals consisting of the semiconductor carcass and air spheres. In the inverted opal the filling fraction of dielectric is less than 26 volume percents, which favors opening of the complete photonic bandgap, if the refractive index of dielectric exceeds the threshold value of 3.0 [12]. Several examples of Si- [13] and $Sb_2Se_3$-inverted [14] opals with large

[1]This chapter is based on: S. G. Romanov, D. N. Chigrin, V. G. Solovyev, T. Maka, N. Gaponik, A. Eychmuller. A. L. Rogach, C. M. Sotomayor Torres, "Light emission in a directional photonic bandgap," Phys. Stat. Sol. (a) **197** 662–672 (2003); D. N. Chigrin, T. Maka, S. G. Romanov and C. M. Sotomayor Torres, "Angular distribution of emission intensity in inverted opals,' ' manuscript in preparation for *Phys. Rev. E*

enough contrast have been realized for the near-infrared part of the spectrum, but no complete photonic bandgap in the visible have been reported so far. For this reason all reported experiments in the visible were performed with opal photonic crystals of a directional bandgap. The gap, which is, usually, addressed in experiments, is the one due to the Bragg diffraction resonance on a stack of (111) planes of opal. In the case of opals made from dielectric or air spheres, the midgap frequency of the Bragg resonance changes dramatically with the angle of observation due to the lattice symmetry. Correspondingly, one can expect the anisotropy of those emission phenomena, which relate to the Bragg stopband.

In section 7.1, a brief description of experimental results is given. An angular distribution of radiated power of an isotropic point light source is analyzed in section 7.2. The enhancement of photoluminescence in some directions is explained in terms of photon focusing. A comparison of experimental and theoretical results is given in section 7.3. A summary is presented in section 7.4.

## 7.1 Photoluminescence directionality diagrams

The samples under study were inverted opal films of $\sim 1$ cm$^2$ area. The crystals have been formed by infilling the voids of the fcc lattice of the poly-methyl-methacrylate (PMMA) beads with $SnS_2$ and subsequent removal of the PMMA. PMMA spheres were crystallized in the fcc lattice with (111) planes along the substrate plane (Fig. 7.1). The beads diameter of studied samples was $D \approx 300$ nm. Samples were prepared at the University of Mainz (Mainz, Germany), further details are given elsewhere [15].

In the right panel of figure 7.2, the transmission spectrum of the inverted crystal is presented for normal incidence. Transmission spectra were measured under white light illumination from a tungsten lamp. The transmitted light was collected at a solid angle of approximately 2°. The Bragg stopband covers the energy region between $1.96 - 2.30$ eV. The suppression of the transmission is about 20 times near the Bragg stopband center. The Bragg stopband corresponds to the first photonic bandgap of the opaline photonic crystal, which is open in the [111] direction of the fcc lattice. In the left panel of figure 7.2, photonic band structure, calculated using the plane-wave expansion method [16], is presented. The best fit to experimental data has been obtained for the crystal modeled by the fcc lattice of overlapping air spheres with diameter $D = 304$ nm in a dielectric background with a refractive index $n = 2.3$ and a filling fraction of 13%. The refractive index of the bulk $SnS_2$ is $n_b = 3.4$ at the absorption bandedge, so an effective refractive index $n = 2.3$ means that the inverted opaline photonic crystal is porous and $SnS_2$ occupies only a part of the avaliable free volume in the PMMA template [15]. A calculated Bragg stopband spans the frequencies

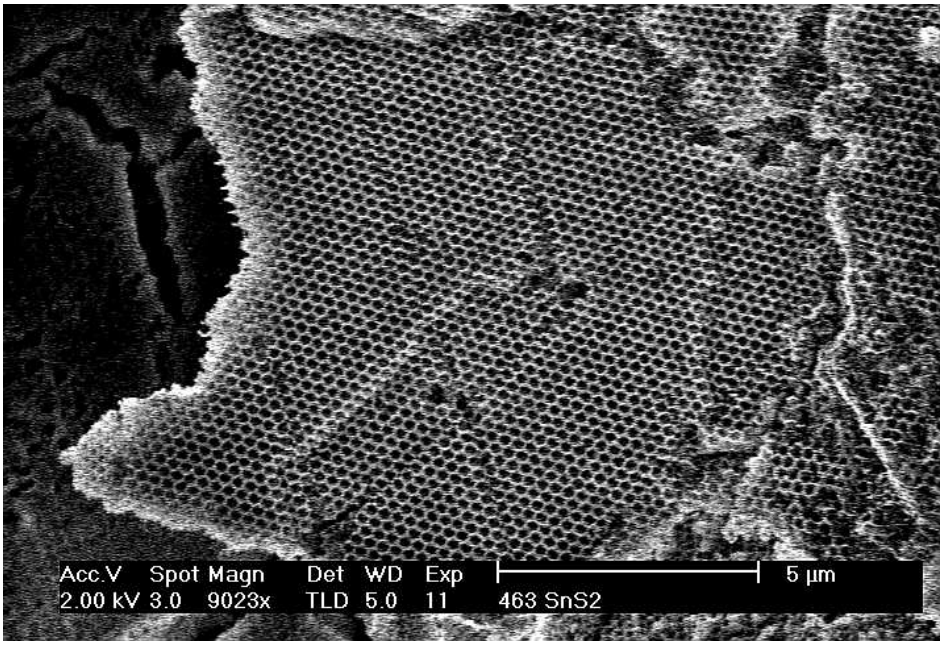


Figure 7.1: Scanning electron microscopy image of the inverted opal film. One can see a hexagonal lattice, which corresponds to the (111) plane of the fcc lattice. (Courtesy of Dr. S. G. Romanov, University of Wuppertal.)

from 0.670 to 0.775 ($2\pi c/a$), here $a = \sqrt{2}D$ is the lattice constant, showing a good agreement with experimental data. The gap width to midgap frequency ratio $\Delta\omega/\omega$ is about 14.5%.

The midgap frequency of the Bragg stopband changes dramatically with the angle of observation due to the lattice symmetry (Fig. 7.2-left). It is instructive to describe the spatial anisotropy of electromagnetic wave propagation in opals using the concept of the Bragg cone, which is defined as the angular interval covered by the Bragg stopband at a given frequency or the corresponding interval of wave vectors in the **k**-space. If the aperture of the collecting optics is less than the angular width of the Bragg cone, then there will be no ballistic eigenmodes of allowed bands, which propagate linearly along the photonic bandgap direction. The Bragg cone changes its width with frequency, which allows comparison of the spontaneous emission inside and outside the bandgap at the same frequency by changing the observation direction.

The study of emission from opals require integrating them with light sources. One can use laser dyes [17, 18], rare-earth ions [19] or semiconductor nanocrystals [17, 20] for this purpose. In the experiments discussed here [11], the dye perylene was chosen as a light source. Perylene dye molecules were placed inside the inverted crystal penetrating the porous carcass by immersing it in a 2.5 g/l perylene in chloroform solution and subsequent drying [18]. The emission band of a perylene dye overlaps with the Bragg stopband of the samples studied. Dye molecules have been homogeneously distributed

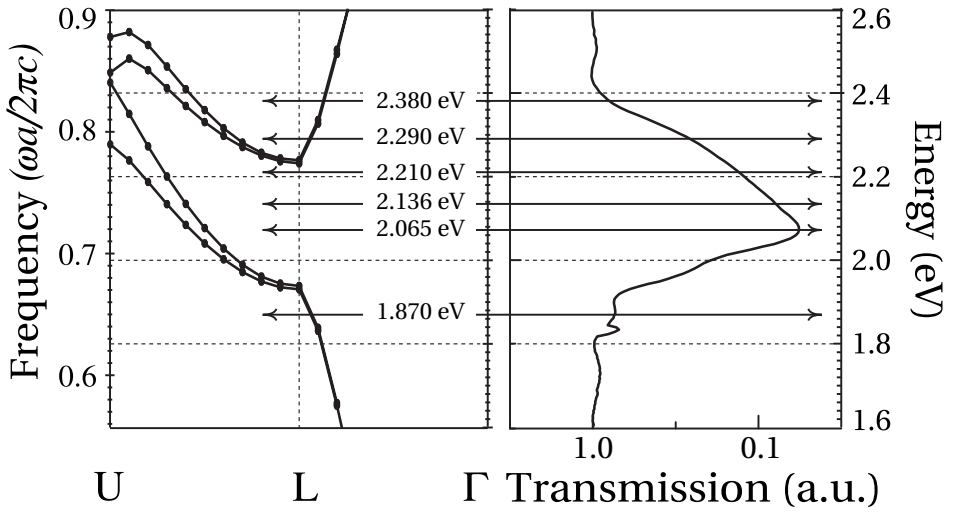


Figure 7.2: Photonic band structure (left) and normalized transmission spectrum (right) of $SnS_2$ inverted opaline photonic crystal recorded at normal incidence. Arrows mark energies at which angle resolved PL spectra have been obtained. The frequency is normalized to $\Omega = \omega a/2\pi c$. $c$ is the speed of light in vacuum.

over the internal surface of air spheres. The photoluminescence was excited by the 351 nm line of an $Ar^+$-laser operating in continuous-wave (CW) mode and collected within a 5° fraction of the solid angle from the sample face opposite to that exposed the laser beam.

In figure 7.3, the angle resolved PL intensity (directionality diagrams) measured far from the sample are shown (solid line with filled dots). To obtain the directionality diagrams the PL intensity at a given frequency was measured as a function of the angle, $\theta$, by rotating the sample. Given the [111] growth direction of the opal lattice with respect to the substrate, the angle $\theta$ is a measure of the detection angle with respect to the normal to (111) planes. In order to take into account the intensity increase due to the longer optical path of the laser beam in the film, the resulting diagrams were multiplied by $\cos\theta$.

The evolution of experimental directionality diagrams can be described as follows (Fig. 7.3). At frequencies below the Bragg stopband it acquires a bell-like shape, which is slightly narrower than the directionality pattern of the Lambert law [21] shown by the red line. When the sample frequency enters the Bragg stopband range from its low-energy side, the directionality pattern shows two lobes centered approximately at $\theta = \pm 20°$ with respect to the [111] axis. A further increasement in frequency results, firstly, in the increase of the lobe angular separation and, secondly, in the development of a third lobe corresponding to [111] direction. The central lobe grows steadily with increasing frequency, whereas the magnitude of side lobes, which are set at approximately $\theta = \pm 40°$ after the emergence of the central lobe, gradually decreases.

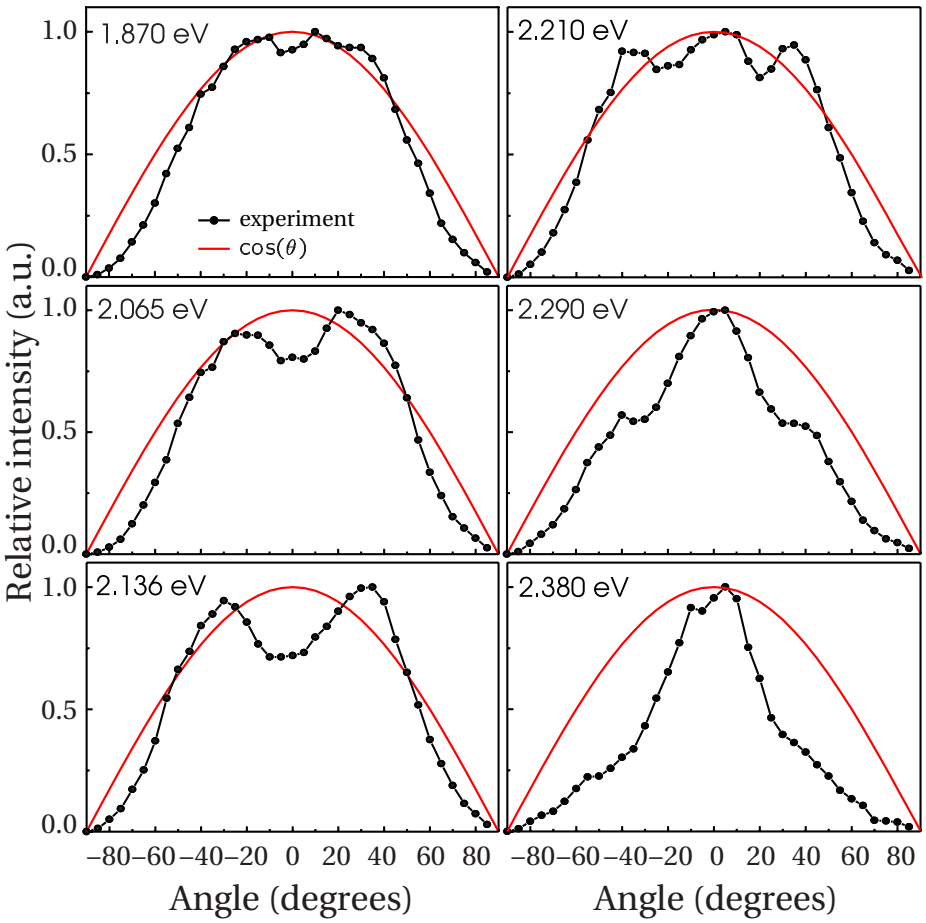


Figure 7.3: Angle resolved PL intensity of the perylene dye-loaded inverted opaline photonic crystal (solid line with dots). The Lambert law (red line) is shown for comparison. The detection angle $\theta = 0°$ corresponds to the [111] direction of the fcc lattice. The energies are those of Fig. 7.2. (Courtesy of Dr. S. G. Romanov, University of Wuppertal.)

At frequencies above that of the upper frequency edge of the Bragg stopband along the [111] direction the directionality diagram acquires a shape elongated towards the central lobe with the small side lobes.

At frequencies within the Bragg stopband, the angle resolved PL intensity shows a common behavior. When compared with emission intensity in free space (red line in Fig. 7.3), the PL intensity of the dye in the inverted opal is suppressed near the [111] direction and it is enhanced at some angle with respect to the [111] direction of the fcc lattice (Fig. 7.3). If an effective channel of non-radiative recombination exists in the system, the PL intensity is directly proportional to the spontaneous emission rate [22]. Thus, for the emission of dye in an opal, one can claim a suppression and an enhancement of spontaneous emission rate with respect to free space in some spatial directions for the frequencies within the Bragg stopband.

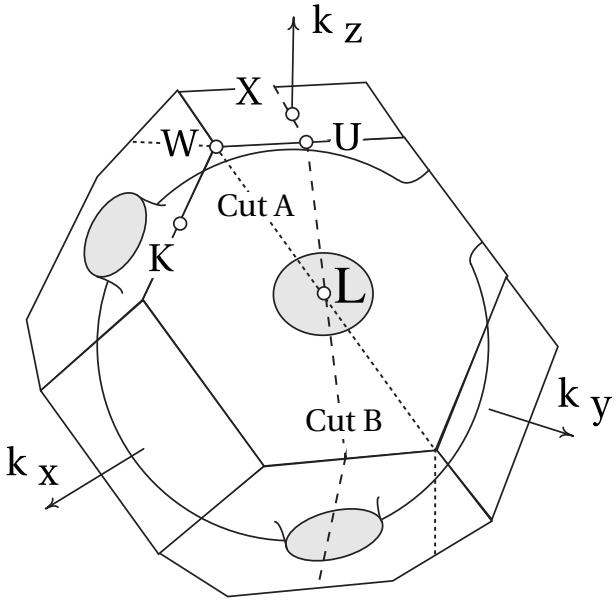


Figure 7.4: The first Brillouin zone and a schematic view of the iso-frequency surface corresponding to the first photonic band of an inverted opal photonic crystal for a frequency inside the Bragg stopband. The iso-frequency surface of the second band has a similar topology and is not shown for clarity.

## 7.2 Angular distribution of radiated power

In the angle resolved measurements, the PL intensity in the given observation direction is averaged only over a small solid angle near this direction. At the same time, dipole moments of dye molecules are randomly distributed in space, so the emission intensity should be averaged over the dipole moment orientation. As it was shown in chapter 5, in this situation the radiated power per solid angle in coordinate space is given by relation (5.28), which reads as

$$\left(\frac{dP}{d\Omega}\right)_i \sim \sum_n \sum_\nu |\mathbf{V}^\nu_{n\mathbf{k}}|^{-1} \, |K^\nu_{n\mathbf{k}}|^{-1}$$

where $\mathbf{V}^\nu_{n\mathbf{k}}$ is the group velocity and $K^\nu_{n\mathbf{k}}$ is Gaussian curvature of iso-frequency surface. Summation over $\nu$ is over all Bloch eigenwaves having their group velocity vectors pointing in the observation direction, while summation over $n$ is over all photonic bands.

A schematic view of the iso-frequency surface of an inverted opaline photonic crystal is presented in figure 7.4 for a frequency inside the Bragg stopband. The iso-frequency surface of inverted opaline photonic crystal deviates from a sphere mainly near the [111] directions. Here the Bragg stopband is open and the iso-frequency surface is strongly distorted, forming a neck. Such a surface consists of alternating regions with nega-

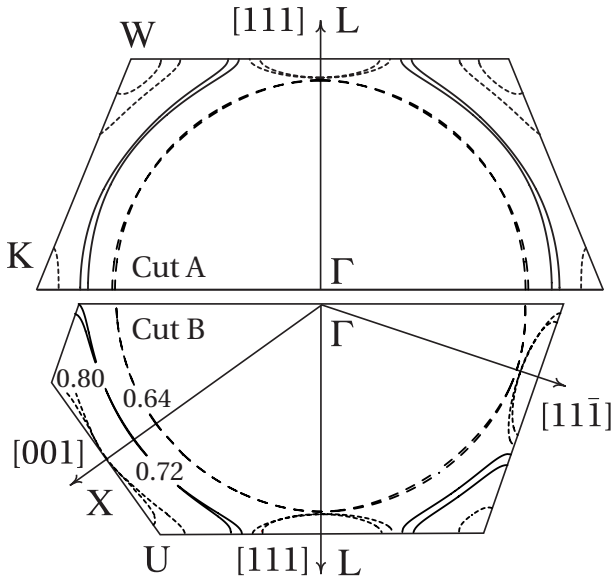


Figure 7.5: Iso-frequency contours for the frequencies below (dashed), inside (solid) and above (dotted) the Bragg stopband, where the normalized frequencies, $\Omega$, are 0.64, 0.72 and 0.80. Iso-frequency contours are shown for two cuts of the first Brillouin zone of the fcc lattice, cut A (top) and cut B (bottom) as depicted in Fig. 7.4.

tive and positive Gaussian curvature separated by the parabolic lines with vanishing curvature.

In figure 7.5, iso-frequency contours are presented for three different frequencies: below ($\Omega = 0.64$), inside ($\Omega = 0.72$) and above ($\Omega = 0.80$) the Bragg stopband (Fig. 7.2). The iso-frequency contours are plotted for two cuts of the Brillouin zone containing [111] direction. They cut the Brillouin zone through the symmetry points K, W, L and $\Gamma$ (cut A) and through the points X, U, L and $\Gamma$ (cut B). Cuts are depicted in figure 7.4 by dotted and dashed lines, respectively. The cut A displays a mirror symmetry about [111] axis, while the cut B does not. In what follows, an angular distribution of the radiative power will be presented only for the symmetric cut A. It is assumed here, that the macroscopic measurements of the PL intensity average away the difference among Brillouin zone cuts, leading to the angular intensity distribution possessing mirror symmetry about the [111] direction.

As the frequency stays below the stopband, an iso-frequency contour is closed and almost circular (Fig. 7.5). The Gaussian curvature does not vanish for any wave vector. This results in a small anisotropy in the energy flux inside the crystal. A wave contour, corresponding to the normalized frequency $\Omega = 0.64$, is presented in the figure 7.6 (a) for the first photonic band of the opaline photonic crystal. The wave contour is a single valued function of the observation direction [Fig. 7.6 (a)]. In figure 7.7 (a), an angular distribution of the radiated power for the normalized frequency $\Omega = 0.64$ is

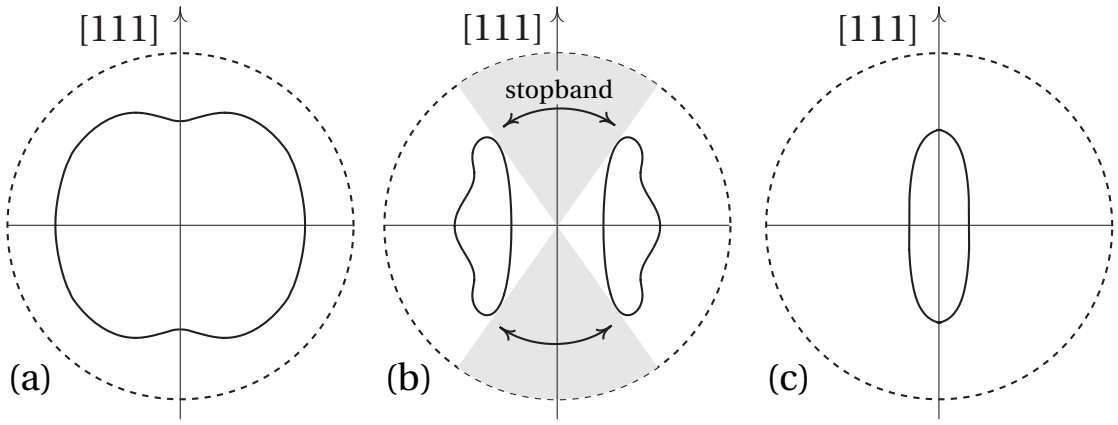


Figure 7.6: Wave contours corresponding to normalized frequencies $\Omega = 0.64$ (a), $\Omega = 0.72$ (b) and $\Omega = 0.80$ (c). Only the wave contours corresponding to the first and third bands are shown in the diagrams (a-b) and (c), respectively. The light grey region in (b) is a stopband. The group velocity is given in units of the speed of light in vacuum. The dashed circle is a wave contour in vacuum.

presented. It shows small amount of anisotropy and reasonably resembles the Lambert law (dashed line). To calculate the radiated power (5.28), one should sum over all photonic bands, which are avaliable at the given frequency. It is assumed here, that the probability of the emission coupling with a given band is equal for all bands.

With increasing the frequency up to the stopband, the topology of an iso-frequency contour changes abruptly. The stopband developed in the [111] direction and the iso-frequency contour becomes open (Fig. 7.5). These topology changes result in a complex contour with alternating regions of different Gaussian curvature. The vanishing curvature results in the folds of the wave contour. The wave contour corresponded to the iso-frequency $\Omega = 0.72$ is presented in the figure 7.6 (b) for the first photonic band of the opaline photonic crystal. The folds in the wave contours yield that two Bloch eigenwaves are traveling in any observation direction outside the stopband. Contributions from both eigenwaves should be taken into account, when the total radiated power is calculated. In figure 7.7 (b), an angular distribution of the radiative power corresponding to the normalized frequency $\Omega = 0.72$ is presented. The energy flux is strongly anisotropic for this frequency, showing zero intensity in the direction of the stopband, and infinite intensity in the direction of the folds of the wave contours (at approximately $\theta = \pm 40^\circ$ with respect to the [111] direction).

When the frequency crosses the upper boundary of the Bragg stopband, the third and fourth photonic bands develop and the stopband closes near the [111] directions. An angular distribution of the radiative power corresponding to the normalized frequency $\Omega = 0.80$ is presented in the figure 7.7 (c). It shows an infinite intensity at approximately $\theta = \pm 40^\circ$ and a Gaussian-like lobe centered at [111] direction. An in-

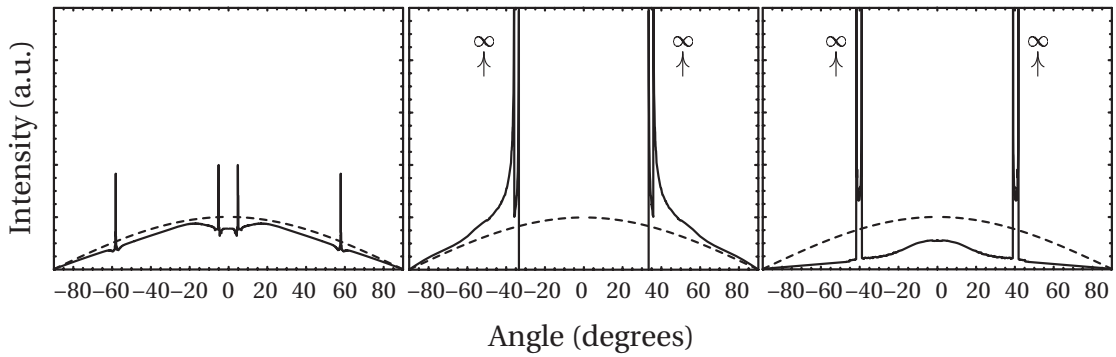


Figure 7.7: Angular distribution of the radiated power for normalized frequencies $\Omega = 0.64$ (a), $\Omega = 0.72$ (b) and $\Omega = 0.80$ (c) calculated with Eq. (5.28). The radiated power in free space (Lambert law) is shown for comparison (dashed line).

finite intensity corresponds to the points of vanishing Gaussian curvature of the first and second photonic bands, while the central lobe is associated with the third and fourth bands. In figure 7.6 (c), a wave contour of the third band corresponding to the normalized frequency $\Omega = 0.80$ is depicted. It is single valued function elongated along [111] direction, which leads to the preferable energy flux in that direction.

## 7.3 Comparison of experimental and theoretical results

To compare experimental results with the theoretical model, the radiated power (5.28) was calculated with a 5° angular step and was integrated within a 5° aperture around the observation direction. The resulting normalized angular distribution of radiated power is presented in figure 7.8 by blue lines with dots. Experimental PL intensity is depicted by black line with dots. The Lambert law (red line) is shown for comparison. A reasonable agreement between experimental and theoretical results is obtained for all frequencies studied. The main difference between theory and experiment appeases within the stopband region. In contrast with a complete suppression of the radiated power predicted by theory for an infinite photonic crystal, the experimentally obtained PL intensity displays only 40-50% decrease of the emission intensity.

For a crystal with a finite thickness, one can estimate the emission suppression by comparing the sample thickness with the Bragg attenuation length. The Bragg attenuation length can be deduced from $\Delta\omega/\omega_0 = 2d/\pi L_B$ and gives the length over which the emission intensity drops by a factor $1/e$ due to Bragg reflection. Here $d$ is the (111) inter-plane distance and $\Delta\omega/\omega_0$ is the full width at the half maximum of the Bragg minimum in the transmission spectrum. For the sample studied here (Fig. 7.2),

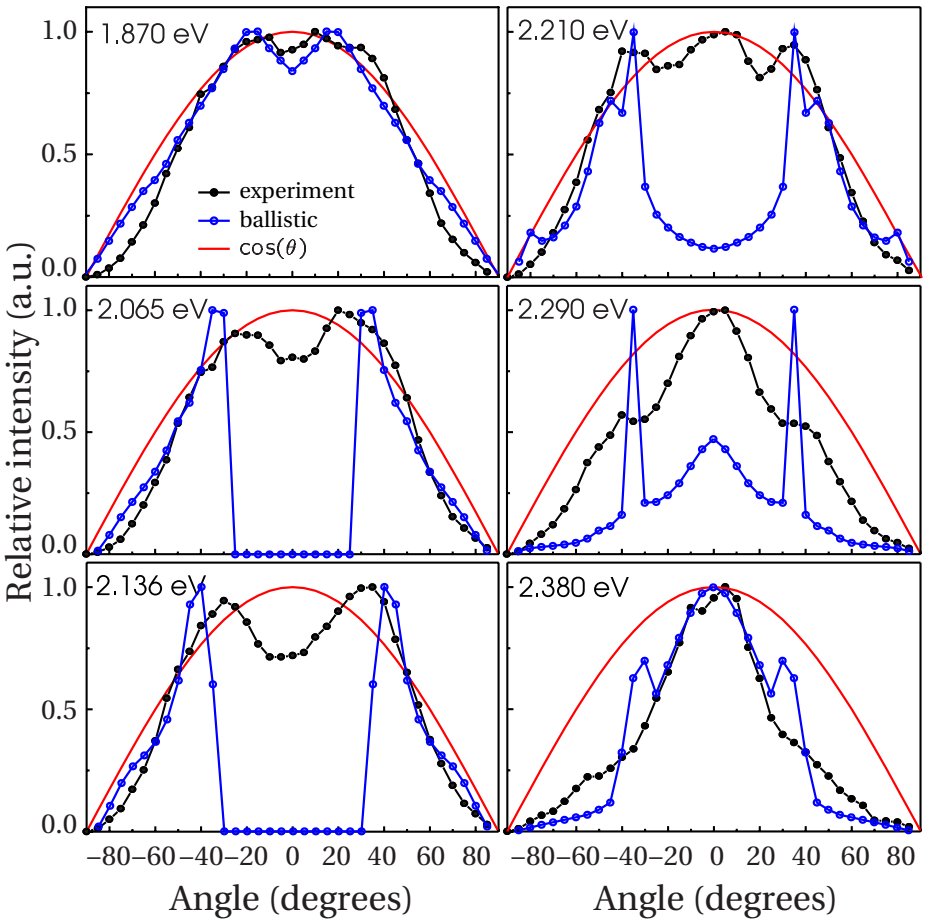


Figure 7.8: Experimental (black lines with dots) and theoretical (blue lines with dots) angular distribution of the emission intensity of dye-loaded inverted opaline photonic crystal. Lambert law (red line) is shown for comparison.

the Bragg attenuation length is 1 $\mu$m. Then, for a sample of 20 $\mu$m thickness, a 99.99% drop of the emission intensity is expected for a light source at the Bragg resonance frequency, $\omega_0$, if it is located 10 $\mu$m away from the sample surface. This conclusion is only valid, if the crystal lattice is perfect.

Due to a self-assembly nature of opals formation, a typical research-grade opal intrinsically has a finite density of structural defects. Then, the emission from an opal with embedded light sources is made up of two components: the ballistic component, made out of photons which reach the detector without scattering, and the scattered component composed of photons, which experience scattering on defects before being detected. The scattered component becomes essential, if the optical path of the light within the photonic crystal exceeds the mean free path (MFP). The MFP in the opal decreases from infinity in the perfect lattice to $l = 7 - 15\,\mu$m in the current research quality opals [23].

The necessary condition to observe an influence of photonic crystal on the emission

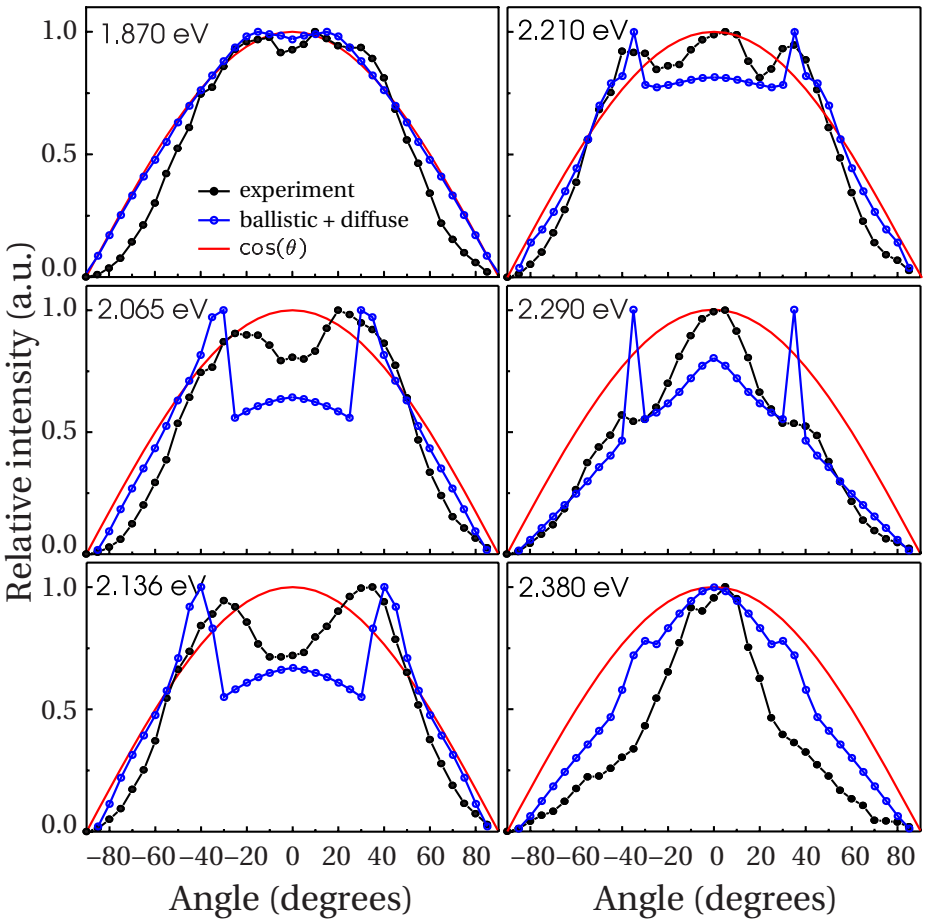


Figure 7.9: Experimental (black lines with dots) and theoretical (blue lines with dots) angule resolved PL intensity of dye-loaded inverted opaline photonic crystal. The theoretical results were obtained by adding $4\cos\theta$ to the ballistic results presented in figure 7.8. Lambert law (red) is shown for comparison.

spectrum is $L_B < l$. It means that in the crystal between successive scattering events light propagates in the form of the Bloch eigenwave. If the sample thickness is much larger than the MFP, the emission coming from the rear part of the sample is diffusively scattered before reaching the detector, i.e., it acquires an isotropic directionality diagram. The emission from the upper near-surface part of the sample, i.e., from the layer with the thickness smaller than the Bragg attenuation length, is not strongly affected by the photonic crystal and is therefore charectarized by an isotropic directionality diagram. The contribution to the detected signal coming from the interior of the opal film consists of multiple scattered photons, which have experienced one or more successive scattering event at lattice defects. Consequently, the observed weak decrease of the PL intensity in the stopband region is an indication of a strong contribution of diffusively scattered light and the near-surface emission to the total detected luminescence.

The isotropic component of the emission provides the background, the intensity

of which varies as cosine of the detection angle (Lambert law). To compare ballistic model (5.28) with experiment, it is assumed that the detected luminescence consists of isotropic and ballistic components only. Within this approximation the contribution from multiply scattered photons is neglected. In figure 7.9, the sum of the ballistic radiated power (5.28) with the isotropic background in the form $4\cos\theta$ is presented. An overall improvement of the correspondence between theory and experiment is obtained as compared with figure 7.8. If additionally one takes into account the multiple scattered component of the luminescence, the broadening of the photon focusing side lobes together with overall smoothening of the radiated power directionality diagrams would be obtained.

The slight disagreement in the angular position of the photon focusing direction predicted by the model as compared with the experiment (Figs. 7.8-7.9) is due to the refraction of the emitted light at the boundary of the sample, which is not taken into account in the presented model. Due to the strongly inhomogeneous nature of the Bloch eigenwaves, their refraction at the photonic crystal–air interface cannot be simply analyzed by the Snell law. An analysis of the inhomogeneous Bloch wave refraction at the photonic crystal–air interface should include all spatial harmonics constituting the eigenwave and it is beyond the scope of this chapter.

## 7.4 Summary

In this chapter, the method developed in chapter 5 was applied to analyze experimental results of PL in an inverted opaline photonic crystal. The reported directionality diagrams of the emission of dye molecules embedded in the inverted opaline photonic crystal reveal the suppression of the emission in the direction of the Bragg stopband and the enhancement of the emission intensity in the photon focusing directions. A reasonable agreement between the developed theory and experiment is reported. The possibilities of further theory improvement to take into account a complexity of the research-grade opals were discussed.

# Bibliography


[1] S. Y. Lin and J. G. Fleming, "A three dimensional optical photonic crystal," *J. Lightwave Technol.* **17,** 1944–1947 (1999).

[2] S. Noda, N. Yamamoto, M. Imrada, H. Kabayashi, and M. Okato, "Alignment and stacking of semiconductor photonic bandgaps by wafer-fusion," *J. Lightwave Technol.* **17,** 1948–1955 (1999).

[3] K. Wang, A. Chelnokov, S. Rowson, P. Garoche, and J. M. Lourtioz, "Focused-ion-beam etching in macroporous silicon to realize three-dimensional photonic crystal," *J. Phys. D: Appl. Phys.* **33,** L119–L123 (2000).

[4] T. Sato, K. Miura, N. Ishino, Y. Ohtera, T. Tamamura, and S. Kawakami, "Photonic crystals for the visible range fabricated by autocloning technique and their applications," *Opt. Quantum Electron.* **34,** 63–77 (2002).

[5] M. Campbell, D. N. Sharp, M. T. Harrison, R. G. Denning, and A. J. Turberfield, "Fabrication of photonic crystals for the visible spectrum by holographic lithography," *Nature* **404,** 53–56 (2000).

[6] S. Shoji and S. Kawata, "Photofabrication of three-dimensional photonic crystals by multibeam laser interference into a photopolymerizable resin," *Appl. Phys. Lett.* **76,** 2668–2670 (2000).

[7] Y. V. Miklyaev, D. C. Meisel, A. Blanco, G. von Freymann, K. Busch, W. Koch, C. Enkrich, M. Deubel, and M. Wegener, "Three-dimensional face-centered-cubic photonic crystal templates by laser holography: fabrication, optical characterization, and band-structure calculations," *Appl. Phys. Lett.* **82,** 1284–1286 (2003).

[8] V. G. Balakirev, V. N. Bogomolov, V. V. Zhuravlev, Y. A. Kumzerov, V. P. Petranovskii, S. G. Romanov, and L. A. Samoilovich, "Three-dimensional superlattices in opal matrices," *Crystall. Rep.* **38,** 348–353 (1993).

[9] S. G. Romanov and C. M. Sotomayor Torres, "Three-dimensional lattices of nanostructures: the template approach," in *Handbook of Nanostructured Materials and Technology*, H. S. Nalwa, ed., (Academic Press, San Diego, 2000), pp. 231–323.

[10] T. Maka, D. N. Chigrin, S. G. Romanov, and C. M. Sotomayor Torres, "Three dimensional photonic crystaks in the visible regime," in *Progress In Electromagnetics Research*, A. Priou and T. Itoh, eds., (EMW Publishing, Cambridge, 2003), pp. 307–335.

[11] D. N. Chigrin, T. Maka, S. G. Romanov, and C. M. Sotomayor Torres, "Angular distribution of emission intensity in inverted opals," *in preparation* .

[12] S. John and K. Busch, "Photonic bandgap formation and tunability in certain self-organizing systems," *J. Lightwave Technol.* **17,** 1931–1943 (1999).

[13] E. Palacios-Lidon, A. Blanco, F. Ibisate, M. Meseguer, C. Lopez, and J. Sanchez-Dehesa, "Optical study of the full photonic band gap in silicon inverse opals," *Appl. Phys. Lett.* **81,** 4925–4927 (2002).

[14] B. H. Juarez, S. Rubio, J. Sanchez-Dehesa, and C. Lopez, "Antimony trisulfide inverted opals: Growth, characterization, and photonic properties," *Adv. Mater.* **14,** 1486–1490 (2002).

[15] M. Muller, R. Zentel, T. Maka, S. G. Romanov, and C. M. Sotomayor Torres, "Photonic crystal films with high refractive index contrast," *Adv. Mater.* **12,** 1499–1503 (2000).

[16] S. G. Johnson and J. D. Joannopoulos, "Block-iterative frequency-domain methods for Maxwell's equations in a planewave basis," *Optics Express* **8,** 173–190 (2001).

[17] S. V. Gaponenko, V. N. Bogomolov, E. P. Petrov, A. M. Kapitonov, A. A. Eychmueller, A. L. Rogach, I. I. Kalosha, F. Gindele, and U. Woggon, "Spontaneous emission of organic molecules and semiconductor nanocrystals in a photonic crystal," *J. Lightwave Technol.* **17,** 2128–2137 (1999).

[18] S. G. Romanov, T. Maka, C. M. Sotomayor Torres, M. Muller, and R. Zentel, "Emission in a $SnS_2$ inverted opaline photonic crystal," *Appl. Phys. Lett.* **79,** 731–733 (2001).

[19] S. G. Romanov, A. V. Fokin, and R. M. De La Rue, "$Eu_3$+ emission in an anisotropic photonic band gap environment," *Appl. Phys. Lett.* **76,** 1656–1658 (2000).

[20] S. G. Romanov, D. N. Chigrin, V. G. Solovyev, T. Maka, N. Gaponik, A. Eychmuller, A. L. Rogach, and C. M. Sotomayor Torres, "Light emission in a directional photonic bandgap," *Phys. Stat. Sol. (a)* **197,** 662–672 (2003).

[21] M. Born and E. Wolf, *Principles of Optics* (Pergamon, New York, 1980).

[22] A. F. Koenderink, L. Bechger, A. Lagendijk, and W. L. Vos, "An experimental study of strongly modified emission in inverse opal photonic crystals," *Phys. Stat. Sol. (a)* **197,** 648–661 (2003).

[23] J. Huang, N. Eradat, M. E. Raikh, Z. V. Vardeny, A. A. Zakhidov, and R. H. Baughman, "Anomalous coherent backscattering of light from opal photonic crystals," *Phys. Rev. Lett.* **86,** 4815–4818 (2001).

# Part IV

# Refraction

# Chapter 8

# Self-guiding in two-dimensional photonic crystals[1]

As it was shown in chapter 3, anomalous refraction is a consequence of a strong photonic crystal anisotropy. Among other manifestations of photonic crystal anisotropy is *self-collimation* [1] phenomenon. A self-collimated beam of light does not spread when it propagates in a photonic crystal. In contrast to spatial solitons, where the nonlinearity of the homogeneous medium counteracts the natural spreading of the beam due to diffraction, the formation of *self-collimated*, or *self-guided*, beams in a photonic crystal is a purely linear phenomenon. The spreading of the beam is counteracted by the crystal anisotropy, such that all wave vectors building the beam lead to the power flux in the same direction. This can be realized for the wave vectors ending at the flat regions on an iso-frequency surface of a photonic crystal. The self-collimation regime reported by Kosaka et at. [1] relies on the inflection points of an iso-frequency surface, where the Gaussian curvature of the surface tends to zero. Typically, a flat region spreads over very limited wave vector directions centered at the wave vector ending at the inflection point. As a consequence, self-collimation can occur only for very limited orientations of the beam with respect to the crystal lattice and for limited beam widths.

In this chapter, it is shown that for some frequencies the form of iso-frequency surface mimics the form of the Brillouin zone of the crystal. In figure 8.1, iso-frequency contours for realistic square (left) and triangular (right) lattice photonic crystals are depicted. The anisotropy of a photonic crystal changes dramatically with changing frequency, iso-frequency contours evolve from convex (red contours in Fig. 8.1) to

[1]This chapter is based on: D. N. Chigrin, S. Enoch, C. M. Sotomayor Torres, and G. Tayeb, "Self-guiding in two-dimensional photonic crystals," *in Proceedings of SPIE "Photonic bandgap materials and devices"* **4655** 63–72 (2002); D. N. Chigrin, S. Enoch, C. M. Sotomayor Torres, and G. Tayeb, "Self-guiding in two-dimensional photonic crystals," *Opt. Express* **11**, 1203-1211 (2003)

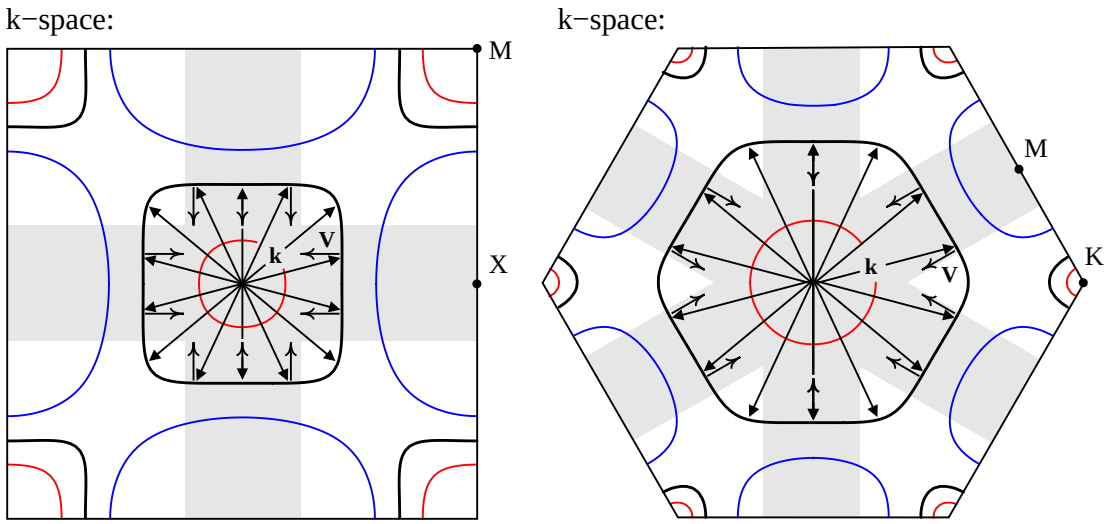


Figure 8.1: Convex (red), concave (blue) and flat (black) iso-frequency contours. Iso-frequency contours on the left (right) panel correspond to the second band of a two-dimensional square (triangular) lattice photonic crystal made of dielectric rods in vacuum. Rods have the refractive index 2.9 and radius $r = 0.15d$, where $d$ is the lattice period. The wave vectors resulting in the Bloch eigenwaves with the group velocity pointing to the direction normal to the Brillouin zone boundary are depicted with arrows.

concave (blue contours in Fig. 8.1). There exists a frequency range where an iso-frequency contour forms an almost perfect square (left) or hexagon (right). Then, a wide angular range of flat dispersion exists canceling out diffraction of a light beam with the corresponding range of wave vectors (Fig. 8.1).

In section 8.1, a physical insight on the the self-guiding phenomenon is given. The radiation pattern of a point source in a photonic crystal is analyzed, taking advantage of an asymptotic analysis developed in chapter 5. The direct numerical simulation of the beam propagation in a finite size photonic crystal is given in section 8.2. The numerical results are obtained using the FDTD method. In section 8.3 the main results of the chapter are summarized.

## 8.1 Fourier space analysis

Without loss of generality, the consideration is restricted to the case of a two-dimension photonic crystal based on a square lattice, which is identical to one investigated in chapter 5. The refractive index of dielectric rods is 2.9 and rods radius is $r = 0.15d$, where $d$ is the period of the lattice. Photonic band structure is shown in figure 8.2 for TM polarization.

The iso-frequency contours of the first two bands of the crystal evolve from convex

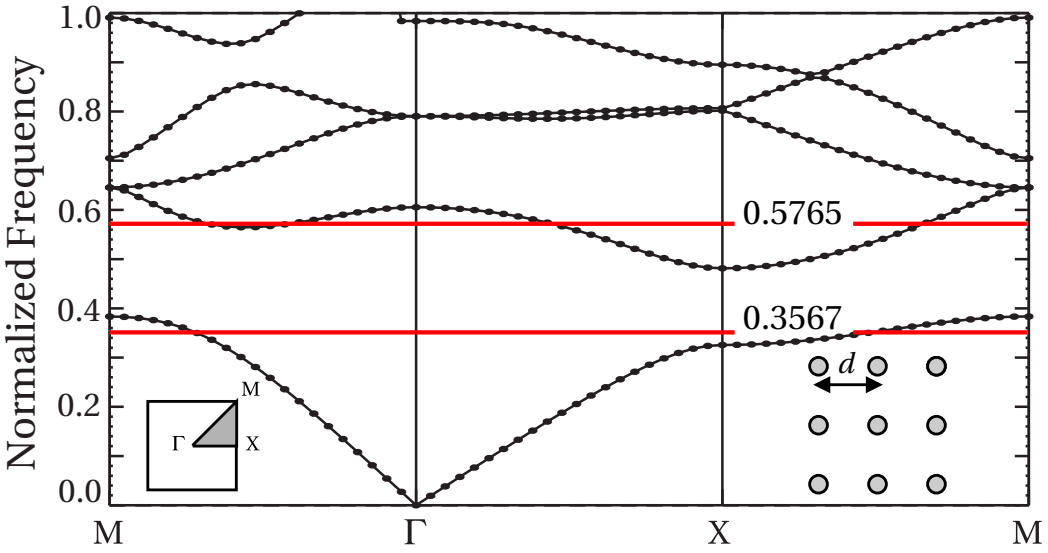


Figure 8.2: Photonic band structure of a square lattice photonic crystal made out of dielectric rods in vacuum. Rods have the refractive index 2.9 and radius $r = 0.15d$, where $d$ is the lattice period. The band structure is given for the TM polarization. The frequency is normalized to $\Omega = \omega d/2\pi c = d/\lambda$. $c$ is the speed of light in the vacuum. Insets show the first Brillouin zone (left) and a part of the lattice (right).

to concave topology. In figure 8.3 transition iso-frequency contours corresponding to the normalized frequencies $\Omega = 0.3567$ (the first band) and $\Omega = 0.5765$ (the second band) are depicted. The iso-frequency contour for the normalized frequency $\Omega = 0.3567$ forms a square with rounded corners, rotated by 45° with respect to the Brillouin zone and centered at M-point of the first Brillouin zone (Fig. 8.3-left). The iso-frequency contour for the normalized frequency $\Omega = 0.5765$ consists of two branches, which are plotted in red and blue in figure 8.3-right. Both branches mimic the form of the first Brillouin zone of the crystal being squares with rounded corners. The "red" branch is centered at the Γ-point and the "blue" branch is centered at the M-point of the Brillouin zone (Fig. 8.3-right).

To analyze how this special kind of anisotropy affects the propagation of light in a photonic crystal, the radiation pattern of a point light source radiating into the crystal is further investigated using the method developed in chapter 5.

In figure 8.4, the angular distribution of the radiated power is presented for the normalized frequencies $\Omega = 0.3567$ (left) and $\Omega = 0.5765$ (right) for the crystal parameters given in the caption of Fig. 8.2. The important feature of the wave propagation inside a photonic crystal at the normalized frequencies considered is that, even a cylindrical initial wave results in an energy flow strongly focused along some specific directions, while it remains negligible for all other directions. To emphasize this special type of self-collimated electromagnetic wave propagation inside a photonic crystal it is called

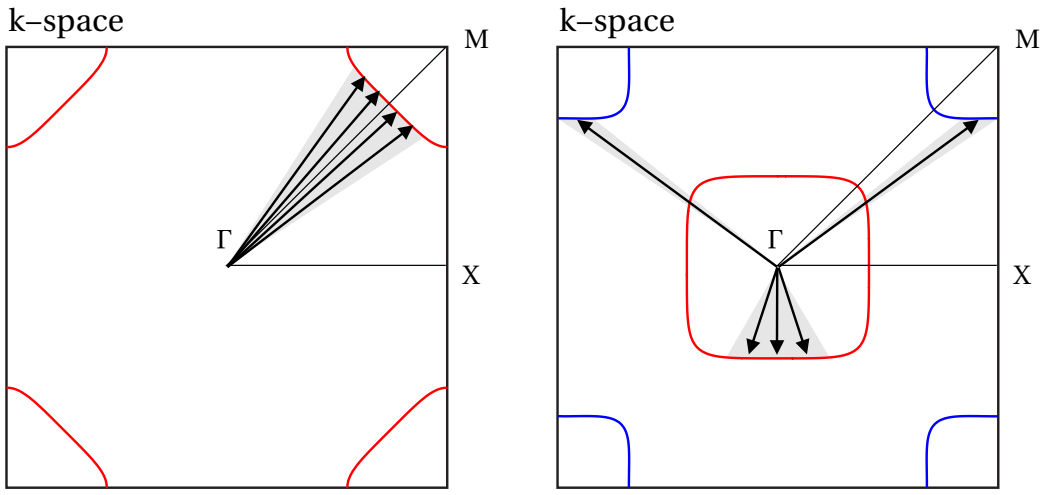


Figure 8.3: Iso-frequency diagram for the normalized frequencies $\Omega = 0.3567$ (left) and $\Omega = 0.5765$ (right). The shaded regions show the wave vectors resulting in the Bloch eigenwaves with the group velocity vectors pointing in the same direction. The crystal parameters are given in the caption of figure 8.2.

here *self-guiding*.

For the first band (Fig. 8.4-left), the radiation pattern is strongly focused along the [11] direction of the lattice. The radiation pattern for the second band (Fig. 8.4-right) is more complex, due to the presence of two branches of the iso-frequencies contour (Fig. 8.3-right). While the "red" branch displays very strong focusing along the [10] direction of the square lattice, the "blue" branch, having some finite curvature, shows a more complex focusing pattern with two rays focused in the directions separated from the [10] direction by approximately 1° (Fig. 8.4-right).

In the *self-guiding* regime the radiation pattern obtained due to a point source suggests that the strongly collimated light propagation is insensitive to the divergence of the initial beam and almost insensitive to the orientations of the beam with respect to the crystal lattice. This property can lead to useful applications of *self-guiding* for waveguide design. A mechanism of spatial light confinement in a self-guiding regime differs significantly, form the wave-guiding mechanisms in both conventional dielectric waveguides [2] and in more recent photonic bandgap waveguides [3]. Strong confinement takes place due to total internal reflection [2] in the former case and due to the complete photonic bandgap [3] in the latter case. Neither a full photonic bandgap nor a physically defined waveguide region are necessary in the case of self-guiding. The spreading of the beam in a photonic crystal is counteracted then by the crystal anisotropy, like in the case of spatial solitons where the nonlinearity of the medium counteracts the natural spreading of the beam due to diffraction.

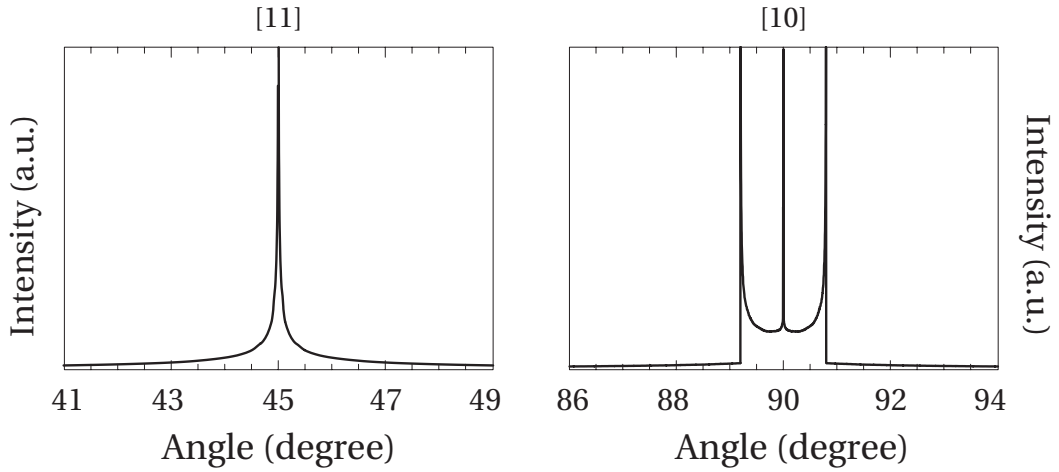


Figure 8.4: Radiation pattern of a point source inside the photonic crystal with the parameters given in the caption of figure 8.2. The normalized frequencies are $\Omega = 0.3567$ (left) and $\Omega = 0.5765$.

## 8.2 Real space analysis

In this section, FDTD method is used to simulate light propagation in a finite two-dimensional photonic crystal in a self-guiding regime. First, the emission of an isotropic point light source inside a two-dimensional photonic crystal is studied. The simulated structure was a $50 \times 50$ lattice of dielectric rods in vacuum. The crystal is surrounded by an extra $5d$ wide layer of a free space. The simulation domain was discretized into squares with a side $\Delta = d/32$. The total simulation region was $1920 \times 1920$ cells plus 8-cell wide perfectly matched layer (PML) [4]. A point isotropic light source was modeled by a soft source [5, 6] with a homogeneous spacial dependence and sinusoidal temporal dependence of the signal.

In figure 8.5 maps of the modulus of the Poynting vector field are shown at the normalized frequencies $\Omega = 0.3567$ (left) and $\Omega = 0.5765$ (right). The point source is placed in the middle of the crystal. A field map is shown for one instant time step. The snap-shots were captured after 10000 time steps, where the time step was $4.38 \times 10^{-17}$ s (0.99 of the Courant value). The structure of the crystal is superimposed on the field map. The highest values of the field are colored red; the lowest are colored blue. From figure 8.5 one can see, that the emitted light is guided in channels in the [11] (left) and [10] (right) directions of the square lattice. This behavior supports the prediction made in the previous section (Fig. 8.4).

To study the beam interaction with a two-dimensional photonic crystal in the self-guiding regime, a $10 \times 20$ rods photonic crystal placed in vacuum was modeled. A simulation domain was $610 \times 640$ cells (Fig. 8.6), with a cell size $\Delta = d/32$. The total simulation domain was surrounded by an 8-cell wide perfectly matched layer (PML)

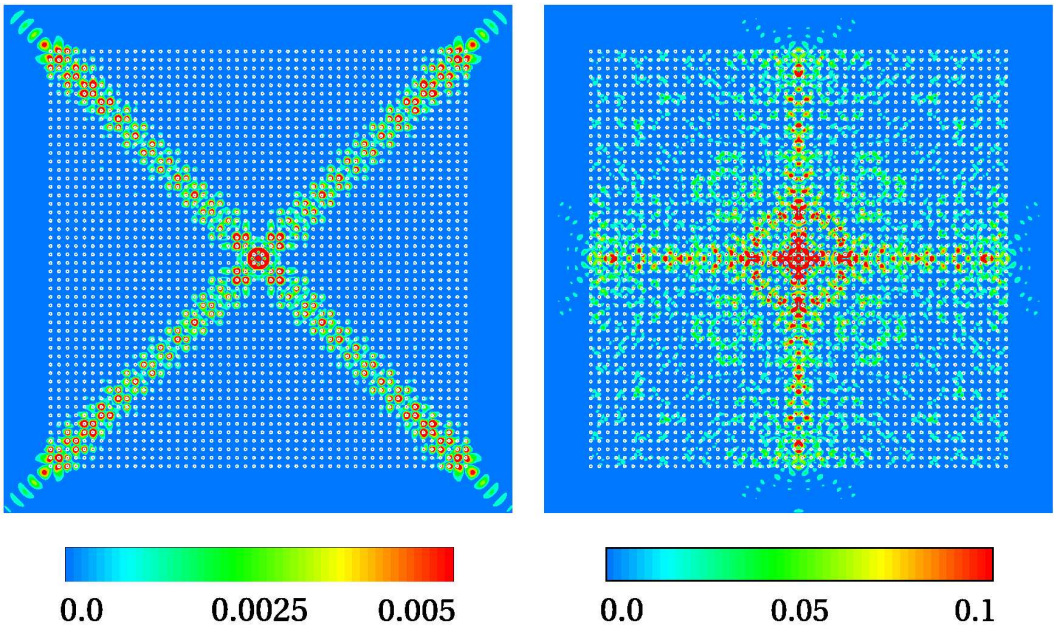


Figure 8.5: Map of the modulus of the Poynting vector field for a $50 \times 50$ rod photonic crystal excited by a point isotropic source. Left: $\Omega = 0.3567$. Right: $\Omega = 0.5765$. The location of the crystal in the simulation is shown.

[4]. To introduce a light beam, a plane wave with a truncated wave front was taken. A temporal dependence of the signal was sinusoidal. A waist of the beam was located at the top of the simulation region, 152 cells apart from the crystal boundary and has a width of 80 cells ($2.5d$). A field generated by a truncated plane wave is equivalent to the field produced by a slit illuminated by a plane wave. For a plane wave incident on a slit from the region $x < 0$, the diffracted wave in the region $x > 0$ arising from a slit can be obtained from Kirchoff integral formulae [7]. A resulting diverging beam generates a wide range of wave vectors.

The beam propagating in free space is shown in figure 8.6-left. A Poynting vector modulus field map is shown for one instant time step after 10000 time steps. In figure 8.6 the structure of the crystal is superimposed on the field map. The highest values of the field are colored red; the lowest are colored blue. The simulation was done for the normalized frequency $\Omega = 0.5765$. The beam is clearly diverging as it propagates in free space (Fig. 8.6-left).

The beam interaction with the photonic crystal at the same normalized frequency is shown in figure 8.6-right. The guiding of the beam is obvious in the crystal, as seeing by comparing the width of the beam at the bottom of the crystal and at the same position in free space (Fig. 8.6-right). In figure 8.7 the beam intensity along the front and back faces of the photonic crystal are given for the same time step as

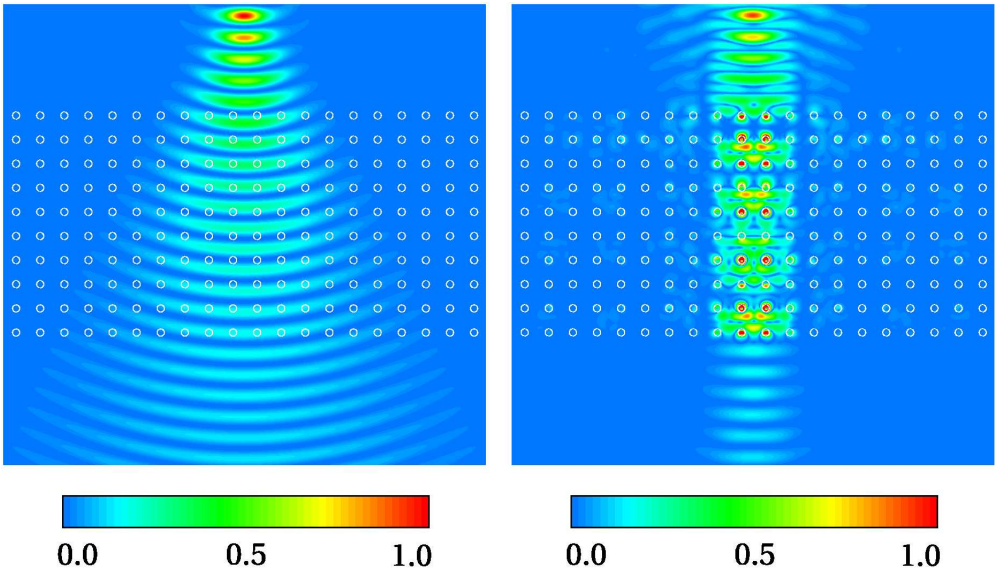


Figure 8.6: Self-guiding in a finite photonic crystal. Left: Map of the modulus of the Poynting vector field of a beam with waist $2.5d$ and the normalized frequency $\Omega = 0.5765$ propagating in free space. Right: Map of the modulus of the Poynting vector field of $10 \times 20$ rod photonic crystal illuminated by the same beam as in the left panel of the figure. The crystal structure is shown in the left panel of the figure to facilitate the comparison.

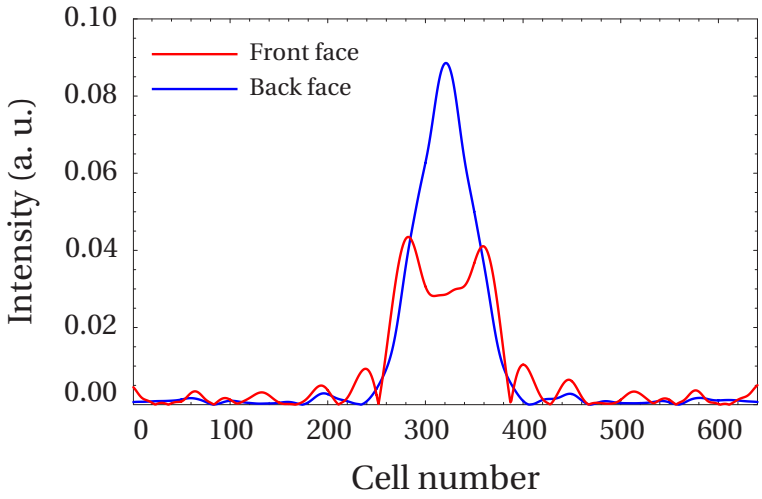


Figure 8.7: Self-guiding in a finite photonic crystal. The modulus of the Poynting vector along the front and back faces of the crystal, orthogonal to the beam axes. There is only a slight difference in the width of the beam before and after propagation through the crystal. The field is given for the instant time step after 10000 simulation steps (Fig. 8.6-right).

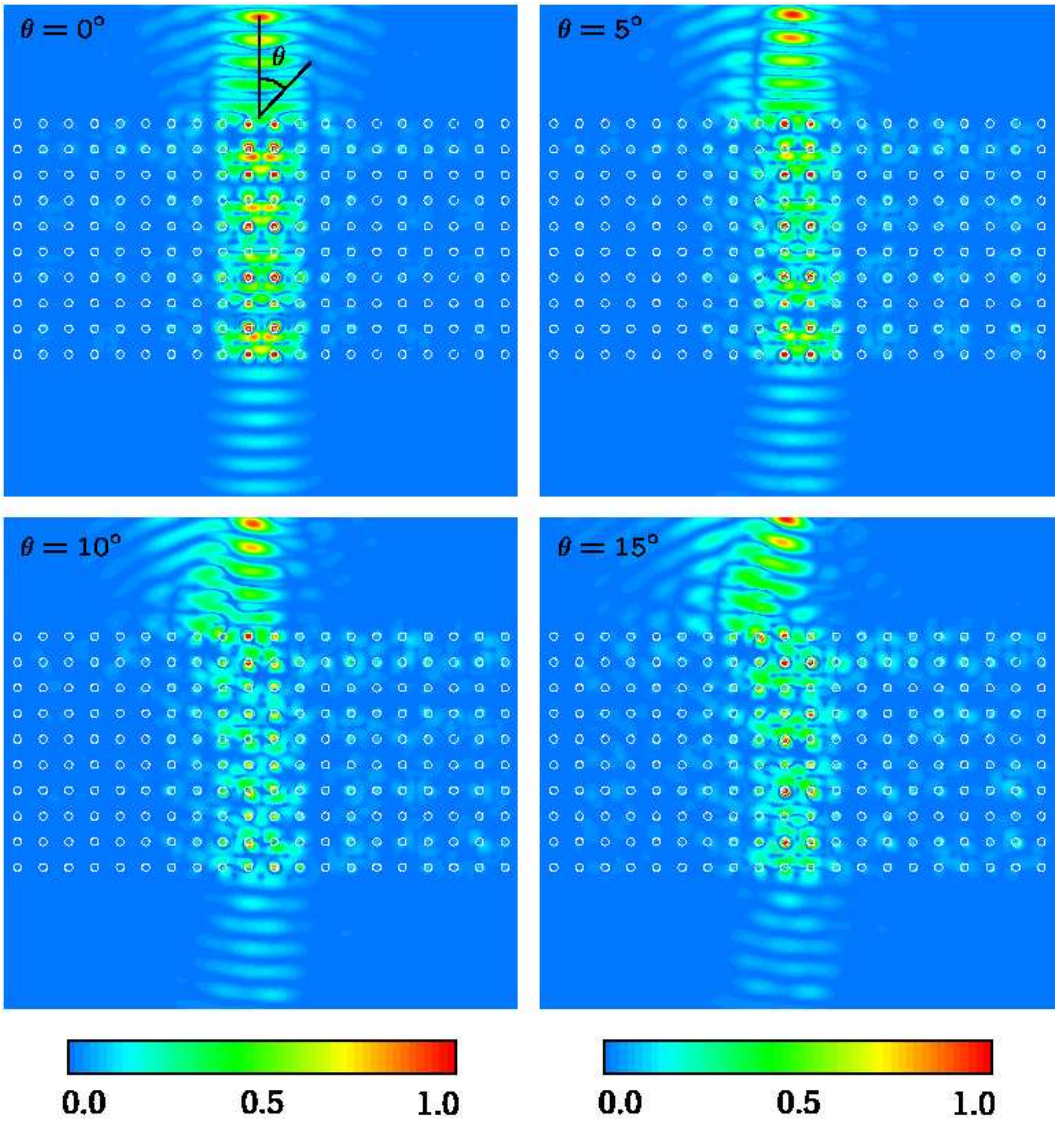


Figure 8.8: Self-guiding in a finite photonic crystal. Map of the modulus of the Poynting vector field of $10 \times 20$ rod photonic crystal illuminated by a beam with waist $2.5d$ and the normalized frequency $\Omega = 0.5765$. The angle of incidence is $0°$ ($5°$) for upper left (right) panel and $10°$ ($15°$) for bottom left (right) panel.

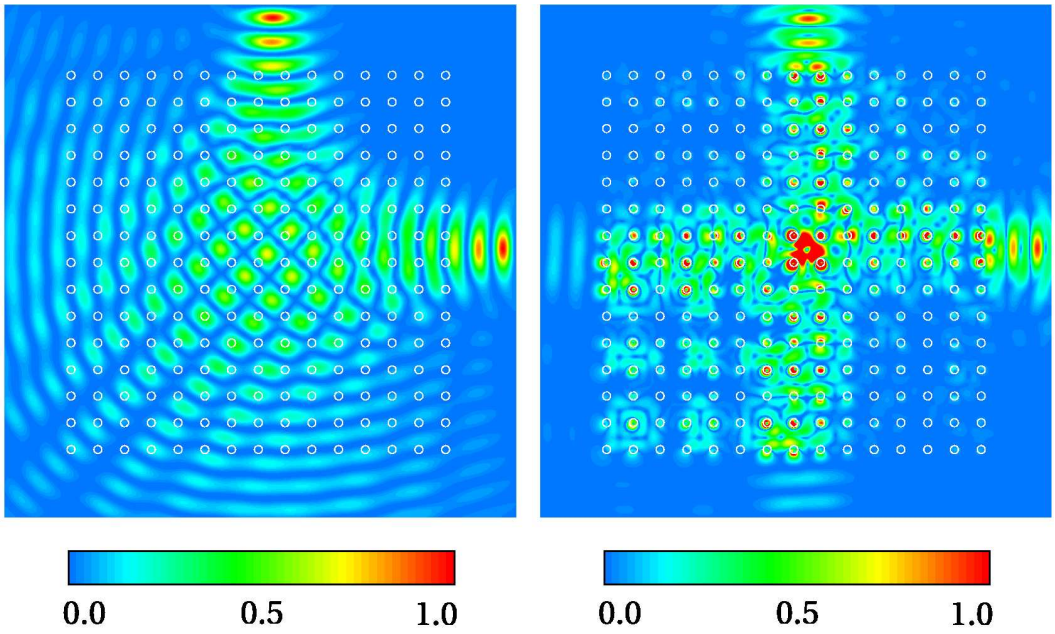


Figure 8.9: Crossing of two self-guided beams. Left: Map of the modulus of the Poynting vector field of two beam with waist $2.5d$ and the normalized frequency $\Omega = 0.5765$ propagating in free space. Right: Map of the modulus of the Poynting vector field of a $15 \times 15$ rod photonic crystal illuminated by the same beams as in the left panel of the figure. The crystal structure is shown in the left panel of the figure to facilitate the comparison.

in figure 8.6-right. There is only a slight difference in the width of the beam above and below the crystal. Here, the front (back) face of the crystal is the first (last) face approached by the incident beam.

Figure 8.8 illustrates the influence of the angle of incidence on the self-guiding propagation of the beam in the photonic crystal. The simulation domain for calculations was the same as in figure 8.6-right. Based on the analysis presented in section 8.1, one can expect, that self-guiding reveals a weak dependence on beam orientation with respect to the crystal lattice. In figure 8.8 the modulus of the Poynting vector for the angle of incidence 0°, 5°, 10° and 15° are shown. The snap-shots were captured after 10000 time steps. One can see, that with increasing angle of incidence the [10] direction of the square lattice remains the preferred direction of propagation and self-guided beam remains strongly focused in this direction.

Figure 8.9 shows a $15 \times 15$ rod photonic crystal illuminated by two beams of the normalized frequency $\Omega = 0.5765$. The first beam impinges from the top of the crystal and the second one impinges from the right. The first beam is identical to the incident beam of the figure 8.6, but its waist is located 88 cells apart from the crystal. The waist of the second beam is located at the very right of the simulation region, 88 cells apart from the crystal boundary. The width of beams is 80 cells ($2.5d$). A simulation domain contained $610 \times 610$ cells (Fig. 8.9), with a cell size $\Delta = d/32$, and was surrounded by 8-cell wide perfectly matched layer (PML) [4]. The Poynting vector modulus field map after 10000 simulation steps is shown in figure 8.9 for two beam propagating in free space (left) and in a photonic crystal (right). The key feature of self-guiding illustrated in this figure is that two beams can cross each other without cross-talk, in a contrast to the case of narrow dielectric waveguides. This effect offers an advantage for applications as it is not trivial to design crossed waveguides with no cross-talk in a comparable size scale.

## 8.3 Summary

In this chapter it was shown, that, by careful engineering of a photonic crystal band structure, one can design an anisotropic crystal which cancel out the natural diffraction of the light beam. A signature of the light beam propagation is such a photonic crystal is a self-guiding of the beam in some specific lattice directions. Unique features of self-guiding are the tolerance to misalignment and no cross-talk between self-guided beams.

# Bibliography


[1] H. Kosaka, T. Kawashima, A. Tomita, M. Notomi, T. Tamamura, T. Sato, and S. Kawakami, "Superprism phenomena in photonic crystals," *Phys. Rev. B* **58,** R10096–R10099 (1998).

[2] A. Yariv and P. Yeh, *Optical Waves in Crystals* (John Wiley and Sons, New York, 1984).

[3] J. D. Joannopoulos, R. D. Meade, and J. N. Winn, *Photonic crystals: molding the flow of light* (Princeton University Press, Princeton NJ, 1995).

[4] J. P. Berenger, "A perfectly matched layer for absorption of electromagnetic waves," *J. Comp. Phys.* **114,** 185–200 (1994).

[5] A. Taflove, *Computational Electrodynamics: The Finite-Difference Time-Domain Method* (Artech House, Norwood, 1995).

[6] D. M. Sullivan, *Electromagnetic Simulation Using the FDTD Method* (IEEE Press, New York, 2002).

[7] M. Born and E. Wolf, *Principles of Optics* (Pergamon, New York, 1980).

# Chapter 9

# Conclusion

Fabrication of a photonic crystal with a complete photonic bandgap in the optical or near infrared spectral range remains a challenging technological problem. This is why, most of the predicted phenomena relying on a complete photonic bandgap still await their experimental demonstration. The study, which results in this thesis, was originally indented (i) to push the limits of photonic crystals with incomplete photonic bandgap to optical applications as well as (ii) to contribute to a solid understanding of light-matter interaction phenomena in photonic crystals with an incomplete photonic bandgap. A contribution to the first more engineering task was achieved by developing ideas of omnidirectional Bragg mirror and photonic crystal-based self-guides. The author hopes that the development of the asymptotic analysis of the classical dipole radiation in a photonic crystal adds to the general understanding of emission processes in periodic medium and contributes to the more fundamental second original task.

A one-dimensional photonic crystal is the simplest example of the medium with an incomplete photonic bandgap. In this thesis, total omnidirectional reflection has been predicted for such a medium. Although detailed criteria of omnidirectional Bragg mirror design are presented in this thesis, further work is necessary to introduce such a mirror in the design of optical devices. This is especially important in the view of successful experimental demonstrations of total omnidirectional reflection from a one-dimensional photonic crystal. Some directions of the future work could include application of omnidirectional mirror to the development of antenna substrates, optical microcavities and fibers.

A two-dimensional photonic crystal is another example of the periodic medium with incomplete photonic bandgap. An exploration of the fact, that a photonic crystal is a strongly anisotropic medium, leads to the idea of self-collimation, in other words, diffractionless laser beam propagation in a photonic crystal. In original proposal of

Kosaka et al. the region of self-collimation behavior was limited to a small sections of the **k**-space.

In this thesis a two-dimensional photonic crystal has been proposed, which cancels out a natural diffraction of the laser beam for a wide range of beam widths and beam orientations with respect to the crystal lattice. The spreading of the beam is counteracted by the crystal anisotropy, as in the case of spatial solitons where the nonlinearity of the medium counteracts the natural spreading of the beam due to diffraction. All calculation of the self-guiding phenomenon presented in this thesis were performed in two-dimensions. In reality a two-dimensional photonic crystal comes as a slab suspended in air or supported by a substrate. An important question still to be answered is to what extend predictions made for two-dimensional system will apply in the three-dimensional case. Questions such as vertical wave confinement, out-of-plane losses, spectral bandwidth, among other are of primarily importance for applications of the self-guiding phenomenon in real optical devices.

The most complex example of a periodic medium with incomplete photonic bandgap is a three-dimensional photonic crystal. Nevertheless, the analysis and modeling of three-dimensional photonic crystals provide maximum flexibility in designing optical devices. For example, in the domain of materials with incomplete photonic bandgap the most promising applications are light sources. Being able to tailor the emission rate within a specific spectral range and simultaneously in specific directions could add a significant flexibility in improving light sources. However, well before designing a light source, a basic physical understanding of emission processes in three-dimensional photonic crystal is essential.

In this thesis, an asymptotic analysis of the classical dipole radiation has been developed. The method introduced gives information on both the far-field radiation pattern and the radiated power modification. If the dipole frequency is within a partial bandgap, the radiated power is suppressed in the direction of a stopband and enhanced in the direction of the group velocity, which is stationary with respect to a small variation of the wave vector. This asymptotic analysis applied to the case of three-dimensional photonic crystal describes reasonably well experimental data on photoluminescence of laser dye molecules embedded in an inverted opaline photonic crystal.

Light emission in a photonic crystal is a very active and controversial research topic. So far there is no clear indications of spontaneous emission rate suppression in a photonic crystal. This is partly because an experiment to observe non-ambiguously spontaneous emission rate modification are still to be performed. In this thesis a small step in the direction of building a consistent explanation of experimental results has been made. For example, it has been shown that far-field radiation pattern of the

classical dipole can be modified due to interference of photonic crystal eigenmodes at the detector plane leading to the added complexity of detected signal.

A classical model of light emission in a photonic crystal corresponds to the quantum mechanical Weisskopf-Wigner approximation, where the problem of the field back-reaction on an emitting dipole is solved assuming that the back-reaction happens infinitely fast. This approximation hides a lot of interesting non-Markovian phenomena, which are worth of a more detailed study. Another common approximation is a perfect periodic lattice of a photonic crystal. Research-grade photonic crystals are not perfect crystalline media, but inhomogeneous media with different sorts of imperfections: dislocation disorder, positioning disorder, etc. While the spectrum of elementary excitations of a perfectly periodic medium is continuous, the spectrum of a random medium is a point spectrum. Imperfect photonic crystal rolls in between of these two classes, leading to a critical spectrum of elementary excitations. Tasks to develop a method to construct spectra of elementary excitations of disordered photonic crystals and to study how criticality of their eigenstates influence the emission of light are both important from a fundamental and a practical point of view.

Photonic crystals remain an active topic of fundamental and applied research and any solved problem contributes to the general understanding of the electromagnetic phenomena in periodic media thereby opening many new exciting question and research problems for future studies.

# Acknowledgments

First of all I would like to thank Prof. Clivia M. Sotomayor Torres for giving me the opportunity to continue my research on photonic crystals in her laboratory at the University of Wuppertal and for being my supervisor over these years. I thank Clivia for her encouragement, help and continuous interest in my work.

I am particular grateful to Prof. Andrei V. Lavrinenko, who introduced me to the exciting world of electromagnetism of complex inhomogeneous media, while I was an undergraduate student at the Belarusian State University. I thank Andrei for being my teacher and friend.

It would be impossible to express my thanks to all those who support and encourage me over these years. I would like to thanks all my colleagues working in the Optical Nanostructures laboratory at the University of Wuppertal for their patience and help. I am particular grateful to Drs. Sergei G. Romanov, Vladimir G. Soloviev, Roman Kian and Patrick Ferrand for many stimulating and encouraging discussions. I am grateful to Torsten Maka for his continuous help. I am grateful to Dmitry A. Yarotsky, Prof. Sergei V. Gaponenko, Torsten Maka and Dr. Sergei G. Romanov for making avaliable for me their experimental results.

And the last not least, this thesis would not be possible without a strong support from my family. I thank my wife Elisabeth and my children Anton, Nikolai and Varvara. Thank you very much for you support and love.

The work presented in this thesis was partially supported by the EU-IST projects PHOBOS IST-1999-19009 and APPTech IST-2000-29321 and German BMBF project PCOC 01 BK 253.